ASSESSMENT OF LOCAL MUSCLE DEFORMATIONS USING MULTI-MODAL IMAGING AND FINITE ELEMENT MODELING

by

Uluç Pamuk

B.Sc. Physics, Boğaziçi University, 2010

Submitted to the Institute of Biomedical Engineering
in partial fulfillment of the requirements
for the degree of
Doctor
of
Philosophy

Boğaziçi University
2019

ASSESSMENT OF LOCAL MUSCLE DEFORMATIONS USING MULTI-MODAL IMAGING AND FINITE ELEMENT MODELING

APPROVED BY:

Prof. Dr. Can A. Yücesoy (Thesis Advisor)	.....
Prof. Dr. Cengizhan Öztürk	.....
Assoc. Prof. Dr. Özgür Kocatürk	.....
Prof. Dr. Çağatay Başdoğan	.....
Prof. Dr. A. Yekta Ülgen	.....

DATE OF APPROVAL: 18 February 2019

ACKNOWLEDGMENTS

Prof. Dr. Can A. Yücesoy for his unending patience, motivation and guidance towards me regarding research, musicianship and life in general,

Prof. Dr. Cengizhan Öztürk Assoc. Prof. Dr. Özgür Kocatürk for their insightful guidance in the progress of the thesis; Prof. Dr. Çağatay Başdoğan Prof. Dr. A. Yekta Ülgen for their participation in the thesis committee and their insightful comments and encouragement;

Assoc. Prof. Dr. Esin Öztürk Işık for her patient and insightful guidance in statistics and Prof. Dr. Burak Acar and VAVlab for their strict guidance in MR–DT data acquisition, registration, tractography and also for allowing use of their tractography software, DTInteract.

Erhan Uyanık and Ömer Seçgin for their patience and guidance in use of heavy machinery during manufacture of experiment hardware; Autodesk Inventor 2012 Student Edition for design of experiment hardware; Slicer3D for segmentation and visualization; GIMP 2.0, Overleaf, Paraview for visualization; Zotero for bibliography;

Acıbadem Kozyatağı and Altunizade Hospitals, and Radiologist Prof. Dr. Alp Dinçer for their support; and technical staff Kaan Mustafa Can, Ömer Arslan, Ertuğrul Gazi Akkuş, Cem Işık, Hacı Osman Yazar, Zafer Yazar, Zafer Dağ and Cihan İpek; and also Onur Özyurt for their help and patience in scheduling and enabling the experiments, and also for their technical expertise;

Agah Karakuzu and Arda Arpak for their collaboration in development of present techniques, and their help during human experiments as well as co-processing of the data;

Physiotherapists Ayça Aklar Çörekçi and Seda Yıldız for applying kinesiological taping and their help in human KT studies;

and all the Volunteers who participated with much patience in the human studies presented in this thesis are gratefully and humbly acknowledged.

This study was supported by The Scientific and Technological Research Council of Turkey (TÜBİTAK) under grants 111E084 (Can A. Yücesoy), 113S293 (Can A. Yücesoy), 118M466 (Can A. Yücesoy).

Agah Karakuzu, Cemre Su Kaya, Ahu Nur Türkoğlu, Filiz Ateş, Arda Arpak, Ayça Aklar Çörekçi, Seda Yıldız, Alican Onur Çankaya, Göktuğ Sanlı and Evrim Yılmaz for being exquisite labmates;

Mustafa Kemal Ruhi, Prof. Yekta Ülgen, Prof. Burak Güçlü, Hakan Solmaz, Didar Talat, Bengü Aktaş, Mustafa Kocatürk for all the jams and gigs with BME (Blues) Bands and especially Prof. Yücesoy for showing me the ways of the blues;

İrem Doğan & Emre Karaoğlan, Gaye Genç & Yunus Emre Kara, Yasemen Birhekimoğlu, Buket Özkaya, Pınar Öz, Berkay Buğdanoğlu and Orhan Kavrakoğlu and for their precious company and discussions regarding higher education;

are gracefully and warmly acknowledged.

Finally, Turgut Pamuk and Mihrinur Evren, my dear parents, and Nihan Nino Koç, my spouse dearest, are whom this thesis is dedicated to, are due for their unwavering support, belief and understanding, which made it all possible.

ACADEMIC ETHICS AND INTEGRITY STATEMENT

I, Uluç Pamuk, hereby certify that I am aware of the Academic Ethics and Integrity Policy issued by the Council of Higher Education (YÖK) and I fully acknowledge all the consequences due to its violation by plagiarism or any other way.

Name :

Signature:

Date:

ABSTRACT

ASSESSMENT OF LOCAL MUSCLE DEFORMATIONS USING MULTI-MODAL IMAGING AND FINITE ELEMENT MODELING

In vivo assessment of muscle deformations, including influence of non-muscular tissues such as NVTs, aponeuroses, fasciæ or overlying skin, is key due to functional relevance of tissue connectivity within limb. In integral framework of anatomy, understanding deformations in muscle and non-muscular connectome, and mechanical interactions therein, is crucial. Muscle deformations caused by external loads, e.g., KT, are conceivable and crucial to quantify when exploring KT's unknown action mechanism. Continuity of muscle fibers and extra-cellular matrix (ECM) is also of relevance. Titin was so far considered as passive spring of sarcomere, a view now changing due to its altered properties in active state. Yet, muscle fiber–ECM interaction can further change titin's influence. This thesis aims to address these by MRI image registration, DTI and FEM. MRI analyses of KT showed principal tissue strains deviated from KT loading direction. By DTI tractography and MRI analyses combined, muscle fiber and shear strains upon passive knee extension were determined. Strains were non-uniform along fascicles, which lengthened (8.7%) and shortened (7.5%), overall. Passive muscle FEM indicated role of NVT connectivity in imposing myofascial loads that cause strain non-uniformities. FEM with active titin showed increased total stress, with little increase from cross-bridges and much from titin. Depending on titin formulation, strain non-uniformities varied, yet persisted. Active force increased or leveled beyond optimum length. Strains were shorter overall: a shorter sarcomere effect. In sum, new non-invasive in vivo DTI and MRI methods are used to assess muscle tissue deformations; FEM allowed proposing new views incorporating epimuscular interactions within limb, with implications for muscle pathophysiology.

Keywords: Diffusion Tensor Imaging (DTI); Magnetic Resonance Imaging (MRI); Myofascial loads; Kinesio Taping (KT); Muscle fiber direction strains; Principal tissue strains; Neuro-vascular Tracts (NVT); Finite Element Modeling (FEM)

ÖZET

LOKAL KAS DEFORMASYONLARININ ÇOKLU MODALİTE GÖRÜNTÜLEME VE SONLU ELEMANLAR MODELLEME İLE DEĞERLENDİRMESİ

Kas deformasyonlarının NVY, aponevroz, fasya veya üzerindeki deri gibi kas dışı dokuların etkisini dahil eden vivo değerlendirmesi, uzuvdaki doku bağlantılılığının işlevsel ilgisi düşünülünce çok önemlidir. Anatominin bütünleşik yapısı dahilinde kas ve kas dışı konektomun deformasyonları; aralarındaki mekanik etkilec simin anlaşılması, kritiktir. KB gibi dış yükler kaynaklı kas deformasyonları böylece kavranabilir ve nicellenmeleri KB'nin bilinmeyen etki mekanizmasını araştırmak için kritiktir. Ekstraselüler matriks (ESM) ile kas fiberlerinin sürerliliği ise ek önem taşır: Şimdiye kadar titin sıkc ca sarkomerin pasif yay elemanı olarak düşünüldü. Bu bakış titinin aktif durumda başkalaşan özellikleri nedeniyle değişmektedir. Ancak kas fiberi–ESM etkileşimi titinin etkisini daha da değiştirebilir. Bu tez MRG ve görüntü çakıştırma; DTG ve traktografi; ve SEM ile bu konuları ele almayı amaçlar. KB'nin MRG analizleri asal doku gerinimlerinin, KB yükleme yönünden saptığını gösterdi. DTG–traktografi ve MRG analizleri ile pasif diz ekstansiyonu sonucu kas fiber ve kayma gerinimleri belirlendi. Toplamda uzayan (%8.7) ve kısalan (%7.5) kesimler içeren fasiküller boyunca gerinimler heterojendi. Pasif kas SEM, gerinim düzensizliklerine neden olan miyobağdokusal yüklerin etkimesinde NVY bağlantılılığının rolünü gösterdi. Titin aktif davranışı dahil SEM, artan kas geriliminde titin katkısı-nın önemini gösterdi. Genelde daha negatif gerinimler, yani daha kısa sarkomer etkisi; optimum boy ötesinde artan veya düzleşen aktif kuvvet görüldü. Sonuçta, kas doku deformasyonlarının değerlendirmesi için yenilikçi, girişimsel olmayan in vivo yöntemler; uzuvdaki epimüsküler etkileşimleri de dikkate alan yeni bakış açılarını kas patofizyolojisine yönelik implikasyonlar ile sunmaya olanak tanıyan hesaplamalı yaklaşımlar kullanıldı.

Anahtar Sözcükler: Difüzyon Tensör Görüntüleme (DTG); Manyetik Rezonans Görüntüleme (MRG); Miyobağdokusal yükler; Kinesiyo Bantlama (KB); Kas fiber gerinimi; Doku asal gerinimi; Nörovasküler Yolak (NVY); Sonlu Elemanlar Modelleme (SEM)

TABLE OF CONTENTS

ACKNOWLEDGMENTS iii
ACADEMIC ETHICS AND INTEGRITY STATEMENT v
ABSTRACT vi
ÖZET viii
LIST OF FIGURES xv
LIST OF TABLES xx
LIST OF SYMBOLS xxi
LIST OF ABBREVIATIONS xxiv
1. OVERVIEW 1
1.1 Anatomy of Muscle and Surrounding Tissue 1
1.2 Imaging Modalities and Advanced Analysis Methodologies for Assessment of Local Deformations in Human Muscle in vivo 4
1.2.1 Ultrasound 4
1.2.2 Magnetic Resonance Imaging 5
1.2.2.1 Calculation of local tissue strains in dynamic conditions 5
1.2.2.2 Calculation of local tissue strains in static conditions . 6
1.2.2.3 Determination of muscle fiber direction 7
1.2.2.4 MRI–DTI to determine local length changes along muscle fibers 8
1.3 Finite element method as a tool for calculation of muscle deformations 8
1.4 Aims of the Thesis 9
1.5 Thesis Overview 10
1.5.1 MRI registration applied to human muscles in vivo and subsequent analyses for assessment of KT effects in terms of principal strains developing in the tissues of the lower leg 10
1.5.2 MRI techniques combined with DTI and tractography for the assessment of principal and shear strains in human muscle, in vivo along with muscle fiber direction strains 10

1.5.3 FEM analyses of passive muscle for an assessment of principles of the effects of muscle relative position changes on length changes along muscle fascicles. 11
1.5.4 FEM analyses for assessment of titin's role in a three-filament para-digm of muscle contraction 11
1.6 List of Publications Produced From the Thesis 12
1.6.1 Journal publications 12
1.6.1.1 First author 12
1.6.1.2 Not first author 12
1.6.2 Conference Proceedings 13
1.6.2.1 First author 13
1.6.2.2 Not first author 15
1.6.2.3 Not presenting author 16
2. MAGNETIC RESONANCE IMAGE ANALYSES AND ASSESSMENT OF LOCAL PRINCIPAL STRAINS WITHIN LOWER LEG MUSCULATURE RESULTING FROM EXTERNALLY APPLIED LOAD IN VIVO 17
2.1 Introduction 17
2.2 Methods 18
2.2.1 Volunteers 18
2.2.2 Experimental protocol 19
2.2.3 Image acquisition 20
2.2.4 Calculation of in vivo deformations 20
2.2.5 Calculation of algorithm artifacts 24
2.2.6 Calculation of volunteer repositioning artifacts 25
2.2.7 Statistics 25
2.3 Results 25
2.4 Discussion 28
3. MAGNETIC RESONANCE AND DIFFUSION TENSOR IMAGE ANALYSES AND ASSESSMENT OF LOCAL ALONG-FIBER MUSCLE STRAINS RESULTING FROM JOINT ANGLE MANIPULATION IN VIVO 35
3.1 Introduction 35
3.2 Materials and Methods 36

3.2.1 Volunteers . . . 36
3.2.2 Experimental protocol . . . 36
3.2.3 MR and DT image acquisition . . . 37
3.3 Calculation . . . 38
3.3.1 Calculation of deformations . . . 38
3.3.2 Determination of muscle fiber directions . . . 40
3.3.3 Calculation of strains . . . 41
3.3.4 Testing of MRI noise artifacts and repeatability . . . 43
3.3.5 Calculation of artifacts . . . 43
3.3.6 Statistics . . . 44
3.4 Results . . . 45
3.5 Discussion . . . 49
3.5.1 Methodology developed . . . 49
3.5.2 Explanations for inhomogeneity of muscle fiber direction strains 52
3.5.3 Limitations and implications . . . 55
4. FINITE ELEMENT MODELING ASSESSMENT OF THE MECHANISM OF COMBINED LOCAL LENGTHENING AND SHORTENING ALONG MUSCLE FIBERS . . . 58
4.1 Introduction . . . 58
4.2 Methods . . . 59
4.2.1 Description of the “linked fiber–matrix mesh model” . . . 59
4.2.2 Myofiber element . . . 60
4.2.3 ECM element . . . 61
4.2.4 Elements linking fiber and matrix meshes . . . 64
4.2.5 Aponeurosis element . . . 64
4.2.6 Model of EDL muscle with extra-muscular connections . . . 64
4.2.7 Solution procedure . . . 65
4.2.8 Processing of data . . . 66
4.3 Results . . . 66
4.3.1 Strain along serial fascicle sections I–IV . . . 66
4.4 Discussion . . . 67
5. FINITE ELEMENT ASSESSMENT OF TITIN’S POTENTIAL ROLE IN

MUSCLE'S FORCE PRODUCTION 71
5.1 Introduction 71
5.2 Methodology: Linked Fiber–Matrix Mesh Finite Element Model 73
5.2.1 Myofiber Element 73
5.2.2 ECM element 77
5.2.3 Elements linking the fiber and matrix meshes 79
5.2.4 Aponeurosis element 79
5.2.5 Model of isolated EDL muscle 79
5.2.6 Reference model with passive state titin vs. extended models incorporating active state titin 80
5.2.6.1 Stiffened titin case 80
5.2.6.2 Stiffened titin case with extra-muscular linkages 80
5.2.6.3 Shifted titin case 81
5.2.7 Solution procedure 81
5.2.8 Processing of data 82
5.3 Results 82
5.3.1 Global: Effects of active state titin on muscle length–force . . . 82
5.3.1.1 Stiffened titin case 82
5.3.1.2 Stiffened titin case with extra-muscular linkages 83
5.3.1.3 Shifted titin case 83
5.3.2 Local: mechanism of RFE based on muscle fiber direction strains and stresses 85
5.3.2.1 Stiffened titin case local strain and stresses 85
5.3.2.2 Stiffened titin relative position change case local strain and stresses 86
5.3.2.3 Shifted titin case local strains and stresses 87
5.4 Discussion 90
6. GENERAL DISCUSSION 94
6.1 Continuity and Integrity of Fascial Networks within Human Lower Limb 94
6.2 Use of Advanced MRI and DTI Analyses Methodologies for the Assessment of Deformations in Human Limb 94
APPENDIX A. DISTRIBUTION OF PRINCIPAL STRAINS IN LOWER LEG

AFTER KINESIO TAPE APPLICATION 97
APPENDIX B. MAGNETIC RESONANCE AND DIFFUSION TENSOR IMAGING FOR ASSESSMENT OF VOLUNTARY SUB-MAXIMAL ISOMETRIC PLANTAR-FLEXION IN VIVO 99
APPENDIX C. MAGNETIC RESONANCE AND DIFFUSION TENSOR IMAGING FOR ASSESSMENT OF VOLUNTARY CYCLIC JOINT MOTION 102
C.1 MRI Compatible Joint Angle Measurement 102
C.2 Motion Triggering of MRI Device 103
APPENDIX D. DETERMINATION OF ACTIVE STATE STIFFENED TITIN CONSTITUTIVE EQUATION 106
REFERENCES 109

LIST OF FIGURES

Figure 2.1	Illustrations of volunteer positioning in MR scanner and KT application.	21
Figure 2.2	Anatomical regions studied.	22
Figure 2.3	Flowchart for image acquisition and data processing steps.	23
Figure 2.4	Effects of KT application in terms of local tissue deformations.	27
Figure 2.5	Distributions of local tissue deformations due to KT application per volunteer. The deformation fields belong to Volunteer A.	28
Figure 2.6	Comparison of key tissue deformations across volunteers for inter-subject variability.	29
Figure 3.1	Illustrations of volunteer positioning in MR scanner and the anatomical region studied.	38
Figure 3.2	Results of the repeatability test.	44
Figure 3.3	(a) Left panel: strain errors. Right panel: strains along GM fibers due to imposed knee angle change. (b) Distribution of fiber direction strains of different nodes for pooled data from all volunteers.	46
Figure 3.4	Serial distribution of fiber direction strain. (A)–(E) Fiber direction strains are mapped on identified GM tracts separately for each volunteer.	47
Figure 3.5	Along-fiber shear strain distributions. (A)–(E) Along-fiber shear strains are mapped on identified GM tracts separately for each volunteer.	48
Figure 3.6	Distributions of mean fiber direction strains of different tracts from pooled data from all volunteers.	48
Figure 3.7	Parallel distribution of fiber direction strain among different GM fiber tracts per volunteer.	50
Figure 3.8	Distribution of deep GM aponeurosis strains per volunteer.	51
Figure 4.1	Stress–strain relation for intra-cellular passive elements representing titin in the myofiber element.	61

Figure 4.2	ECM element's stress–strain relations in cross-fiber and thickness, along-fiber, and shear directions.	63
Figure 4.3	Geometry of the rat EDL model studied.	65
Figure 4.4	Nodal fiber direction strains per serial sections I–IV vs. fascicle interface curves at long muscle length without (a) and with (c) relative position change.	67
Figure 4.5	Fiber direction strain and stress contour plots for model with extra-muscular connections, after 7 mm distal relative position change and subsequently lengthening to L_{opt} + 0.5 mm.	68
Figure 5.1	Geometry of the rat EDL model studied.	74
Figure 5.2	Active stress–strain properties of the myofiber element representing the contractile apparatus.	75
Figure 5.3	Stress–strain relation of intra-cellular titin in myofiber domain for reference passive and stiffened active states.	77
Figure 5.4	Stress–strain relation of intra-cellular titin in myofiber domain for passive and shifted active states.	77
Figure 5.5	Active muscle force decreases beyond optimum length with no apparent shift in muscle optimum length for stiffened titin case.	82
Figure 5.6	Muscle length vs total, active, and passive force results for reference and stiffened titin in muscle relative position change models.	83
Figure 5.7	Total force–length characteristics of modeled EDL muscles in the range of muscle lengths studied, L_{opt} and $L_{opt} + 2$ mm. Inset: Active muscle force–length characteristics for no pre-stretch and high pre-stretch case muscles.	84
Figure 5.8	Mean nodal fiber direction strain/stresses vs. fascicle interface curves at long ($L_{opt} + 3.2$ mm) muscle length.	85
Figure 5.9	Contour plots of reference titin (top plots) and stiffened titin (bottom plots) cases showing (a) fiber direction strain (ϵ_{22}), (b) total fiber direction stress (σ_{22}), (c) stress due to actin–myosin contractile apparatus ($\sigma_{22contr}$), (d) stress due to titin ($\sigma_{22titin}$).	85

Figure 5.10 Nodal fiber direction strain per fascicle interface for stiffened and reference titin cases in active lengthening after muscle relative position change. 86

Figure 5.11 Nodal fiber direction total stress per fascicle interface for stiffened and reference titin cases in active lengthening after muscle relative position change. 86

Figure 5.12 Nodal fiber direction titin stress per fascicle interface for stiffened and reference titin cases in active lengthening after muscle relative position change. 86

Figure 5.13 Total muscle force and mean fiber direction nodal strain/stresses vs. fascicle interface curves at long ($L_{opt} + 2$ mm) muscle length. 87

Figure 5.14 Total muscle force and mean fiber direction nodal strain/stresses vs. fascicle interface curves back at original (L_{opt}) muscle length. 89

Figure A.1 Distributions of local tissue deformations due to KT application per volunteer. Deformation fields belong to Volunteer B. 97

Figure A.2 Distributions of local tissue deformations due to KT application per volunteer. Deformation fields belong to Volunteer C. 97

Figure A.3 Distributions of local tissue deformations due to KT application per volunteer. Deformation fields belong to Volunteer D. 98

Figure A.4 Distributions of local tissue deformations due to KT application per volunteer. Deformation fields belong to Volunteer E. 98

Figure B.1 Distributions of GM fiber direction strains (top left), and also first principal strains for local tissue deformations on NVTs (bottom left) due to sub-maximal plantar-flexion activity for one volunteer. Top panels provide anterior view whereas bottom panels provide posterior view. 99

Figure B.2 Distributions of GM fiber direction strains, along with NVTs and local lengthening on them (top panels), and their intersections with GM tracts seen from posterior (bottom panel) view for the volunteer in Figure B.1. 100

Figure B.3 Distributions of GM fiber direction strains (top panels), along with NVTs and their intersections (bottom panels) with GM tracts seen from posterior (left) and anterior (right) views for another volunteer. 101

Figure C.1 Motion guiding fixation device (left) and recorded angular information by fiber-optic rotary encoder (right, top) along with resulting trigger waveforms (right, bottom). 102

Figure C.2 External trigger signal characteristics used in the study as required by for the Siemens Trio 3 T device. 103

Figure C.3 (a) Magnitude image belonging to phase images, (b) x direction phase image, (c) y directon phase image and (d) z direction phase image. x, y and z directions correspond to medio–lateral, anterior–posterior and inferior–superior anatomical directions inside the MRI device, respectively. 104

Figure C.4 Distributions of GM and SOL fiber direction strains during plantarflexion phase of voluntary cyclic ankle plantar- and dorsi-flexion, displayed on a sagittal slice. 105

Figure D.1 Active stretch (red) simulations for different muscle lengths at start of activation (corresponding to initial fiber direction strains of 1.0, 1.1, 1.2, 1.3, 1.4). Isometric stressâstrain relations determined from continuum mechanical model (bold black) along with the active stress (black) obtained by subtracting passive stress (blue) from total stress are depicted. 106

Figure D.2 Stress–strain relation for myofibrils stretched (i) in low [Ca^{2+}] solution (passive stretch, triangles), and in high [Ca^{2+}] solution from an initial sarcomere length of (ii) 2.4 μm (active stretch, circles) and (iii) 3.4 μm (active stretch from 3.4 μm, squares). Stresses are normalized to isometric total stress at 2.4 μm. Data acquired from [1]. 107

Figure D.3 Stress–strain constitutive equation of active state stiffened titin (Eq. 5.3) for active lengthening starting at 2.4 μm sarcomere length, acquired by subtracting passive force (Figure D.2) and actin–myosin cross-bridge force (Figure D.1) form total force (Figure D.2). 107

LIST OF TABLES

Table 2.1	Anthropometric data.	19
Table 2.2	Parameters used in FLASH sequence. Note that no fat suppression and a choice of high bandwidth (41 600 Hz) were used. Number of averages = 1.	20
Table 2.3	Algorithm (top) and subject repositioning (middle) artifacts compared to in vivo strains due to KT application (bottom) for KT-to-TA region (left), TA (middle) and nonâtargeted tissues (right).	26
Table 3.1	Anthropometric data.	37
Table 3.2	MR and DT imaging parameters. [a]Resampled 128 x 128.	39
Table 4.1	Values and definitions of the model constants.	62
Table 5.1	Values and definitions of the model constants.	76
Table C.1	PC and DT imaging parameters.	104

LIST OF SYMBOLS

T	Tesla
Hz	Hertz
cm	centimeter
mm	millimeter
mm^2	square millimeter
mm^3	cubic millimeter
μm	micrometer
s	second
kg	kilogram
$^\circ$	degree
v_{enc}	velocity encoding
$\otimes$	cross-product
N	Newton
I	unit tensor
F	deformation gradient tensor
E	strain tensor
E_1	first principal strain
E_3	third principal strain
V	volume
dV, ΔV	volume change
L_{opt}	optimum muscle length
$F_{ref}@L_{opt}$	total force of reference model at L_{opt}
t_1, t_2, t_3	stress–strain relation coefficients of the intra-cellular titin within myofiber elements in passive state
h_1, h_2, h_3	stress–strain relation coefficients of the intra-cellular titin within myofiber elements in active state
b_1, b_2, b_3	stress–strain relation coefficients of the contractile apparatus within myofiber elements

a_{11}	passive cross-fiber stiffness
a_{12}	passive fiber–cross-fiber shear stiffness
a_{22}	passive fiber direction stiffness
W	strain energy density function for ECM element
k	initial passive stiffness for ECM element
$\underline{L}^G$	Green–Lagrange strain tensor
$\underline{S}$	second Piola–Kirchoff stress
I_3^{avg}	third invariant of right Cauchy–Green strain tensor
M	fiber tract direction
C	right Cauchy–Green strain tensor
J	Jacobian determinant of deformation
B_1	along-fiber shear strain
I_4	strain invariant defining along-fiber shear strain
I_5	strain invariant defining orientation of the along-fiber shear plane relative to cross-fiber shear diagonals
$\hat{n}$	unit normal vector
$\hat{r}$	local along-fiber tangent unit vector
$[Ca^{2+}]$	calcium ion

π	pi
ϵ	strain
ϵ_{22}	along-fiber strain
ϵ_{shift}	strees–strain relation shift coefficient of the intra-cellular titin within myofiber elements in shifted active state
σ	stress
σ_{22}	along-fiber stress
$\sigma_{22contr}$	contractile apparatus component of along-fiber stress
$\sigma_{22titin}$	titin component of along-fiber stress
$\sum \sigma_{22}$	sum of nodal along-fiber stresses
λ_S	weight factor in the penalty function for the solid volume
λ_F	weight factor in the penalty function for the fluid volume

ψ	magnitude of along fiber shear strain
λ_M	magnitude of uniaxial fiber stretch
θ	fiber tract pennation angle

LIST OF ABBREVIATIONS

EMFT	Epimuscular Myofascial Force Transmission
MRI	Magnetic Resonance Imaging
DTI	Diffusion Tensor Imaging
DWI	Diffusion Weighted Imaging
FEM	Finite Element Modeling
LFMM	Linked Fiber-Matrix Mesh
MTJ	MyoTendinous Junction
KT	Kinesio Tape
ECM	Extra-Cellular Matrix
CV	Coefficient of Variation
EDL	Extensor Digitorum Longus muscle
GM	Gastrocnemius muscle Medial head
SOL	Soleus muscle
TA	Tibialis Anterior muscle
MVC	Maximum Voluntary Contraction
PC	Phase-Contrast
MRA	Magnetic Resonance Angiography
DENSE	Displacement ENcoding with Stimulated Echoes
RFE	Residual Force Enhancement
Turbo FLASH	Turbo Fast Low-Angle Shot
ss-EPI	single shot-Echo Planar Imaging
FA	Fractional Anisotropy
2D	Two-Dimensional
3D	Three-Dimensional
SD	Standard Deviation
NVT	Neuro-Vascular Tract
US	UltraSound

1. OVERVIEW

1.1 Anatomy of Muscle and Surrounding Tissue

Muscle is the motor that produces the force driving skeleton's motion and is composed of muscle fibers and extra-cellular matrix (ECM). The ECM is a three dimensional scaffold of connective tissue within which muscle fibers operate [2]. Each muscle fiber is composed of a serial arrangement of its smallest functional units: the sarcomere. Force production capacity of the sarcomere is maximal between 2.25–2.50 μm and is considered to decrease linearly outside this length range [3]. Sarcomere's force producing active lattice is composed of actin and myosin myofilaments and force is produced via the cross-bridges formed between these myofilaments under the influence of calcium and is dependent on the overlap between actin and myosin filaments. Thus, sarcomere length is a fundamental metric in muscle mechanics. This classical viewpoint is based on two fundamental assumptions:

1. Presence of calcium affects only actin and myosin, thus contraction is traditionally considered as a two-myofilament paradigm [3, 4, 5, 6]. However calcium dependence of titin is known [7, 8, 9] and contraction is spreadingly described accordingly as a three-myofilament paradigm [1, 10, 11, 12, 13, 14, 15, 16, 17]. Studies regarding how deformations within muscle change when taking titin into consideration are scarce and limited to cubic volume of parallel fibered muscle for excising muscle geometry related concerns [18, 19].

2. Lengths of sarcomeres are determined solely by the mechanical interaction among serially arranged sarcomeres of the same myofibril. However, due to connecting protein structures that exist between muscle fibers and the ECM, each sarcomere would be in mechanical interaction both with the ECM and through the ECM, also with sarcomeres within other muscle fibers. Thus, sarcomere length would be determined by a more complex mechanism.

Based on these, overall, our research group proposes to steer towards describing contraction as a four-myofilament paradigm. Muscle deformation analyses regarding such mechanisms are scarce if not lacking. It must further be noted that there are various connections beyond myofiber–ECM connection, hence the issue is also about the mechanism for transmission of muscle force. Within the composite structure of muscle tissue, muscle fibers are attached to the ECM via multi-molecular connections. Ability of these connections to transmit force laterally between muscle fibers were shown for isolated singe fibers [20], muscle fiber bundles [21] and whole muscle in situ [2, 22, 23]. Finite element model accounting for muscle's composite structure showed the effects of such intra-muscular myofascial force transmission leading to e.g., a heterogeneous strain distribution within muscle with homogeneous material [24].

Connective tissues of muscle are continuous structures and combine to form aponeurosis and tendon, where muscle fibers are connected. Such myotendinious connections are specialized for transmitting force developed within the muscle fibers to the tendon and from there to the bone and eventually to the joint [25] While importance of such myotendinous force transmission pathway is evident, assuming it is the only available pathway for transmitting forces generated in sarcomeres is an overstatement. Classical view on muscle mechanics states that muscle fibers and the ECM are connected at the myotendinious junction exclusively, which leads to the assumption that muscle fibers are mechanically independent, hence the sarcomeres within a muscle fiber would all be of the same length. Furthermore, this classical view assumes that muscles are independent actuators; force produced by muscle is transmitted equally to both tendons; and length–force relationship of a muscle is unique [26].

The skin is considered largest organ in human body. Unequivocally second to it, is the fascial system [27], covering and sheathing all musculature within the limb. Appendages of circulatory, nervous and lymphatic systems, namely blood vessels, veins and capillaries; nerves; lymphatic vessels and ducts are enclosed in fasciæ, investing into muscles, bones and other organs and hence interlinking them mechanically. Skeletal muscle is part of an integral system which is comprised of muscular and non-muscular structures in vivo. Direct collageneous connections between epimysia

of adjacent neighboring muscles [28] and indirect connections between distant muscles via predominantly neuro-vascular tracts (NVT) and also through compartmental fascia continuous to this system provide pathways for transmission of force between muscles [28, 29]: inter-muscular myofascial force transmission. Non-muscular tissues such as inter-muscular septum, inter-osseal membrane, and bone are an integral part of this system allowing transmission of force [30]: if this can be isolated it is referred to as extra-muscular myofascial force transmission. Collectively known as epimuscular myofascial force transmission (EMFT) [28], inter- and extra-muscular myofascial force transmission (for a detailed review see [31, 32]) was shown to cause proximo–distal force differences in non-isolated muscles, where the force difference represents the net amount of force transmitted from the target muscle via myofascial pathways or this can be considered as a net amount of myofascial loads acting on the muscle belly [30] Increase in the difference between proximal and distal forces was observed when the position of the target muscle was changed isometrically relative to surrounding structures [33]. This indicates that stretching of the NVTs and other myofascial structures causes elevated loads to act on the muscle. One explanation for the experimentally observed force differences is that the net amount of the myofascial loads is integrated to the force measured in one of the tendons of the muscle. However, this is tenable only if the muscle were a rigid body. Instead, via the connective tissues comprising the muscle's ECM, which is integral to the epimuscular myofascial structures, the myofascial loads conceivably spread inside the muscle and lead to local effects. Those effects can be characterized as local deformations and their quantification is very important. Myofascial loads, considered as external forces on muscle effecting its interior, could be due to stretching of NVTs and other connective tissues caused by relative position change of that muscle with respect to other muscles, or could be entirely of external origin: an integral structure of connective tissue between skin and muscle's ECM could bring external forces applied on skin deeper into muscle level, and cause deformations intra-muscularly. KT is a well-suited example for this kind of loading. While numerous expectations and premises exist regarding KT's effects, how it causes deformations locally within muscle tissue is not known well and regarding studies are lacking. It is clear that if those deformations occur along the length of muscle fibers, the lengths of sarcomeres can vary. This is particularly relevant in terms of muscle function. There-

fore, quantification of local length changes along muscle fibers also is very important. Yet, achieving those without interfering with the integrity of the muscle and connective tissue system is very difficult experimentally. Two ways of such assessments are using medical imaging as an experimental tool and using finite element analyses for a computational modeling tool.

1.2 Imaging Modalities and Advanced Analysis Methodologies for Assessment of Local Deformations in Human Muscle in vivo

Due to their non-invasive nature, medical imaging modalities such as ultrasound (US) and magnetic resonance imaging (MRI) allow biomechanical studies in vivo without disrupting the structural integrity of target tissue.

1.2.1 Ultrasound

Comparison of muscle architectural parameters such as pennation angle and fiber length determined by US and by direct anatomical measurement yielded good agreement for human m. gastrocnemius medialis (GM) [34]. US imaging of triceps surae muscles at different ankle and knee joint combinations at rest and during maximal plantar-flexion effort has shown variation of architecture and function within the muscles of triceps suræ [35]. These results have been extended to show fascicle length changes in GM during eccentric contractions at extended and flexed knee positions [36]. Tissue displacements within triceps suræ muscles have been calculated by tracking US video images during passive knee extension and during selective electrical stimulation of GM, and have been found similar for GM and isometric and passive SOL muscles, suggesting force may inter-muscularly be transmitted between the muscles of triceps suræ in vivo [37].

1.2.2 Magnetic Resonance Imaging

US offers good spatial and temporal resolution as well as higher availability, lower cost and relative ease of operation during experiments with apparatus and/or within calibrated spaces designed for research in biomechanics. However, limitations such as tissue depth, transducer array size, and imaging of a single plane are some shortcomings of US. On the other hand, improvements in and availability of MRI hardware and imaging sequences have led to increased use of MRI for study of muscle anatomy and physiology in biomechanically relevant experimental settings. Thus, MRI offers a viable if not superior alternative to US in imaging of tissue architecture and displacements.

1.2.2.1 Calculation of local tissue strains in dynamic conditions.

Cine MRI synchronizes acquisition of images over many repetitions of cyclic motion and reconstructs the data in a series of anatomic images with desired number of time frames [38]. Other MRI modalities that were originally used for evaluation of myocardial function in vivo, such as phase-contrast (PC) in which displacements and strains are determined by space and time integral of pixel velocities encoded in phases of the image [39], and displacement encoding with stimulated echoes (DENSE) in which strain tensor is directly obtained from tissue displacement encoded in phases of the image [40], were recently utilized in imaging of skeletal muscle:

1. Using cine PC imaging during active elbow flexion, non-uniform strain patterns were observed along the centerline aponeurosis of m. biceps branchii but such non-uniformities were attributed to complex muscle–tendon architecture [41]. Cine PC MR images acquired during knee extension and flexion of healthy volunteers and of volunteers who had rectus femoris tendon transfer surgery showed that m. rectus femoris did not move in the direction of knee flexors, but this finding was explained with scar tissue formation around the muscle after surgery [42]. Outcomes of PC MRI and spin-tagging methods have been compared to validate

non-uniform strain patterns observed in deep and superficial aponeuroses of GM during sub-maximal isometric plantar-flexion effort [43].

2. Cine DENSE imaging of m. biceps branchii during low-load elbow flexion [44] was in agreement with similar cine PC study [41], and additionally, second principle strain was greater than first principle strain along centerline aponeurosis, suggesting changes in the nature of deformation within muscle, possibly due to shearing [44]. In a study on damage during eccentric activity, long head of biceps femoris muscle was assessed during active and passive lengthening using cine DENSE MRI and higher strains were observed during active lengthening compared to those during passive lengthening, along with higher and more localized strains for volunteers with narrower aponeurosis width compared to those with wider [45].

1.2.2.2 Calculation of local tissue strains in static conditions.

Static T1-weighted anatomic images were also recently used to quantify local deformations within triceps suræ muscles upon passive flexion of the knee while keeping ankle angle constant [46]. Tissue deformation was quantified using an intensity based non-rigid non-parametric image analysis tool: demons algorithm [47]. Strain tensors were also computed for image sets that went under synthetic rigid transformation and resulting deformation established baseline strains (error strains) for the algorithm. Significant differences are inquired in different regions of human distal lower limb, between algorithm error strains and strains calculated regarding two subsequent in vivo image sets, one of which is the image set whose deformation upon synthetic rigid transformation established the baseline error per image set. Strain distributions observed in GM, and also in globally isometric SOL, were heterogeneous suggesting occurrence of epimuscular myofascial force transmission in vivo. Furthermore, feasibility of demons algorithm for study of muscle mechanics was demonstrated.

1.2.2.3 Determination of muscle fiber direction.

Diffusion tensor imaging (DTI) is an MRI method that measures diffusivity of water molecules within biological tissue by application of diffusion sensitizing gradients in at least six directions, in addition to acquisition of at least one non-weighted diffusion image. Diffusion of free water molecules in tissue is limited by cell membranes and other structures [48]. Therefore, a tensor obtained from diffusion of water molecules within each voxel characterizes local architecture of tissue. Correspondence of the first eigenvector of the diffusion tensor to the average direction of local fibers were shown in animal [49] and cadaver supported human studies [50]. Galban et al. proposed that the second and third eigenvalues provided by DTI corresponded to structural information about the endomysium and average fiber diameter respectively [51], in concert with DTI findings regarding the myocardial architecture [52]. Significant decrease in the second eigenvalue of m. tibialis anterior (TA) upon passive plantar-flexion has been reported [53][53]. Moreover, the third eigenvalue showed a larger increase in mouse TA after severe ischemic stress and it showed high correlation with the damage observed in histological slices [54]. For passively plantar- and dorsi-flexed human lower leg muscles, Schwenzer et al. reported no change in the first eigenvalue and a decrease in the second and third eigenvalues in the stretched muscle groups [55]. Damon et al. presented feasibility and validation of tractography for determination of pennation angles of muscle fibers using DTI [56]. Repeatability of measuring muscle architectural of parameters such as pennation angle and fiber track length were demonstrated [57]. Importance of high signal-to-noise ratio for tractography purposes was underlined [58]. Performance of different b-values, which defines the diffusion weighting of images, were compared for signal-to-noise ratio at different magnetic field strengths [59]. Froeling et al. demonstrated computational methods for noise reduction to hasten DTI acquisition, suggesting its potential in clinical use [60]. Muscle architecture was constructed for TA [61] and even for SOL [62, 63], despite its complex structure. Kan et al. used DTI parameters to address changes in quadriceps femoris muscle group mechanics in volunteers with lateral patellar dislocation [64]. In sum, use of DTI is presented as a feasible method to characterize muscle architecture.

1.2.2.4 MRI–DTI to determine local length changes along muscle fibers.

In order to assess effects of EMFT in vivo, experiments are designed similar to previous animal experiments where relative position of a muscle is changed while its synergists are kept isometric. Position of a bi-articular muscle can be changed in relation to its mono-articular synergists by manipulating angle of the joint the mono-articular synergist does not cross. Triceps suræ offers such opportunity: m. gastrocnemius (GAS) and m. soleus (SOL) are both ankle plantar-flexors, however SOL is mono-articular and does not cross the knee joint. Upon manipulation of knee angle, only bi-articular GAS changes length, and rest of the lower leg musculature is kept isometric. Any deformation observed in the lower leg musculature would be indication of EMFT. Further experimental scenarios are of active muscle contraction and/or joint motion during the image acquisition are to be further assessed.

1.3 Finite element method as a tool for calculation of muscle deformations

Finite element modeling (FEM) is a numerical analysis method which allows comprehensive mechanical assessment of tissues under various constraints and loading conditions. Muscle's fiber embedded ECM morphology provides grounds for a bi-domain formulation, considering the active myofiber and passive ECM domains as separate mechanical entities related mechanically with each other via interconnections at element nodes, with a penalty function applied to ECM domain adequately ensuring volume constancy of muscle tissue. Using this bi-domain continuum mechanical formulation of muscle in isometric fully contracting and also in passive states provides ample opportunity to investigate heterogeneity of strains also separately within myofiber elements yielding separate stress contributions from titin and actin–myosin cross-bridges, which in sum accounts for sarcomeres' force production. Furthermore, addition of inter- and extra-muscular linkages representing collagenous connectivity between muscles, or between muscle and non-muscular composure such as NVTs respectively, allows study-

ing effects of muscle relative position change on internal mechanics of muscle tissue and also on total muscle force transmitted to the MTJ. As such FEM allows simulation of many phenomena otherwise inaccessible, granting perspective on underlying principles of mechanical interaction within muscle tissue upon interventions such as botulinum toxin induced paralysis and subsequent adaptations [65, 66], or aponeurotomy [67, 68], thus promoting FEM as a powerful tool for analyses of muscle deformations.

1.4 Aims of the Thesis

Based on the background summarized above and the gaps in our understanding of skeletal muscle mechanics the thesis work aims at the following:

1. In vivo assessment of local muscle tissue deformations resulting from an externally imposed loading via MRI analyses of KT effects on targeted as well as non-targeted human muscles of the lower leg.

2. In vivo assessment of local intramuscular deformations in human muscle, specifically length changes in the muscle fiber direction imposed by changes in joint configurations in the passive state.

3. FEM assessment of principles of the mechanisms of in vivo findings showing heterogeneous length changes along the muscle fiber direction.

4. Development of FEM analyses towards quantification of muscle deformations for various contraction paradigms involving two, three and four myofilaments, for an assessment of effects of calcium dependent changes in titin's mechanical behavior in the context of EMFT.

5. Development of in vivo methodologies to study effects of joint motion in terms of local muscle deformations in the active state in human.

1.5 Thesis Overview

1.5.1 MRI registration applied to human muscles in vivo and subsequent analyses for assessment of KT effects in terms of principal strains developing in the tissues of the lower leg

The first aim of the thesis is addressed by combining MRI analyses and a KT application. MRI, and and subsequent image registration and analyses allowed quantification of principal tissue deformations upon externally applied mechanical load. Spread of these external loads locally and in various anatomical directions within muscle and nonmuscular tissue are discussed within context of myofascial integrity in Chapter 2, along with presentations of principal strains per volunteer in Appendix A.

1.5.2 MRI techniques combined with DTI and tractography for the assessment of principal and shear strains in human muscle, in vivo along with muscle fiber direction strains

The second aim of the thesis is addressed by combining MRI and DTI analyses. Diffusion tensor imaging and subsequent tractography combined with MRI registration techniques allowed determination of muscle deformation in fiber direction as well as shear directions upon single passive knee extension. Principal strains were also determined on aponeuroses. Findings are presented in Chapter 3. Similar analyses were also carried out data acquired during sustained sub-maximal plantar-flexion activity. Exemplary findings of first principal strains on neuro-vascular tracts have been presented in relation to fiber direction muscle strains in Appendix B.

Note that addressing also the fifth aim of the thesis, methods for assessment of deformations arising during cyclic ankle flexion were developed and the outcome is exemplified with a preliminary work presented in Appendix C.

1.5.3 FEM analyses of passive muscle for an assessment of principles of the effects of muscle relative position changes on length changes along muscle fascicles.

The third aim of the thesis is addressed by extending the existing finite element model of our group. Muscle fascicles with lengthening and shortening sections in a passively lengthened muscle, while counter-intuitive at first glance, does have mechanical reasons behind. In silico analyses allow full control over model constraints and extensive access to underlying mechanical metrics, particularly stress and strain. In this case, continuum model bi-domain finite element model with myofibers embedded into the ECM, namely linked fiber–matrix mesh model (LFMM) [24], can help understand how lengthening and shortening sections within passively lengthening fascicles could coexist. To address this, Chapter 4 aims studying the effects of muscle relative position change with certain lengthening of passive EDL muscle of the rat using FEM methodology. An increased understanding of local mechanics within muscle and its anatomical relations to extra-muscular linkages, particularly NVTs, helps illustrate the plausible role of epimuscular myofascial loads on imposing locally shortening regions within a longer muscle.

1.5.4 FEM analyses for assessment of titin's role in a three-filament paradigm of muscle contraction

The fourth aim of the thesis is addressed by comparing the existing two-myofilament (actin and myosin) model approach to a newly developed three-myofilament (titin's altered properties caused by muscle activation are added) model, and by a first implementation of this to an extramuscularly connected muscle model (considering muscle fiber–ECM linkages as the fourth myofilament). Further assessment using this bi-domain continuum mechanical formulation of muscle in isometric maximal contraction provided ample opportunity to further investigate heterogeneity of strains also separately within myofiber elements that account for the sarcomere, with different formulation for contractile apparatus (actin–myosin cross-bridge force) and titin

contributions to produced muscle force. Findings are discussed within three-filament paradigm of muscle and titin's additional and possibly nonuniform role in non-isometric muscle activity is underlined in Chapter 5, with details regarding formulation of titin's constitutive equation in Appendix D.

1.6 List of Publications Produced From the Thesis

1.6.1 Journal publications

1.6.1.1 First author.

1. "MRI analyses show that kinesio taping affects much more than just the targeted superficial tissues and causes heterogeneous deformations within the whole limb", U. Pamuk and C. A. Yucesoy, Journal of Biomechanics, Vol. 48(16): pp. 4262-70, 2015.

2. "Combined magnetic resonance and diffusion tensor imaging analyses provide a powerful tool for in vivo assessment of deformation along human muscle fibers", U. Pamuk, A. Karakuzu, C. Ozturk, B. Acar, C. A. Yucesoy, Journal of Mechanical Behavior of Biomedical Materials, Vol. 63, pp. 207-219, 2016.

1.6.1.2 Not first author.

3. "Magnetic resonance and diffusion tensor imaging analyses indicate heterogeneous strains along human medial gastrocnemius fascicles caused by submaximal plantar-flexion activity", A. Karakuzu, U. Pamuk. C. Ozturk, B. Acar, C. A. Yucesoy, Journal of Biomechanics, Vol. 57, pp. 69-78, 2017

1.6.2 Conference Proceedings

1.6.2.1 First author.

4. "Finite element analyses of active state titin reveals previously unconsidered important effects on muscle mechanics", U. Pamuk and C. A. Yucesoy, Uluslararası Katılımlı 9. Ulusal Biyomekanik Kongresi (UBK 2018), p. 179, Sep 19-22, 2018. (accessed on 02.12.2018) http://www.biomeccon.org/2018/Biomeccon.pdf

5. "Assessment of mechanism of force enhancement due to active state stiffened titin using linked fiber–matrix mesh model", U. Pamuk and C. A. Yucesoy, World Congress of Biomechanics, WCB, 8th biennial WCB, Musculoskeletal biomechanics across the scales, poster no. 2190, Jul 08-12, 2018, (accessed on 02.12.2018) https://app.oxfordabstracts.com/stages/123/programme-builder/submission/22147?backHref=/events/123/sessions/680&view=published

6. "Effects of variation of stretch and activation level on human gastrocnemius geometric and mechanical metrics", U. Pamuk, A. Karakuzu, C. A. Yucesoy, editor J. Ojeda, European Society of Biomechanics, ESB, 23rd annual congress of ESB, YÖK yayın ID: 4150430, 2-5 Jul 2017, (accessed on 02.12.2018) https://esbiomech.org/conference/archive/2017seville/papers/1665-4570-1-PB.pdf

7. "Kinesio taping as a superficial loading on the skin causes multi-directional and heterogeneous local tissue length changes within the entire limb", U. Pamuk and C. A. Yucesoy, Uluslararası Katılımlı 8. Ulusal Biyomekanik Kongresi, UBK 2016, SP5, pp. 78-81, 19-23 Oct 2016, (accessed on 04.12.2018) https://web.archive.org/web/20170517161812/http://www.eaorganization.net/ubk/UBK_2016-Bildiri_Kitabi.pdf

8. "Kinesio tape: What does it actually do mechanically?", U. Pamuk and C. A. Yucesoy, European College of Sport Science, ECSS, 21st annual congress of ECSS, p. 477, Jul 06-09, 2016, (accessed on 02.12.2018) http://wp1191596.server-he.de/DATA/CONGRESSES/VIENNA_2016/DOCUMENTS/VIENNA_BoA.pdf

9. “MRI and DTI analyses combined provide a powerful tool for quantifying deformation along human muscle fibers in vivo”, U. Pamuk, A. Karakuzu, B. Acar, C. Ozturk, C. A. Yucesoy, International Society of Biomechanics, ISB, XXVth biennial international congress of ISB, pp. 903-904, Jul 12-16, 2015, (accessed on 02.12.2018) https://isbweb.org/activities/congresses
https://isbweb.org/images/conferences/isb-congresses/2015/
isb_2015_abstract_book_final.pdf

10. “MRI analyses indicate non-uniform human muscle tissue deformations and confirm theoretically anticipated sarcomere length heterogeneity, in vivo”, U. Pamuk, A. Karakuzu, P. Akyazi, B. Acar, C. Ozturk, C. A. Yucesoy, 18th National Biomedical Engineering Meeting, BIYOMUT, SP9, p. 35, Oct 16-17, 2014, (accessed on 02.12.2018) 10.1109/BIYOMUT.2014.7026392,
http://www.biyomut2014.boun.edu.tr/BIYOMUT2014/Bildiri_Kitapcg_files/
BIYOMUT2014_OzetKitabi.pdf

11. “Magnetic resonance imaging analyses confirm so far theoretically posed intermuscular interaction effecs, in vivo”, U. Pamuk, A. Karakuzu, P. Akyazi, B. Acar, C. Ozturk, C. A. Yucesoy, International Society of Electrophysiology and Kinesiology, ISEK, XX ISEK congress, p. 81, Jul 15-18, 2014, (accessed on 02.12.2018)
https://isek.org/past-conferences/
https://isek.org/wp-content/uploads/2015/10/ISEK2014Rome.zip

12. “Quantification using MRI analyses shows complex and widespread mechanical effects of kinesio taping within a whole limb”, U. Pamuk, A. A. Çörekçi, A. Arpak, C. Ozturk, C. A. Yucesoy, International Society of Biomechanics, ISB, XXIVth biennial international congress of ISB, poster session 1, poster no. 70, Aug 04-09, 2013, (accessed on 02.12.2018)
https://isbweb.org/congress-proceedings/152-isb-2013/
390-isb-2013-brazil-poster-session-1
https://isbweb.org/images/conferences/isb-congresses/2013/poster/ps1-08l.pdf

1.6.2.2 Not first author.

13. "Intra- and epimuscular connective tissues are not just passive structural elements, but interfere with, and affect muscle's active mechanics", C. A. Yucesoy, A. Karakuzu, U. Pamuk, World Congress of Biomechanics, WCB, 8th biennial WCB. Mechanics of passive muscle and connective tissue 1, Jul 08-12, 2018, (accessed on 02.12.2018)
https://app.oxfordabstracts.com/stages/123/programme-builder/submission/19761?backHref=/events/123/programme-builder/view/sort/author&view=published

14. "Tensiomyographic assessment of changes in muscle tonus and rate of force production due to kinesio taping", S. Yıldız, U. Pamuk, G. Baltacı, C. A. Yucesoy, World Congress of Biomechanics, WCB, 8th biennial WCB. Medical device / soft tissue interaction, poster no. 4231, Jul 08-12, 2018, (accessed on 02.12.2018)
https://app.oxfordabs tracts.com/stages/123/programme-builder/submission/21470?backHref=/events/123/programme-builder/view/sort/author&view=published

15. "Assessment of in-vivo skeletal muscle mechanics during joint motion using multimodal magnetic resonance imaging based approaches", A. Karakuzu, U. Pamuk, C. Ozturk, C. A. Yucesoy, 18th National Biomedical Engineering Meeting, BIYOMUT, SP7, p. 34, Oct 16-17. 2014, (accessed on 02.12.2018)
10.1109/BIYOMUT.2014.7026373
http://www.biyomut2014.boun.edu.tr/BIYOMUT2014/Bildiri_Kitapcg_files/BIYOMUT2014_OzetKitabi.pdf

1.6.2.3 Not presenting author.

16. “Muscles’ activation state affects medial gastrocnemius fiber strain heterogeneity: Assessment using MRI and DTI methods”, U. Pamuk, A. Karakuzu, G. Sanlı, C. A.Yucesoy, International Society of Biomechanics, ISB, XXVIth biannual international congress of ISB, p. 107, Jul 23-27, Brisbane 2017, (accessed on 02.12.2018) https://isbweb.org/images/conferences/isb-congresses/2017/ISB2017-Full-Abstract-Book.pdf

2. MAGNETIC RESONANCE IMAGE ANALYSES AND ASSESSMENT OF LOCAL PRINCIPAL STRAINS WITHIN LOWER LEG MUSCULATURE RESULTING FROM EXTERNALLY APPLIED LOAD IN VIVO

2.1 Introduction

Kinesio taping (KT) (for a review see [69, 70]) has been increasingly used in the treatment of sports injuries and various neuro-musculoskeletal disorders. However, objective assessments of its effects have been sparse. Studied physiological outcome measures agree with the expected benefits such as improved muscle strength [71, 72] and activity [72, 73], increased range of motion [72, 74, 75], better force sensing [76], scar healing [77], increased lymph flow [78] and reduced pain [74, 75, 79]. Yet, other studies argue that the changes may be too small to be clinically beneficial [74], or even show no changes e.g., in muscle strength [76] and activity [80, 81, 82], nerve conduction [83] and joint position sense [71, 84].

Alexander et al. [80, 81] showed an inhibitory effect of taping on trapezius and gastrocnemius muscles. This suggests that taping causes deformations within the target muscle, a component of which affects muscle fibers. For this to occur, forces applied by the tape over the skin must be transmitted to deeper layers of muscle tissue. On the other hand, KT effects outside the target muscle are often ascribed to neurological mechanisms triggered by the effects on the target muscle [85, 86]. Mechanical effects of KT beyond the targeted tissues are not known objectively. Muscles packed within a limb can impose loads on each other via their contacting surfaces. This can reflect particularly normal forces originating from KT inside the limb. Additionally, continuity of the extra-cellular matrix (ECM) with epimuscular connective tissues [87, 88] and muscle fibers [21, 23, 89] allows myofascial force transmission (MFT) (for details see [31, 33]). Animal experiments showed major inter-synergistic [90] and inter-

antagonistic [91] MFT, within an entire limb [92]. This can reflect both normal and tangential forces originating from KT to the targeted tissues and from there, to other tissues elsewhere within the limb. Recent magnetic resonance imaging (MRI) studies indicate heterogeneous local deformations, upon changing exclusively the knee angle, not only within m. gastrocnemius, but also within its synergistic [46] and antagonistic muscles [93]. Therefore, mechanical loading imposed selectively can have widespread heterogeneous effects.

We consider that by operationalizing such mechanisms, KT initiates mechanical effects distributed within a limb. Proposed benefits may rely directly on local deformations (e.g., in tissue alignment), or on their translation into sensory (e.g., by increasing space over the area of pain, or directing the exudate to a lymph duct) or proprioceptive (e.g., by loading or unloading of mechanoreceptors) effects. However, comprehensive assessments of mechanical effects of KT are lacking which obscures understanding of the mechanism of imposed effects on the underlying tissues. Therefore, our goal was to characterize the mechanical effects of KT objectively using MRI analyses. Specifically, we aimed at testing the hypotheses that KT causes acutely local deformations not necessarily

1. in agreement with tape adhering direction and
2. limited to the directly targeted tissues.

2.2 Methods

2.2.1 Volunteers

Experimental procedures were in strict agreement with guidelines and regulations concerning human welfare and experimentation set forth by Turkish law, and approved by a Committee on Ethics of Human Experimentation at Istanbul University, Istanbul School of Medicine, Istanbul. Five healthy female volunteers ((mean $\pm$ SD):

age = 25.6 ± 1.8 years, height = 160.4 ± 5.5 cm, body mass = 51.4 ± 7.8 kg) participated (Table 2.1). After a full explanation of the purpose and methodology, volunteers provided informed consent.

Table 2.1
Anthropometric data.

Volunteer	Age	Height (cm)	Mass (kg)	Upper leg length (cm)	Lower leg length (cm)
A	27	154	45	49	36.0
B	24	163	51	50.5	36.5
C	24	155	43	45.5	38.0
D	28	165	56	51.0	36.0
E	25	165	62	46.5	40.0

2.2.2 Experimental protocol

Each volunteer was positioned prone on MRI patient table. Volunteer's left leg was brought to a reference position:

1. The ankle was fixed at 90° by using a custom made MRI compatible device (Figure 2.1a). A piece of Velcro under the heel and straps over the ankle allowed joint position fixation.

2. Using scanner's positioning laser, tip of the device and three locations in the lower leg were marked to fix its orientation. Position of the spina-iliaca anterior–superior was marked on MRI table. To locate the knee joint, a piece of Velcro was attached over the patella and also on MRI table.

The knee angle measured using a universal goniometer [94] in the reference position (undeformed state) equaled 158 ± 5°. After moving the patient table into the bore, sets of 3D high resolution MR images were acquired in relaxed state. Subsequently, patient table was moved out. Standard KT (5 cm beige Kinesio Tex Gold

FingerPrint Tape, Kinesio Holding Company, Albuquerque, NM) was applied without removing the volunteer from MRI patient table. Placing one end at the dorsal surface of the metatarsus, tape was stretched proximally to the tuberosity of tibia with 50% tension (Figure 2.1b), and was adhered over the skin along m. tibialis anterior (TA) after the ankle was brought to plantar-flexion [85] (Figure 2.1c). This imposes a distally directed loading. Using the positioning laser, care was taken to maintain marker positions. In this deformed state, knee angle equaled $158 \pm 4°$. Maintained relaxed state of the volunteer for 30 min allowed KT effects to be stabilized. Then the patient table was moved into the bore automatically ensuring that it attained the identical position also during image acquisition in the deformed state.

2.2.3 Image acquisition

3D localizer imaging was performed to plan the subsequent imaging sequences. 3D turbo fast low-angle shot [Turbo FLASH] based (Table 2.2) coronal MR image sets were collected using 3 T MR scanner (Magnetom Trio; Siemens, Erlangen, Germany) with two 6-channel surface coils. Choices of high bandwidth and frequency encoding in proximo–distal direction [95] allowed minimizing potential chemical shift artifacts. Imaging time equaled 6 min and 6 s.

Table 2.2
Parameters used in FLASH sequence. Note that no fat suppression and a choice of high bandwidth (41 600 Hz) were used. Number of averages = 1.

TR (ms)	TE (ms)	TI (ms)	Flip angle (°)	Band-width (Hz/px)	Field of view (mm^2)	Slice thickness (mm)	Number of slices	Image matrix size (px^2)	Voxel size (mm^3)
1750	3.36	1100	12	130	320 x 320	1	144	320 x 320	1 x 1 x 1

2.2.4 Calculation of in vivo deformations

Starting from the proximal half of the imaged portion of the lower leg (corres-

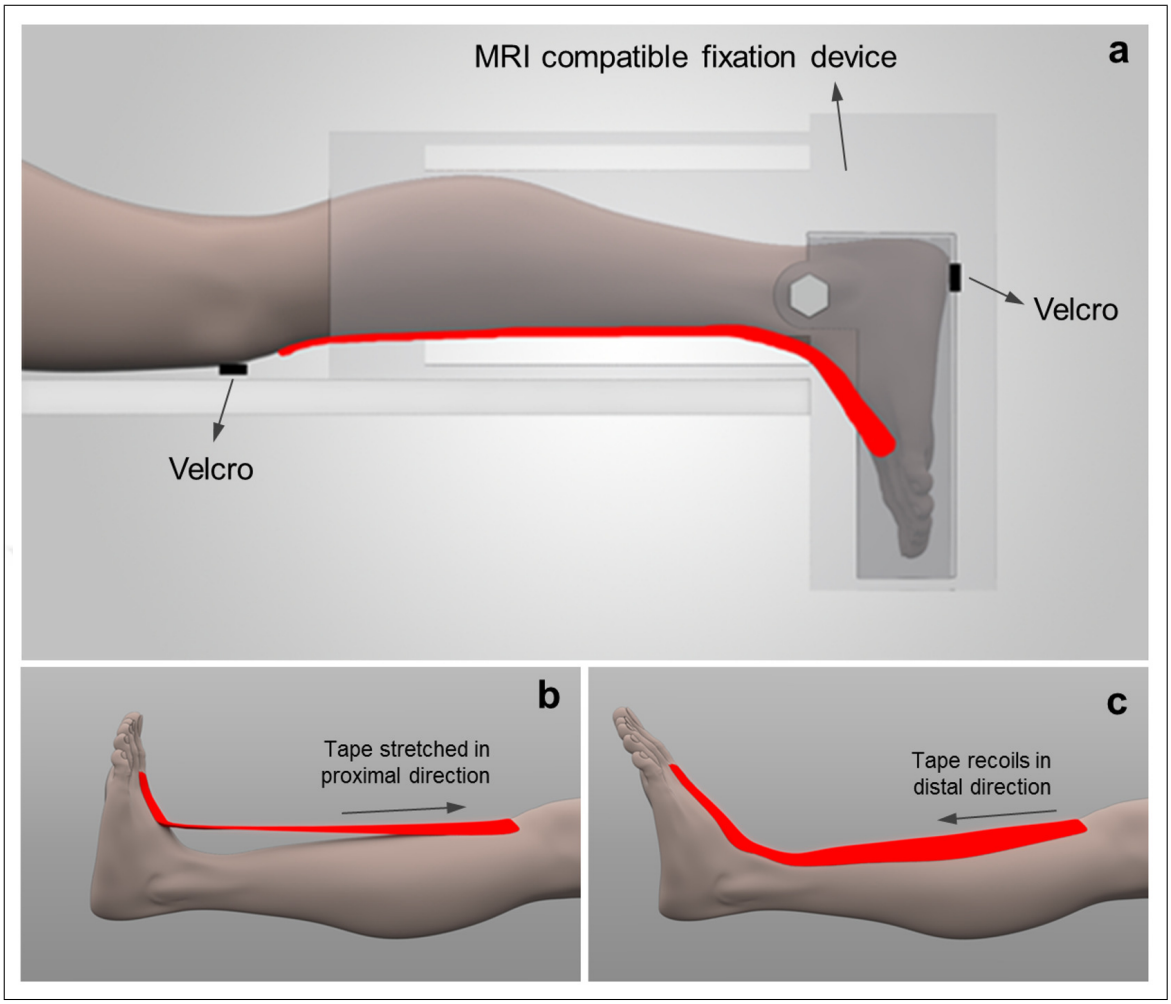

Figure 2.1 Illustrations of volunteer positioning in MR scanner and KT application. MR image sets were acquired before and after tape application for the undeformed and deformed states, respectively. (a) Volunteer positioning after tape application is illustrated. Experimental procedure includes several steps: (1) volunteer's left leg was brought to a reference position. Ankle angle was fixed at 90°by using an MRI compatible fixation device. A piece of Velcro under the heel, and strapping over the ankle allows fixation of the ankle angle. To locate the knee joint, a piece of Velcro was attached to the patella. Position of the knee (patella) was marked on MRI table and a corresponding piece of Velcro was placed. Additionally, position of spina-iliaca anterior–superior was marked on MRI table (not shown in the figure). (2) The patient table (a motorized and computer-controlled slide) was moved into MRI bore. Using positioning laser of MRI scanner, care was taken to maintain the positions of the markers on the lower leg and on the fixation device with respect to corresponding markers on the patient table. (3) After MR image sets of undeformed state were acquired, patient table was moved out of MRI bore for tape application. (b) With the ankle in dorsi-flexed position, one end of the tape was placed distally at the dorsal surface of the metatarsus and the other end was stretched to 50% tension proximally and placed on the tuberosity of tibia. (c) Ankle was then brought to plantar-flexion and tape was adhered over the skin along m. tibialis anterior. (4) After waiting for 30 min to allow tissue deformation take place, patient table was moved back into the bore automatically ensuring that it attains identical position as during previous image acquisition. Care was taken to maintain positions of the markers and MR image sets of the deformed state were acquired.

ponding to mid-TA belly), 64 consecutive cross-sectional slices were studied (Figure 2.2a). Within each slice, seven anatomical regions were distinguished manually by out-

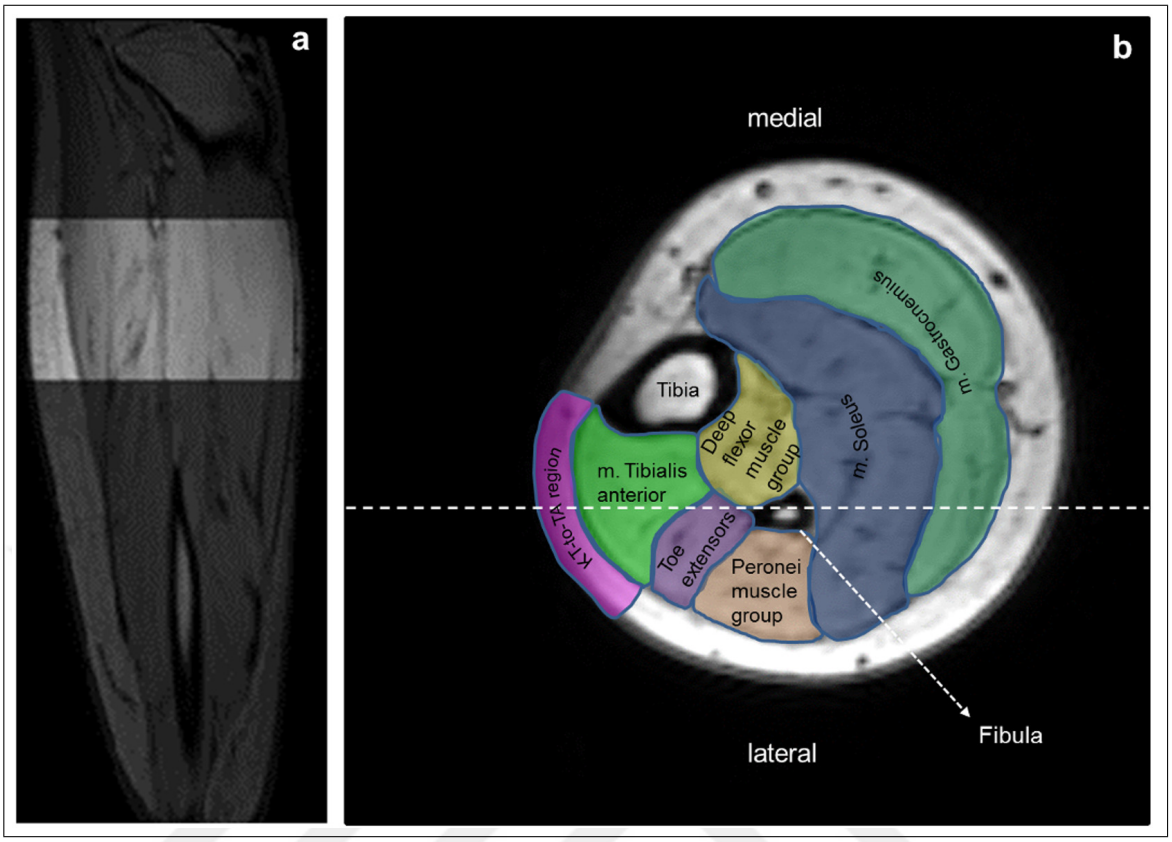

Figure 2.2 Anatomical regions studied. (a) A slice group consisting of 64 consecutive cross-sectional slices was selected manually for each volunteer: the most proximal slice location was at the proximal half of the length of the imaged portion of the lower leg (corresponding to mid-m. tibialis anterior belly). (b) Within each slice analyzed, seven anatomical regions were distinguished manually by outlining their boundaries to represent connective tissues including the skin and fasciae superficial to TA (KT-to-TA region), m. tibialis anterior (TA), toe extensors (m. extensor digitorum longus and m. extensor hallucis longus), peroneal muscles, deep flexor muscles, m. soleus and m. gastrocnemius. White dashed line corresponds to the location of sagittal slice in (a).

lining their boundaries (Figure 2.2b): connective tissues including the skin and fasciæ superficial to TA (referred to as KT-to-TA region) and TA (directly targeted tissues); toe extensors, peroneal muscles, deep flexor muscles, m. soleus and m. gastrocnemius (non-targeted tissues).

In vivo deformations caused by KT were calculated (Figure 2.3) by aligning MR images acquired in the deformed and undeformed states. Demons algorithm [47], i.e., a non-rigid and non-parametric image analysis technique was applied. Utilizing arrays of voxel intensities, this algorithm relies on differences between grayscale values of consecutive voxels within each image and corresponding voxels in deformed and

undeformed images. Image differences calculated iteratively are used to characterize displacement values for each voxel. During each iteration, updated displacement fields are smoothed by a Gaussian kernel for regularization of local displacements and global motion. Finally, after a successful alignment of images obtained by minimizing image differences, information on real deformation is available for each cubic shape comprised of four adjacent image voxels.

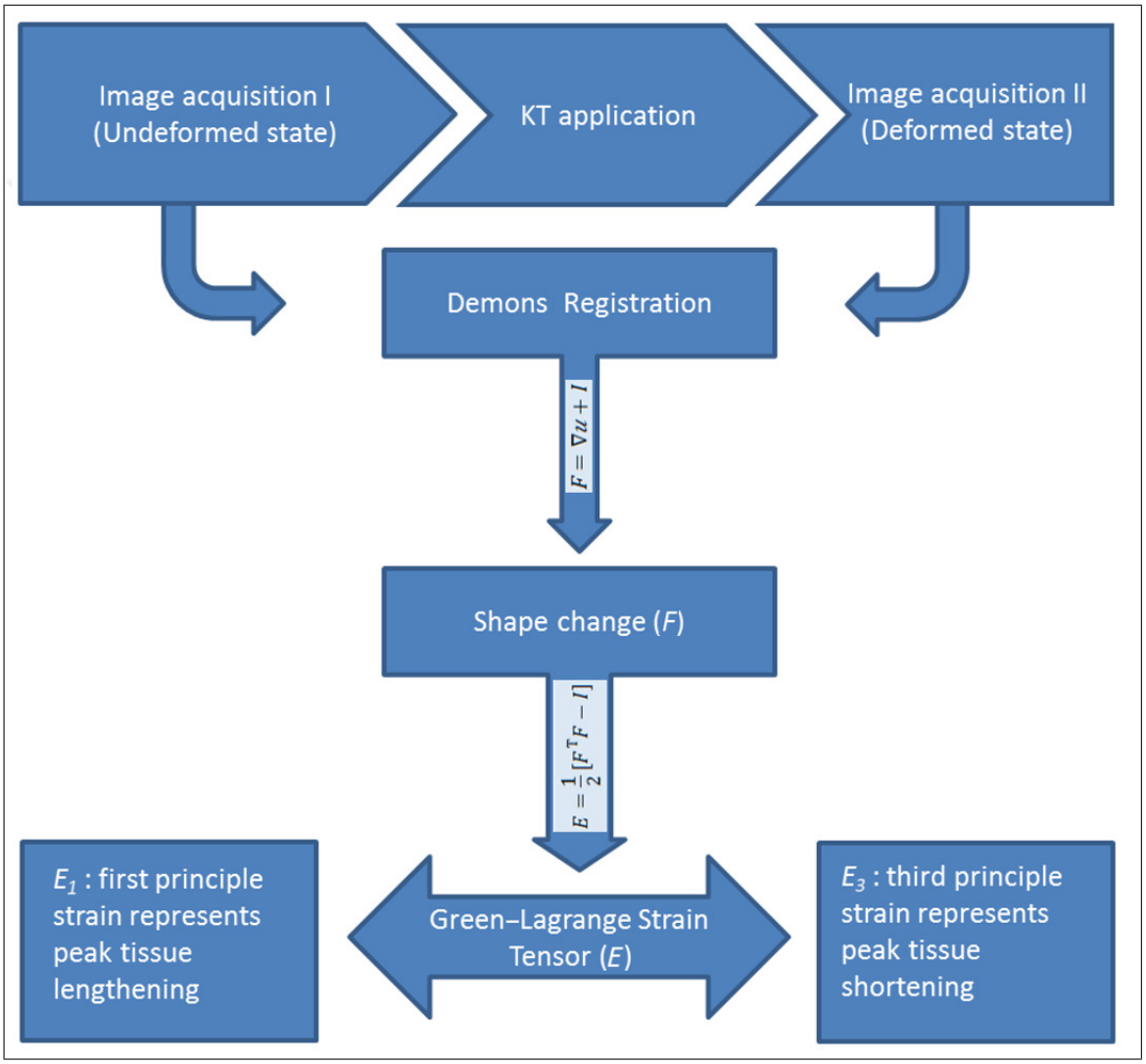

Figure 2.3 Flowchart for image acquisition and data processing steps. Undeformed and deformed image sets were registered using demons algorithm. Obtained deformation gradient matrix (F) was used to calculate Green–Lagrange strain tensor (E) for each voxel. Eigenvalue analyses yielded first (E_1) and third (E_3) principle strains, representing peak tissue lengthening and shortening, respectively.

Using displacement fields obtained, deformation gradient matrix F, characterizing voxel deformation, was calculated by using displacement gradient, ∇u, in material

coordinates:

$$F = \nabla u + I \tag{2.1}$$

Green–Lagrange strain tensor E was calculated for each voxel in order to assess deformations within the lower leg muscles present after KT application:

$$E = \frac{1}{2}\left[F^T F - I\right] \tag{2.2}$$

For each anatomical region separately eigenvalue analyses were done per voxel. First (E_1) and third (E_3) principal strains represent peak local tissue lengthening and shortening, respectively. The eigenvectors determine the direction of peak deformations.

2.2.5 Calculation of algorithm artifacts

The validity of demons algorithm has been well-tested and shown for several soft tissues including myocardium (e.g., [96, 97]). This algorithm's success in quantifying skeletal muscle tissue deformations was shown with vigorous testing [93]. Presently, image sets of the undeformed state were transformed by a "synthetic rigid body" motion imposed on the data: 10° rotation within the cross-sectional plane (representing endorotation of the knee during flexion [98], 3° rotations in the coronal and sagittal planes, and 4 mm translation axially.

Subsequently, the undeformed state and the transformed image sets were compared. Theoretically, imposed rigid body motion should cause no strains. Therefore, any strains calculated represent algorithm artifacts.

2.2.6 Calculation of volunteer repositioning artifacts

In order to characterize artifacts due to volunteer repositioning *per se*, identical experimental procedures and data analyses described above were repeated in a separate session, this time without KT application.

2.2.7 Statistics

Principal strain distributions by definition deviate from normal distributions. Therefore, non-parametric Wilcoxon rank-sum tests were performed for differences between

1. artifacts and in vivo deformations due to KT application
2. and deformations in directly targeted and non-targeted tissues.

Non-parametric Kruskal–Wallis tests with Dunn's post-hoc test were performed for inter-subject variability. The level of significance was chosen at $p > 0.05$.

2.3 Results

After KT application, mean peak tissue strains in directly targeted tissues and non-targeted tissues were significantly higher than algorithm and volunteer repositioning artifacts (Table 2.3). For a majority of the comparisons, volunteer repositioning artifacts were significantly higher than algorithm artifacts.

Figure 2.4 shows pooled local tissue deformations data across all volunteers. For KT-to-TA and TA regions respectively, maximal local lengthening and shortening equals 51.5% and 27.5%, and 41.4% and 29.6% (Figure 2.4); mean lengthening and shortening equals 10.9% and 10.2%, and 10.2% and 10.1% (Table 2.3). Maximal

strain values of the non-targeted tissues are sizable (Figure 2.4). However, overall, mean local lengthening and shortening (5.7% and 5.9%) are significantly smaller than corresponding values of KT-to-TA and TA regions each (Table 2.3).

Table 2.3
Algorithm (top) and subject repositioning (middle) artifacts compared to in vivo strains due to KT application (bottom) for KT-to-TA region (left), TA (middle) and non-targeted tissues (right). * denotes significant differences ($p < 0.05$) with algorithm artifacts within a given region. † denotes significant differences ($p < 0.05$) with subject-repositioning artifacts within a given region. ‡ denotes significant differences ($p < 0.05$) between targeted and non-targeted tissues within a given region.

Mean ± SD	KT-to-TA region	TA	Non-targeted tissues
Algorithm artifacts (synthetic rigid body motion) (n=5) No KT applied			
Algorithm artifact (lengthening)	1.5% ± 1.0%	1.5% ± 1.3%	1.2% ± 1.1%
Algorithm artifact (shortening)	-1.6% ± 1.2%	-1.6% ± 1.1%	-1.3% ± 1.1%
Volunteer repositioning artifacts (n=5) No KT applied			
Volunteer repositioning artifact (lengthening)	3.3% ± 2.4%*	4.5% ± 3.7%*	2.9% ± 2.6%*
Volunteer repositioning artifact (shortening)	-4.7% ± 3.5%	-4.8% ± 3.7%*	-3.3% ± 2.4%*
Local tissue strains (n=5) due to KT application With KT applied			
Strain due to KT (lengthening)	10.9% ± 7.6%*, †, ‡	10.2% ± 7.7%*, †, ‡	5.7% ± 4.1%*, †
Strain due to KT (shortening)	-10.2% ± 6.0%*, †, ‡	-10.1% ± 5.9%*, †, ‡	-5.9% ± 3.8%*, †

Figure 2.5 shows distributions of local deformations for volunteer A. This presentation visually reveals that bigger amplitude strains occur in directly targeted tissues. Key tissue deformations (Figure 2.5d) are described below. See Appendix A for such presentations for other volunteers and Figure 2.6 for a comparison across volunteers.

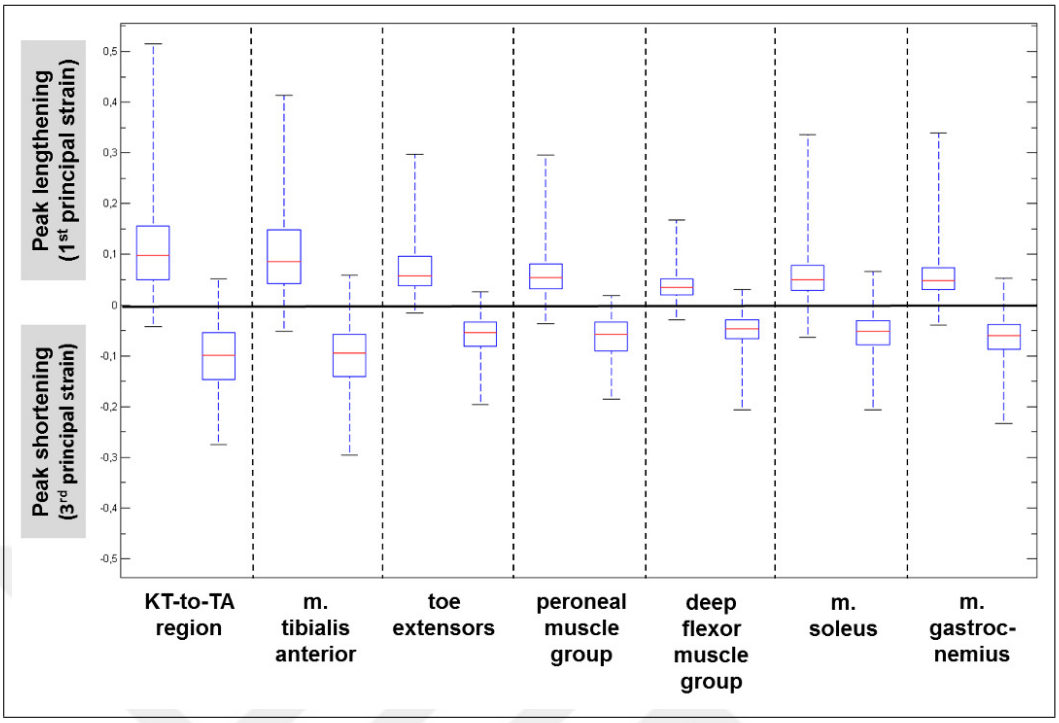

Figure 2.4 Effects of KT application in terms of local tissue deformations. Data were represented per anatomical region of interest (muscle, muscle group or non-muscular tissue) and analyzed across all volunteers. Local tissue lengthening and shortening effects (first and third principal strain). Box and whisker plots: The horizontal line inside each box represents the median strain value; the upper and lower edges of each box itself represent upper and lower quartiles respectively (i.e., the 75th and 25th percentiles), and lines extending from each end of the box (whiskers) indicate the maximal values of the principal strains plotted.

Directly targeted tissues: Superficially, along the skin, both lengthening and shortening occurs in anterior–posterior directions, causing parts of the skin to be lifted or pressed. Deeper, parts of KT-to-TA region undergo shortening proximally or lengthening distally. Lateral half of TA shows lengthening posterior–laterally, whereas medial half shows shortening proximally. Other volunteers also show consistent deformations, in varying amplitudes (Figure 2.6). However, volunteer D (Figure A.3) is an exception with lateral and medial halves of TA showing shortening in anterior and anterior–proximal directions, respectively.

The non-targeted tissues: Overall, deformations in variable magnitudes and directions are found for volunteer A (Figure 2.5) and for the remainder volunteers. However, inter-subject variability in strain magnitudes and directions is notable. For volunteers D and E, deformation in the non-targeted tissues is comparable to that of

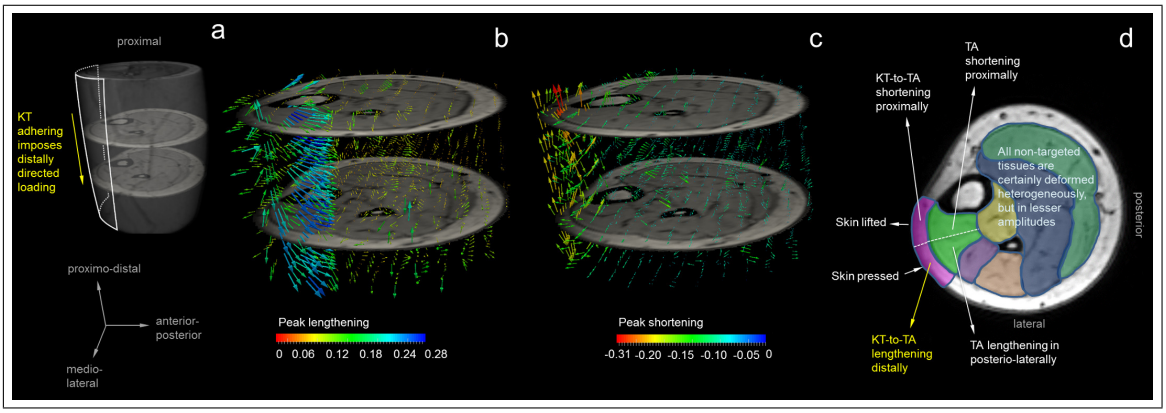

Figure 2.5 Distributions of local tissue deformations due to KT application per volunteer. The deformation fields belong to Volunteer A. The reader is referred to Appendix A material for other volunteers. Deformation fields are visualized using glyphs. Each glyph represents deformation of a voxel. However, for clarity of presentation, a consistent glyph masking was employed. The direction of each glyph is determined by the corresponding eigenvector. The length of each glyph is proportional to the magnitude of local tissue lengthening or shortening. (a) Representation of KT applied zone within imaged volume. Two anatomical image slices are shown for reference. These slices, also shown in parts (b) and (c), are proximally and distally 20 slices away from the centrally located slide within the analyzed volume. Superior–inferior (representing the tape direction), anterior–posterior and medio–lateral directions are indicated. Deformations fields are shown distinguishing (b) local tissue lengthening and (c) local tissue shortening (first and third principal strains, respectively). (d) The anatomical regions distinguished. Note that KT-to-TA and TA regions comprise directly targeted tissues whereas the remainder regions together are referred to as non-targeted tissues. General deformation characteristics of these tissue regions are summarized.

directly targeted tissues (Figure 2.6).

In sum, only one part of deeper KT-to-TA region shows local deformations in agreement with tape adhering direction whereas, including superficially the skin, the rest of KT-to-TA and TA regions shows deformations in other directions. Moreover, although KT causes more pronounced deformations in the directly targeted tissues, non-targeted tissues also show sizable heterogeneous deformations. These findings confirm our hypotheses. Inter-subject variability of KT effects is notable.

2.4 Discussion

Demons algorithm has been utilized for calculating deformations in various tissues including pelvic floor [99], lung [100], myocardium [97] and finger flexor muscles

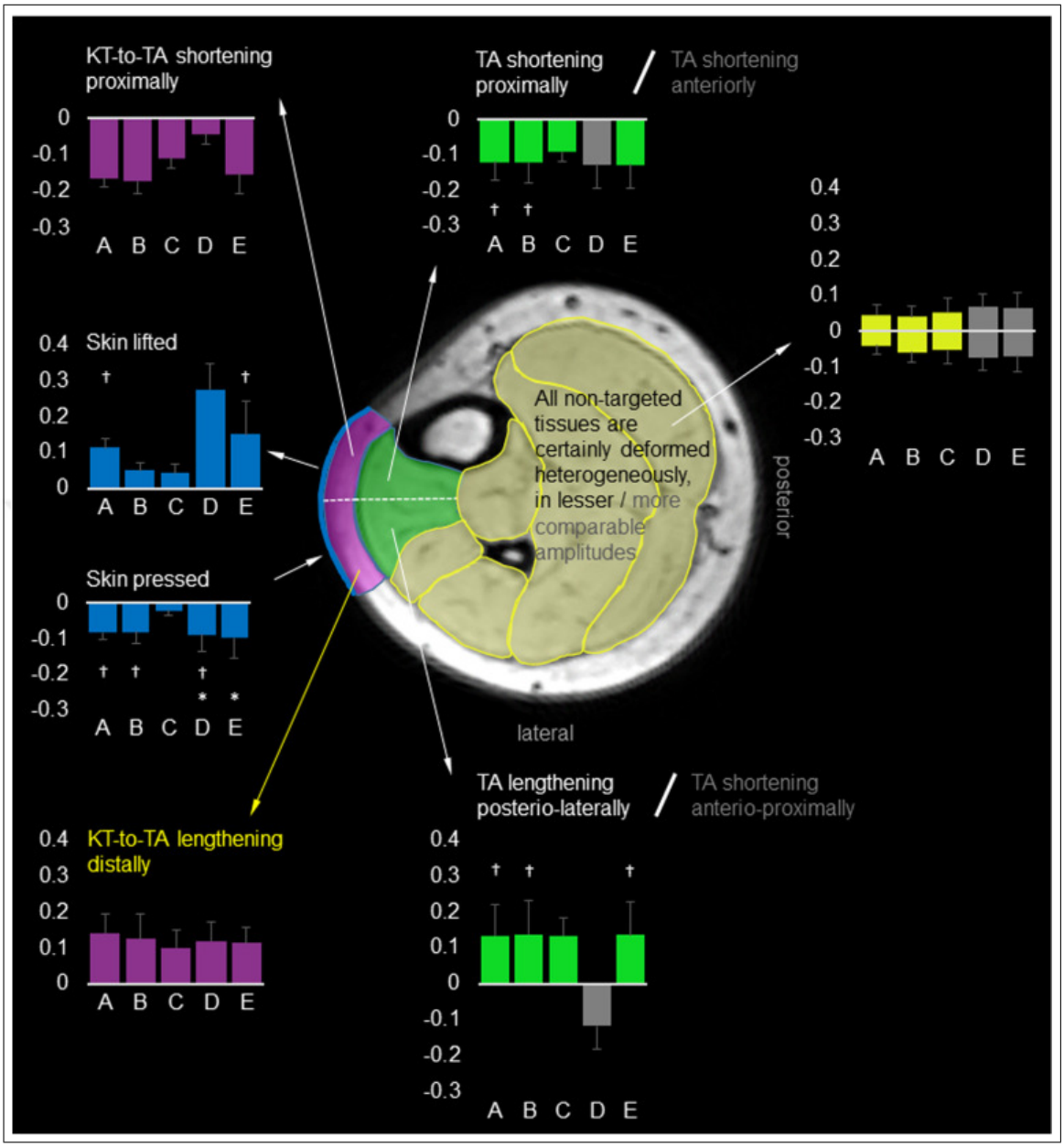

Figure 2.6 Comparison of key tissue deformations across volunteers for inter-subject variability. Key tissue deformations are distinguished by using eigenvectors calculated per voxel: e.g., proximally directed key tissue deformation is classified for magnitude 40.5 of voxel eigenvector component in the proximal direction. For directly targeted tissues, voxels belonging to medial or lateral halves of the skin; remainder of KT-to-TA region; and TA region were distinguished manually. Consequently, a total of 10 000 to 85 000 voxels were included in assessments for each of these regions. For the non-targeted tissues, deformation is quite heterogeneous with no key tissue deformation pattern easily recognizable. Therefore, voxels are included without such classification for a general comparison across volunteers. Bar plots show mean and SD of key tissue deformations per region and per each volunteer. Consistent key tissue deformations across volunteers can be compared for varying amplitudes for each region (all comparisons except those indicated by * or † are significantly different). Deviations from that are indicated by gray bars and font.

[101]. In those studies, good agreements were shown among strains calculated using demons algorithm and those determined by other registration methodologies and imaging modalities. A commonly used reliable method to test algorithm success is to use synthetic image sets with known deformations imposed on the test image itself [102, 103]. In addition, physical phantoms are used for a more direct testing [99, 104]. This technique reliability of which was well established previously was employed recently to assess the deformation of human lower leg musculature [46, 93]. Knee angle changes were imposed passively to alter the length of m. gastrocnemius, whereas the ankle was fixed to restrain distally the lengths of all lower leg muscles. Yaman et al. [93] devised a synthetic known image deformation test involving very similar displacements to those occurring in the experiments, which were imposed exclusively on m. gastrocnemius, forcing the remaining tissue volume to be absolutely undeformed. Such challenging registration yielded no false deformations to be calculated in that volume and strains of similar order of magnitude as those imposed by image deformation were calculated for m. gastrocnemius. This confirms success of demons algorithm for muscle tissue analyses, but also shows its limitations:

1. Strains were somewhat underestimated suggesting that they are conservative estimators of actual local deformations.

2. Sharp discontinuities in deformation yield errors for narrow regions separating the deformed and undeformed volumes indicating that deformations in boundaries between anatomical units need caution. However, strict discontinuities as such are unrealistic during actual joint movement and also in the present test protocol, which does not involve joint movement.

Huijing et al. [46] and Yaman et al. [93] conducted also a rigid body motion test by imposing synthetic motion representing a much larger scale motion than possible motion of subjects during imaging. As this should theoretically cause zero strain it is a good test of the algorithm, which yielded very small strains, calculated in those studies and presently. However, earlier experiments did not require the subjects to be removed from the MRI table. Therefore, in the present study, an additional testing of

actual subject repositioning was appropriate and yielded larger deformations than those resulting from the synthetic testing. This suggests that certain changes in the joint configurations of the subjects prior to deformed state imaging are likely. Nevertheless, KT induced effects do dominate such artifacts. Quantifying local tissue deformations due to KT allows gaining a great insight for an objective understanding of the effects of this treatment. Further technical developments marginalizing any artifacts of the employed advanced MRI analyses and tailoring them also to other protocols of KT applications can yield highly relevant new studies.

Notably, most local deformations within the directly targeted tissues are not along the tape direction. Deformation in orthogonal directions can be explained by recoiling of the stretched tape causing the underlying skin to crimp. This involves the "lifting" effect as described by Kase et al. [85] at parts but, also the opposite elsewhere causing local lengthening and shortening in anterior–posterior and medio-lateral directions. However, the remaining mismatch among the loading vs. deformation direction can only be explained by transmission of the imposed loads differentially within the tissues. Within the KT-to-TA region, collagen bundles have increasingly random orientations from superficial (epidermis) to deeper (dermis) layers of the skin [105]. Superficial fascia is continuous with the dermis, and consists of non-dense (areolar) and dense connective tissue, both containing irregularly arranged collagen fibers [106]. Skin ligaments connect the base of the dermis to the deep fascia [107]. This is continuous with epimysium of the muscle below and its ECM is comprised of irregularly arranged collagen fibers [106]. Collagen is the basic load-bearing element in connective tissues [108] which are pathways for MFT [23, 31, 88, 109]. Myofascial loads distributed within these structures can affect mechanics of activated muscle substantially due to their effects locally on sarcomeres [24, 32, 65]. However, these loads affect local muscle tissue deformations also in passive conditions among synergistic [46] and antagonistic muscles of the lower human leg, in vivo [93]. Regarding the present findings we suggest the following explanation. The tape may deform the superficial skin predominantly in the direction it is adhered. However, owing to the irregular arrangement of collagen fibers deeper within the skin and within the intramuscular connective tissues, the loads are directed diversely such that most of the deformation occurs in arbitrary directions.

Local deformations observed within the non-targeted tissues indicate that the mechanical loading imposed externally by KT application causes local distributed myofascial loads within the entire lower leg. Previous studies reported for the rat muscles in situ [91, 92] and for human muscles in vivo [46, 93] that inter-muscular mechanical interaction ascribed to muscle relative position changes causes altered force or local deformation. The results show that KT can cause such mechanical interaction affecting tissues far away from those directly targeted. However, tissue lengthening and shortening appear less pronounced suggesting that the proximity to tape affects magnitude of myofascial loads.

Ascribed to an expected increase of skin tension, KT application has been considered to alter skin mechanoreceptors' perception of joint position evoking stimulus perceived as reaching the end of normal joint position, before such position is attained [85]. A plausible mechanical consequence of such sensory illusion is repositioning of the joint in order to normalize perceived skin tension causing an assistance of flexion action. Conceivably, distal lengthening of part of KT-to-TA region in agreement with KT adhering direction may provide such assistance. However, the present findings indicate varying directions and amplitudes of skin deformation including not only elevated tension but also the opposite. Therefore, KT effects on proprioception appear to rely on a much more complex mechanism than a uniform tension effect on the skin. Yet, free nerve endings in the superficial epidermis and dermis [110] are sensitive to stretch irrespective of loading direction [111, 112] and play a role in pain inhibition [113]. Therefore, deformation patterns shown in KT-to-TA region ally with pain alleviation. Lymphatic drainage is an expected KT effect [114] ascribed to lifting [85]. However, presence of not only lifted but also pressed skin parts indicate a more complex mechanism, relying plausibly on a pressure gradient in the tissue.

Muscle is the motor for movement hence anticipated improved joint function effects should relate to muscle function. Sizable mechanical effects of KT for the TA and other muscles are shown. Local deformations imply effects on muscle spindles, considered sensitive primarily to stretch [115]. However, this effect is not necessarily in agreement with tape adhering direction. The deformation patterns within the tar-

geted TA are not homogeneous. This does not support the implicit assumption that KT causes uniform spindle stretch or unloading characterized by the way it is applied. Therefore, an expectation of facilitation or inhibition effects directly in concert with the external tape application protocol may be a simplistic one. Yet, muscle spindles respond to transverse loads and pressure [116]. They are considered to act also as "misalignment sensors" [87] or local sensors of heterogeneous tissue strain [32]. These issues, which need to be confirmed, suggest locally increased and decreased mechanoreceptor stimuli occurring simultaneously at different parts of the muscle. Therefore, a preferred outcome at the joint should be a net effect of such variable stimuli instead of a uniform increase or decrease. Using EMG, Alexander et al. [80, 81] showed an inhibitory effect of taping, which was applied to achieve a facilitation effect on trapezius and gastrocnemius muscles. Based on our data, their findings may either reflect a net effect of inhibitory nature or a local effect predominantly inhibitory, whereas other locations not measured could show the opposite. KT effects on antagonistic muscles are either not anticipated or are considered as secondary to effects on target tissue's sensory apparatus [86]. The results show local tissue deformations confirming effects of KT on non-targeted tissues and sustain the role of a neuro-mechanical coupling within the entire limb. These issues may have important implications for improving joint function using KT.

Issues not considered presently should be acknowledged. First, other taping applications may cause different effects. Increasing the tape tension or providing an inward pressure to the tissues can affect deeper layers of fasciæ [85]. This could cause higher amplitude deformations to take place in a wider zone potentially including also some of the non-targeted tissues. However, uniform effects consistently in agreement with tape adhering direction are still not conceivable. Second, the present testing was done in passive conditions, whereas typical use of KT involves muscle activation and joint motion during daily or sportive activities. Muscle activation leads to increased stiffness in muscle tissue [117]. This may favor spread of externally imposed loads and elevate the effects shown presently. However, muscle activation will cause shortening of the target muscle and as a consequence of joint motion, antagonistic muscles will also change length. This is likely to alter KT effects on proprioception. Third, athletes with

musculo-skeletal and connective tissue pathologies and patients with e.g., spasticity could differ from our study group. Increased connective tissue stiffness and muscle tone of pathological tissues may result in more pronounced load transmission compared to that presently shown and local variations in tissue deformations are plausible. It is important that future studies also test experimental conditions involving such issues not considered here.

In conclusion, MRI analyses allow for an objective assessment of local tissue deformations caused by KT application. The findings show that local deformations occurring acutely within the directly targeted tissues include local lengthening and shortening within both connective tissues including the skin and fasciæ superficial to the targeted m. tibialis anterior and within this muscle. These deformations are heterogeneous in magnitude and direction. Notably, only a small portion of the targeted tissue volume shows deformations in agreement with tape adhering direction whereas, most deformation occurs in other directions. Moreover, non-targeted muscles are subject to such deformations, but in smaller amplitudes.

3. MAGNETIC RESONANCE AND DIFFUSION TENSOR IMAGE ANALYSES AND ASSESSMENT OF LOCAL ALONG-FIBER MUSCLE STRAINS RESULTING FROM JOINT ANGLE MANIPULATION IN VIVO

3.1 Introduction

Arranged in series within muscle fibers, sarcomere is the basic functional element of skeletal muscle. Force production capacity of sarcomere depends on its length. Therefore, quantification of length changes along fibers of human muscles, in vivo bears great importance for characterizing muscle's function.

Magnetic resonance imaging (MRI) analyses are highly suitable for quantifying local tissue deformations in human muscles. Demons registration [46, 93], phase-contrast [41, 43, 118], displacement encoding with stimulated echoes [45] and spatial-tagging [119] were used previously. However, these techniques alone are insufficient for determining deformation along muscle fibers.

Diffusion tensor imaging (DTI) is an MRI methodology that detects diffusivity of water within biological tissues by applying diffusion sensitizing gradients in multiple directions. Diffusion of free water molecules in tissue is limited by tissue structures such as cell membranes [48]. Therefore, tensors storing data characterizing diffusion of water molecules along each gradient direction identify tissue architecture. Animal [49] and cadaver [50] studies have shown that the first eigenvector of the diffusion tensor corresponds to the direction of muscle fibers. Damon et al. [56] presented feasibility and validation of tractography for determining pennation angles using DTI. Repeatability of structural muscle measures such as pennation angle and fiber length has been demonstrated for humans in vivo [57]. Hence, DTI tractography allows for visualizing orientation of muscle fibers.

Using MRI based deformation analyses and DTI based tractography combined, we aimed to assess muscle fiber direction local tissue deformations within the human medial gastrocnemius (GM) muscle as caused by knee angle changes.

3.2 Materials and Methods

Experimental procedures were in strict agreement with guidelines and regulations concerning human welfare and experimentation set forth by Turkish law, and approved by a Committee on Ethics of Human Experimentation at Istanbul University, Istanbul School of Medicine, Istanbul.

3.2.1 Volunteers

Five healthy female volunteers ((mean $\pm$ SD) age $= 27 \pm 1$ years, height $= 159 \pm 4$ cm, body mass $= 50 \pm 4$ kg) participated (Table 3.1). After a full explanation of purpose and methodology, volunteers provided informed consent.

3.2.2 Experimental protocol

Volunteers were positioned prone on MRI patient table. Volunteer's left leg was brought to a reference position: The ankle was fixed at 90° by using a custom made MRI compatible device. A piece of Velcro under the heel and straps over the ankle allowed joint position fixation. To locate the knee joint, a piece of Velcro was attached over the patella and also on MRI table. The knee was brought to flexion by elevating the torso with support such that the trunk of the volunteer is brought as close as possible to the MRI bore wall in order to attain the maximal flexed knee position (Figure 3.1A). The knee angle measured using a universal goniometer [94] in this undeformed state equaled $140.8 \pm 3.0°$. After moving the patient table into MRI bore, sets of 3D high-resolution MR and DT images were acquired at relaxed state.

Table 3.1
Anthropometric data.

Volunteer	Age	Height (cm)	Mass (kg)	Upper leg length (cm)	Lower leg length (cm)
A	25	160	47	42.0	37.0
B	27	154	45	49.0	36.0
C	29	160	52	43.0	37.0
D	28	165	56	51.0	36.0
E	27	158	52	44.0	38.0

3.2.3 MR and DT image acquisition

3D localizer imaging was performed to plan subsequent imaging sequences. 3D turbo fast low-angle shot [Turbo FLASH] based (see Table C.1 for MR imaging parameters) coronal MR image sets were collected using 3 T MR scanner (Magnetom Trio; Siemens, Erlangen, Germany) with two 6-channel surface coils. Choices of high bandwidth and frequency encoding in proximo–distal direction [95] allowed minimizing potential chemical shift artifacts.

2D single shot echo planar imaging (ss-EPI) based axial DT image sets were collected with fat saturation and posterior–anterior direction frequency encoding to minimize potential chemical shift artifacts in the region of interest. Non-weighted b0 images and 12 diffusion-weighted gradient images with unique directions were acquired for eight signal averages (see Table C.1 for DT imaging parameters).

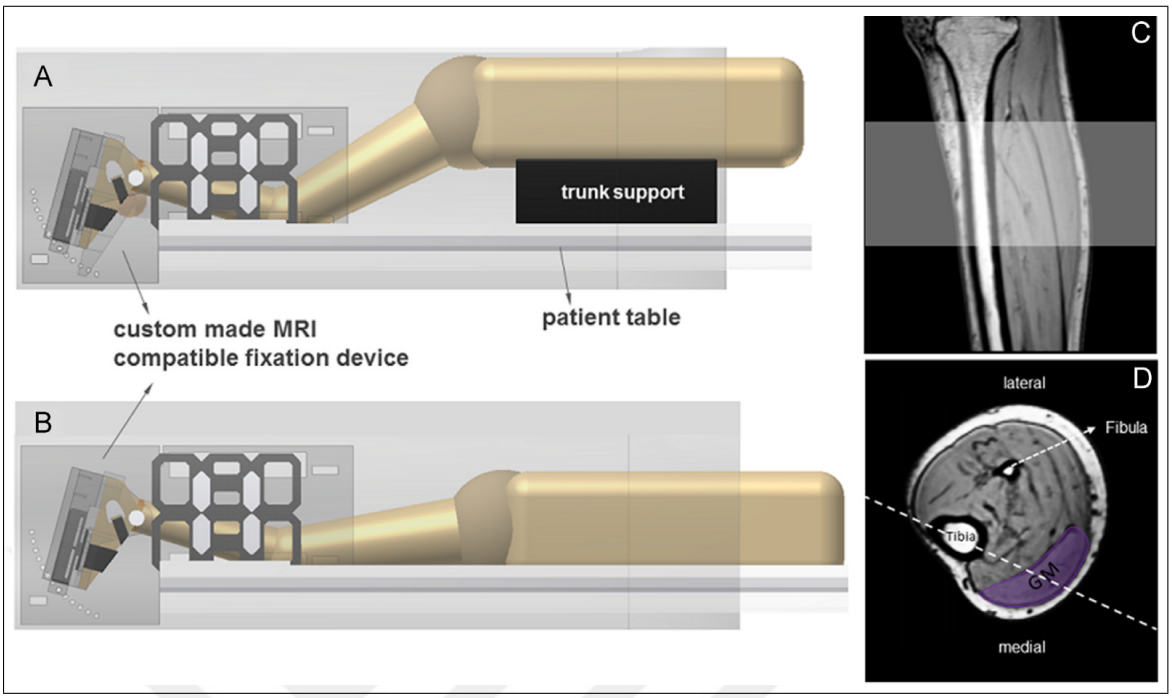

Figure 3.1 Illustrations of volunteer positioning in MR scanner and the anatomical region studied. (a) Undeformed state. Body is prone on the patient table that can be moved in and out of the bore of MRI machine. A custom made MRI compatible fixation device was used to fix the ankle angle at 90°. A piece of Velcro under the heel and strapping over the ankle allows fixation of the ankle angle. To locate the knee joint, a piece of Velcro was attached to the patella and a corresponding piece of Velcro was placed on MRI table. Trunk of the volunteer is supported and brought as close as possible to the bore of MRI in order to impose a flexed knee position. (b) Deformed state. Support under trunk of the volunteer is removed. This creates movement in hip as well as knee joints, but preserves the lower leg position. Ankle angle is unchanged. (c) A slice group consisting of 112 consecutive cross-sectional slices coinciding with the diffusion weighted image volume (corresponding to mid-m. gastrocnemius belly) was selected manually for each volunteer. (d) Within each slice analyzed, anatomical region enveloping GM was distinguished manually by outlining its boundaries. White dashed line corresponds to the location of sagittal slice in (c).

3.3 Calculation

3.3.1 Calculation of deformations

MR images were rigidly aligned with DT images. Starting from the proximal half of the imaged portion of the lower leg (corresponding to mid-GM belly), in each of 112 consecutive cross-sectional slices studied, GM region was distinguished manually (Figure 3.1c and 3.1d).

Deformations caused by knee extension were calculated by aligning MR images

Table 3.2
MR and DT imaging parameters. [a]Resampled 128 x 128.

	MR Imaging Parameters	DT Imaging Parameters
Sequence	Turbo FLASH	ss-EPI
Slice orientation	Coronal	Axial
Repetition time (TR) (ms)	1750	4900
Echo time (TE (ms)	3.36	61
FOV (mm^2)	320 x 320	180 x 180
Matrix (px^2	320 x 320	64 x 64[a]
Pixel size (mm^2)	1.0 x 1.0	1.4 x 1.4
Slice thickness (mm)	1.0	2.8
Flip angle (°)	12	90
Bandwidth (Hz/px)	130	2003
b-value (s/mm^2)	N/A	450
Number of diffusion directions	N/A	12
Inversion time (TI) (ms)	1100	N/A
Acquisition time (min:s)	05:41	07:48

acquired in deformed and undeformed states. Demons algorithm [47], i.e., a non-rigid and non-parametric image analysis technique was applied. Utilizing arrays of voxel intensities, this algorithm relies on differences between grayscale values of consecutive voxels within each image and corresponding voxels in deformed and undeformed images. Image differences calculated iteratively are used to characterize displacement values for each voxel. During each iteration, updated displacement fields are smoothed by a Gaussian kernel for regularization of local displacements and global motion. Finally, after obtaining successful alignment of images by minimizing image differences, information on real deformation is available for each cubic shape comprised of four adjacent image voxels.

3.3.2 Determination of muscle fiber directions

Rician noise was eliminated [120] from raw diffusion weighted images (DWI). Subsequently, diffusion tensor of each voxel was calculated. To determine GM muscle fiber tracts, streamline tractography with 4th order Runge–Kutta numerical integration was performed on in-house software built on VAVframe framework[1] . Tract seed points were generated from voxels showing a minimum directionality of diffusion ($FA \geq 0.1$) [60]. The seed points were bi-directionally tracked with 0.7 mm integration steps (half of the smallest voxel dimension [121]). Each integration point forms a tract node.

Tracking algorithms typically make use of the known muscle geometry including boundary [61, 122] and tract length [57] to filter out possible irrelevant tracts. Based on a review by Chow et al. [123] reporting human GM fiber lengths, the criterion we implemented rejected tracts shorter than 30 mm, and longer than 50 mm. In addition, tracking was terminated if at least one of the following conditions was met:

1. Current tract node's $FA < 0.5$ and
2. tract curvature $> 5^\circ$ per step [60].

Two polygonal regions of interests, marked manually on deformed state b0 images, were used to constrain the tracts to be in GM. Tracts passing through both were accepted for further processing.

Fiber tract pennation angles (θ) were calculated based on Lansdown et al. [61]: deep GM aponeurosis was marked on the anatomic images, reconstructed in 3D and smoothed. Subsequently, unit normal vectors ($\hat{n}$) were calculated for each node of the aponeurosis model. For each tract, $\hat{r}$ is defined as the vector between the first node of the tract on the aponeurosis and the subsequent nodes along the tract. For each node,

[1] VAVframe if a registered C++ framework incorporating multiple open libraries, as well as original code, developed at Boğaziçi University, EE Dept. VAVlab, Istanbul, Turkey

pennation angle is calculated as $\theta = \sin^{-1}(\hat{n} \cdot \hat{r})$ and their mean along each tract is considered as its pennation angle.

3.3.3 Calculation of strains

Displacement fields in the global coordinates were mapped on deformed state b0 images and were linearly interpolated onto the nodes of the fiber tracts based on the weighted means of the grid neighbors of a given voxel in the displacement field.

Using the displacement fields obtained, deformation gradient matrix F, characterizing deformation at each fiber tract node, was calculated by using displacement gradient (∇u) in material coordinates:

$$F = \nabla u + I \tag{3.1}$$

Subsequently, the right Cauchy–Green strain tensor C

$$C = F^T F \tag{3.2}$$

and Green–Lagrange strain tensor E was calculated for each node in order to assess deformations within GM after knee extension

$$E = \frac{1}{2}[F^T F - I] \tag{3.3}$$

For each node the following were calculated:

1. Strain tensor was rotated to align with nodal unit tangent vector of the tract, M, yielding local fiber direction strain values.

2. In order to assess shearing between fascicles, along-fiber shear strain was determined based on [124, 125]. Strain invariants

$$I_4 = J^{2/3}\,\lambda_M^2 \tag{3.4}$$

$$I_5 = J^{4/3}\,\lambda_M^4\,(\,1+\psi^2\,) \tag{3.5}$$

were calculated, where $J = \sqrt{(\det C)}$, $\lambda_M = J^{-1/3}\sqrt{(M \cdot CM)}$, $\psi = \sqrt{(\frac{J^{-1/3}(M \cdot C^2 M)}{(M \cdot CM)^2} - 1)}$, and used to calculate along-fiber shear strain

$$B_1 = \sqrt{\frac{I_5}{I_4^2} - 1} \tag{3.6}$$

Nodal coordinates with corresponding fiber direction and along-fiber shear strain values were transferred to Slicer 4 (http://www.slicer.org) for visualization [126] of local muscle tissue deformations along GM tracts per volunteer in order to interrogate their homogeneity. A serial distribution of fiber direction strain hence, inhomogeneity of those values along GM tracts was considered as an indicator of altered force production potential of sarcomeres located at different parts of the tract. In addition, mean values of nodal fiber direction strains of each tract were calculated and visualized per volunteer. A parallel distribution of fiber direction strain hence, inhomogeneity of those values across different GM tracts was considered as an indicator of altered capacity of different tracts to the excursion of the muscle. Therefore, serial and parallel distributions were considered as metrics of high functional significance.

3. Determinant of F was used to assess volume change dV/dV_0.

For voxels in the deep GM aponeurosis, eigenvalue analyses were done to obtain peak local lengthening (E_1) and shortening (E_3). The eigenvectors determine the direction of peak strains. The peak local deep GM aponeurosis strains in the proximo–distal direction, aligned with the Achilles tendon, were distinguished.

3.3.4 Testing of MRI noise artifacts and repeatability

In order to quantify possible artifacts due to noise within MRI scanner, two separate MR image sets of a volunteer were acquired in subsequent imaging performed in constant position. This assessment showed that the noise artifacts are small yielding strain values of $2.3 \pm 1.2\%$ and $2.0 \pm 1.4\%$ for lengthening and shortening, respectively.

Repeatability of fiber direction strain patterns was tested within one volunteer. After completing the original protocol, the repeat protocol was executed:

1. Volunteer's torso was elevated again with the trunk support, while keeping the knee joint position consistent with the previous flexed position. Sets of 3D high-resolution MR and DT images were then acquired for the original protocol.

2. Subsequently, the trunk support was removed, and care was taken to maintain identical extended knee joint position as in the original acquisition. Separate sets of 3D high-resolution MR and DT images were acquired also for this repeat protocol. Testing was done while maintaining a relaxed state at all times.

Deformation analyses and tractography were performed for the original protocol and its repetition. Original protocol yielded a general pattern of fiber direction strains, which indicates that the proximal track segments are lengthened, whereas the distal ones are shortened. Repeat protocol matched that quite well (Figure 3.2).

3.3.5 Calculation of artifacts

Validity of demons algorithm in quantifying tissue deformations was shown with vigorous testing [93]. Presently, image sets of undeformed state were transformed by a "synthetic rigid body motion" imposed on data: 10° rotation within cross-sectional plane (representing endorotation of the knee during flexion [98]), 3° rotations in coronal and sagittal planes, and 4 mm translation axially. Subsequently, undeformed state and

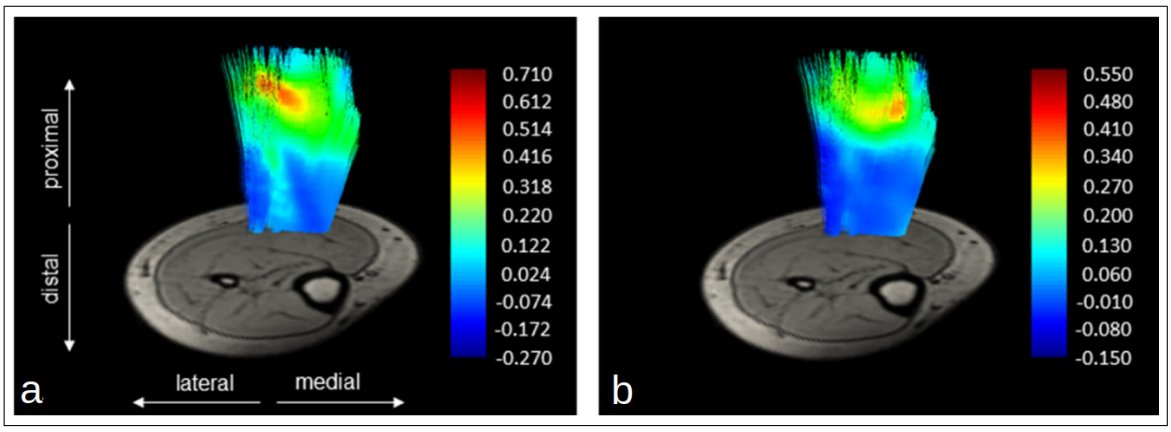

Figure 3.2 Results of the repeatability test. Fiber direction strain distributions occurring due to (a) original, and (b) repeat protocols match quite well. Note that strain amplitudes are somewhat smaller in the repeat protocol, which is ascribed to predominantly to viscoelastic properties of muscle and connective tissues.

these transformed image sets were compared. Displacement fields calculated using demons algorithm were mapped onto the tracked fibers. Theoretically, imposed rigid body motion should cause no strains. Therefore, resulting strains represent strain errors and volume errors.

3.3.6 Statistics

Fiber direction strain distributions deviate from normal distributions. Therefore, for lengthening and shortening separately, non-parametric Wilcoxon rank-sum tests were performed for differences between in vivo deformations and strain errors. Wilcoxon rank-sum tests were also performed to assess any changes of volume. Level of significance was chosen at $p > 0.05$.

Pair-wise comparisons of mean fiber direction strain along individual tracts for each volunteer were done based on Kruskal–Wallis with Dunn's post-hoc test. Ratio of the number of fiber pairs with statistically different mean strains to the total number of fiber pair combinations quantify parallel distribution of strain per each volunteer.

3.4 Results

Pooled data show mean $\pm$ SD of measurements from all volunteers:

1. Pennation angles equal $17.1 \pm 10.4°$.
2. Strain errors ($0.2 \pm 0.1\%$ and $3.3 \pm 0.9\%$ for lengthening and shortening, respectively) are small and are significantly different from fiber direction strains ($8.7 \pm 8.5\%$ and $7.5 \pm 4.6\%$ for lengthening and shortening, respectively) occurring due to knee extension imposed (Figure 3.3a).
3. Volume change (0.059 ± 0.005 error, vs. 0.050 ± 0.091) was insignificant.

Pooled strain data from all volunteers (Figure 3.3b), and strains visualized along GM tracts for each volunteer (Figure 3.4) indicate a serial distribution of fiber direction strains occurring within GM muscle fibers. Figure 3.4 shows that despite the globally lengthened condition of GM, locally lengthened and shortened parts are simultaneously present within the same tracts. For all volunteers, there is a general pattern indicating that proximal track segments are lengthened, whereas distal ones are shortened. However, inter-subject variability exists:

1. For volunteers A–D, approximately the proximal half of the tracts shows predominantly lengthening, whereas for volunteer E, this is limited to a much smaller portion.
2. Amplitude of local shortening (10–12% for volunteers A and B, 17% for volunteer D, whereas, 19% and even up to 23% for volunteers C and E, respectively) and lengthening (14–15% for volunteers A and B, whereas 26% and 35% for volunteers E and D, respectively, and up to 116.7% volunteer C) varies with a gradual transition from lengthening to shortening in the proximo–distal direction. Certain tracts present an opposite deformation pattern with shortening at proximal and lengthening at distal ends (e.g., by 15.4% and 25.4%, respectively in medial fascicles of volunteer D).

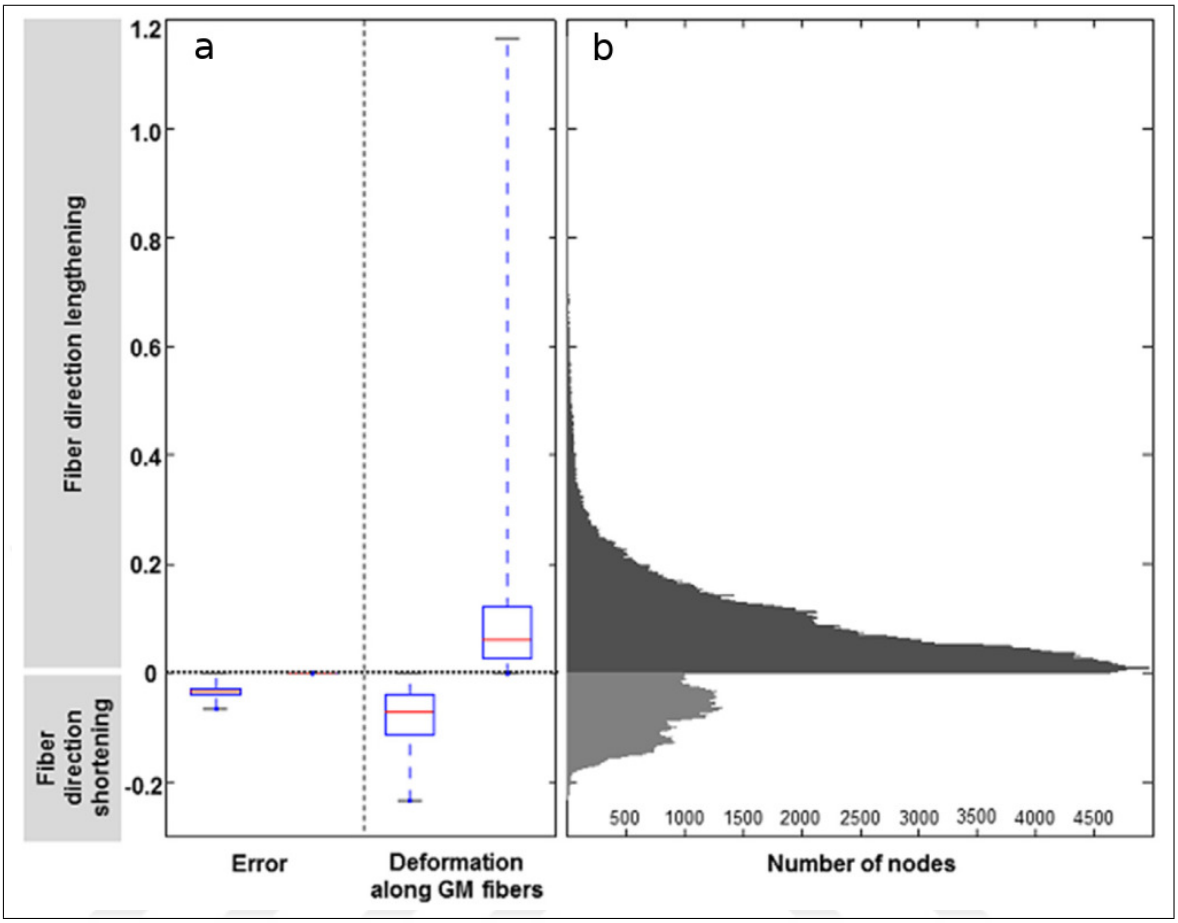

Figure 3.3 Effect of altered knee angle across all volunteers. Green–Lagrange strain tensor of each node rotated to align with the unit tangent vector of the corresponding GM tract yields fiber direction strain values presented as local fiber direction lengthening and shortening. (a) Box and whisker plots: horizontal line inside each box represents the median strain value; upper and lower edges of each box itself represent upper and lower quartiles respectively (i.e., 75th and 25th percentiles), and lines extending from each end of the box (whiskers) indicate peak values of fiber direction strains plotted. Left panel: strain errors. Right panel: strains along GM fibers due to imposed knee angle change. (b) Distribution of fiber direction strains of different nodes for pooled data from all volunteers.

Along-fiber shear strains visualized per volunteer (Figure 3.5) confirm the presence of much shearing between fascicles.

Distributions of mean fiber direction strains of different tracts for pooled data from all volunteers (Figure 3.6) indicate a parallel distribution of strain occurring among muscle fibers of GM. This is visualized for each volunteer in Figure 3.7. Parallel distribution of strain quantified equals 18.3%, 26.4%, 14.4%, 4.6% and 17.0% for volunteers A, B, C, D and E, respectively. For volunteers A, B and D, superficial tracts

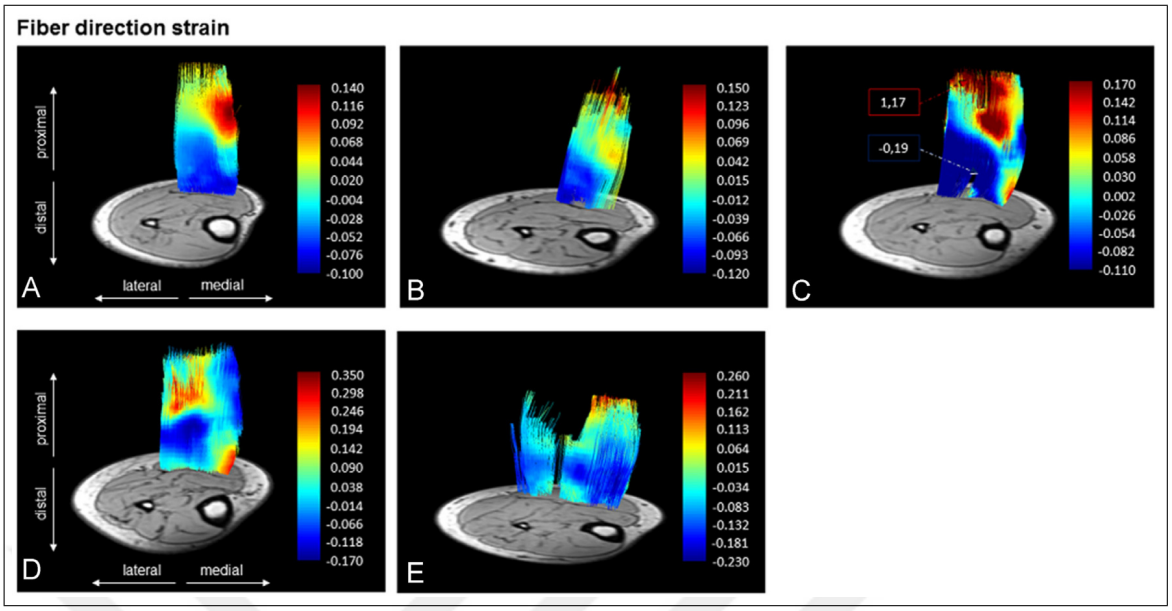

Figure 3.4 Serial distribution of fiber direction strain. (A)–(E) Fiber direction strains are mapped on identified GM tracts separately for each volunteer. A cross-sectional slice within the distal half of the diffusion weighted image volume is used as a reference. Negative values show local shortening and positive values show local lengthening. Strain upper limits are not normalized to reflect individual serial distribution differences. However, to achieve a better presentation, peak values of local shortening and lengthening are excluded for volunteer C. These values are indicated separately in the figure.

(corresponding to more distal muscle fibers) show negative mean strain, whereas positive values are calculated for deeper tracts. A gradient of mean fiber direction strains also exists for volunteers C and E. However, this shows a more complex characteristic indicating inter-individual differences.

Deep GM aponeurosis strains (mean $\pm$ SD of pooled data indicates $22.4 \pm 13.5\%$ and $17.2 \pm 7.9\%$ of peak local lengthening and shortening, respectively) show sizable inhomogeneity (Figure 3.8). Note that for about a fourth of the aponeurosis surface, was the deformation aligned with the Achilles tendon (6.7% and 20% of the voxels showed lengthening and shortening, respectively in that direction).

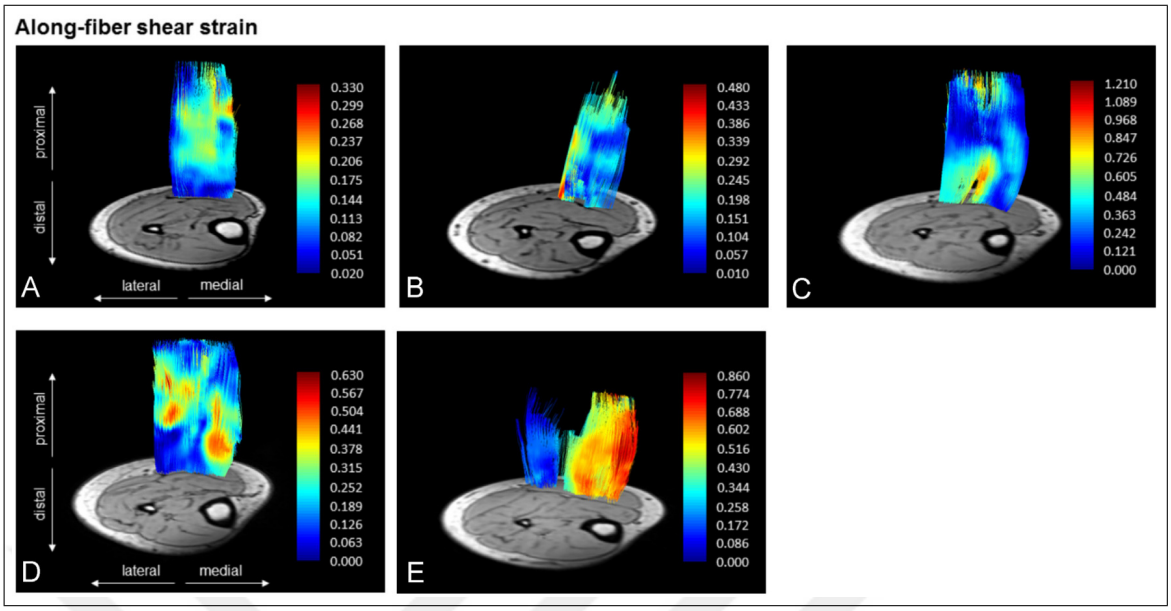

Figure 3.5 Along-fiber shear strain distributions. (A)–(E) Along-fiber shear strains are mapped on identified GM tracts separately for each volunteer. A cross-sectional slice within the distal half of the diffusion weighted image volume is used as a reference. Strain upper limits are not normalized to reflect individual serial distribution differences.

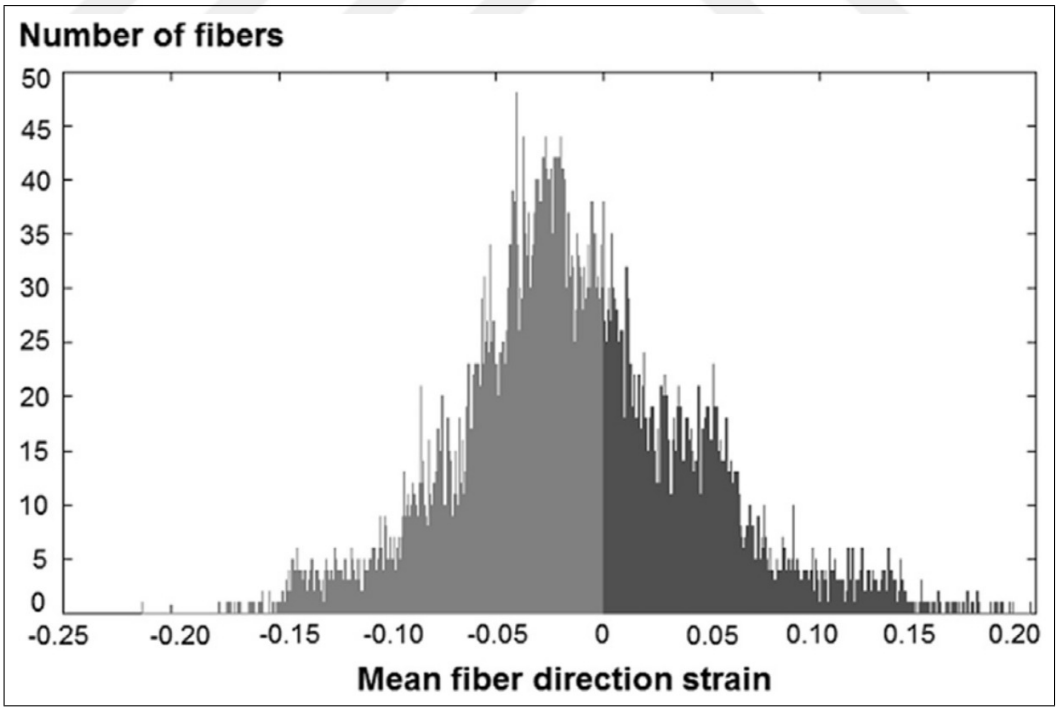

Figure 3.6 Distributions of mean fiber direction strains of different tracts from pooled data from all volunteers. Histogram indicates a parallel distribution of strain among different GM fiber tracts. Negative values represent shortening and positive values represent lengthening.

3.5 Discussion

3.5.1 Methodology developed

Methods for quantifying muscle tissue deformation in context of muscle architecture are lacking:

1. Ultrasound studies are limited to either two dimensional deformation analyses [37] or three-dimensional structural analyses [127].
2. MRI analyses in a single slice [45] or a three-dimensional volume [46, 93, 128] yield a good representation of muscle tissue deformation, however physiologically relevant fiber direction length changes remain unknown.
3. Numerous studies utilizing DTI and tractography provide anatomical information for human muscle fibers in vivo [57, 60, 62, 122], but they provide no information regarding deformation. Among limited number of studies combining DTI and deformation analyses, Englund et al. [119] analyzed contraction-induced deformation within muscle volume. However, without doing fiber tractography, they made a voxel-wise comparison of peak principal strain's direction with principal diffusion direction and showed no consistent match. Felton et al. [129] did perform tractography and aligned the strain-rate tensor obtained during muscle activity with resulting fiber tracts. However, imaging was confined to only two slices, thus not informative for the general muscle volume.

We have combined deformation analyses in three-dimensional muscle volume with DTI and tractography. This allows localizing muscle fascicles and mapping fiber direction deformations along them. This is a major step for understanding muscle mechanics and physiology. Pennation angle of tracked fibers and standard deviation of pennation angles agree with previous reports [61, 123] indicating anatomical representativeness of the method developed. Calculation of tissue deformations relies on demons algorithm which, has been utilized and validated for calculating deformations

in various tissues including pelvic floor [99], lung [100] myocardium [96] and cortical bone [130]. Deformation of human lower leg musculature was also assessed [46, 93].

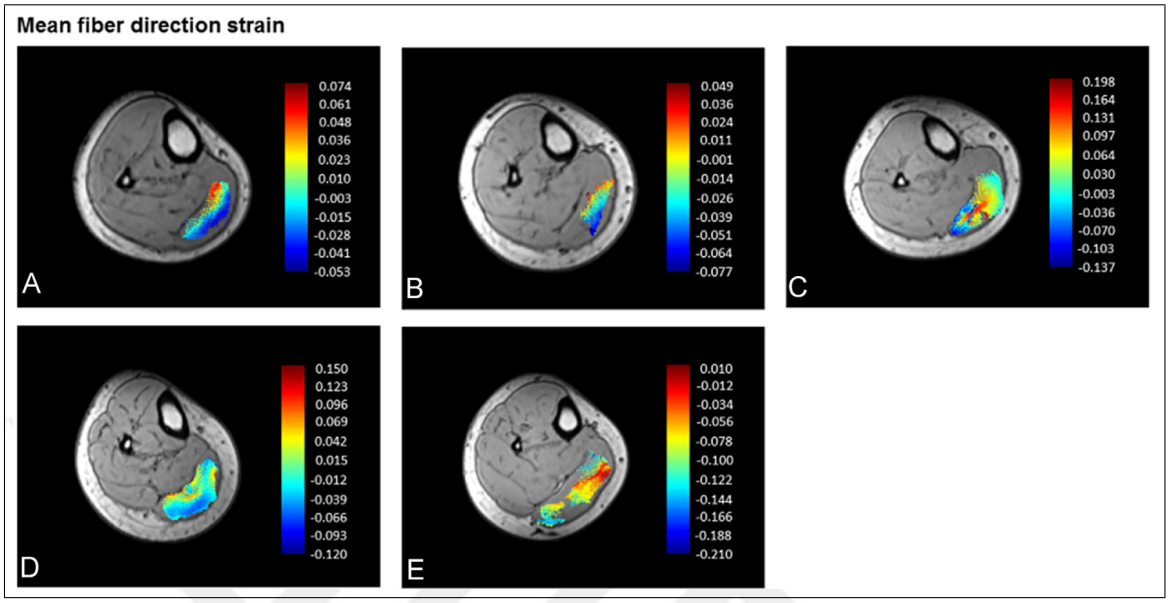

Figure 3.7 Parallel distribution of fiber direction strain among different GM fiber tracts per volunteer. (A)–(E) Mean fiber direction strains of different tracts are mapped on a reference cross-sectional slice separately for each volunteer. Reference slice is chosen so as to maximize fiber representation within muscle cross-section. Negative values represent shortening and positive values represent lengthening. Strain limits are not normalized to reflect individual parallel distribution differences.

A rigid body motion test was performed by imposing synthetic motion on image sets, which represents a much larger scale motion than possible subject movement during imaging. This should theoretically cause zero strain and indeed yielded very small error strains also presently. Yaman et al. [93] conducted further critical testing of the reliability of demons algorithm by imposing known deformations on the image sets. One key finding was that the strains calculated are conservative estimators of actual local deformations. To the best of our knowledge no data is available in the literature, which presents amplitudes of strain occurring along human GM fibers upon passive knee extension in vivo. Therefore, a direct comparison of the strains shown presently is not possible. Using ultrasonography in passive state, De Monte et al. [131] measured the changes in GM fascicle lengths. Their data depicted at knee angles of 144°and 174°indicates that imposed knee movement at constant ankle position causes approximately 18% fascicle strain. Our findings show for similar test conditions that strain along GM tracts will vary from approximately 8% shortening to 9% lengthening.

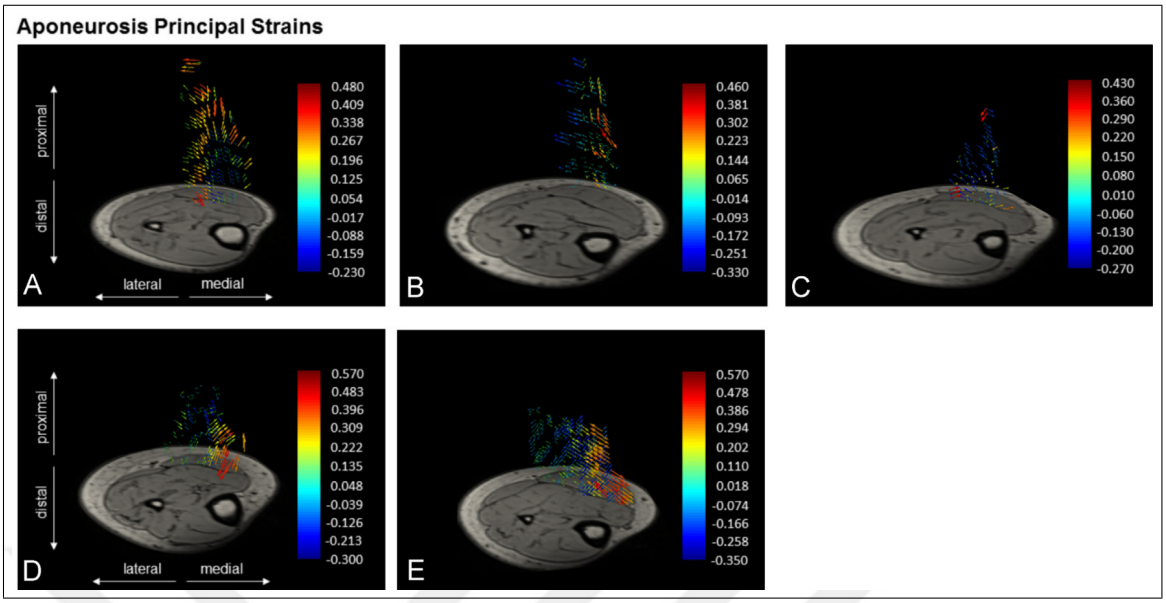

Figure 3.8 Distribution of deep GM aponeurosis strains per volunteer. (A–E) Deformation fields are visualized using glyphs. Each glyph represents deformation of a voxel. Direction of each glyph is determined by corresponding eigenvector. Length of each glyph is proportional to magnitude of local aponeurosis tissue lengthening or shortening. A cross-sectional slice within the distal half of the diffusion weighted image volume is used as a reference. Strain upper limits are not normalized to reflect individual serial distribution differences.

Although the order of magnitude of strain values agrees, we don't know the overall fascicle length change. Yet, we know from a combined cadaver and MRI assessment that global muscle length changes on imposed joint movement can be quite different from local ones [46]. Therefore, a match between fascicle length changes and local fiber direction strains is unlikely. On the other hand, for a comparable knee angle change imposed, Yaman et al. [93] assessed principal strains within lower leg muscles including m. gastrocnemius. Mean of peak local lengthening and shortening that they reported ($10.3 \pm 1.0\%$ and $9.7 \pm 1.0\%$, respectively) were indeed comparable to present strain amplitudes. Note however that those peak strains were higher than present fiber direction strains. This agrees with the conclusion of Zhong et al. [44] and Englund et al. [119] that the peak length changes within a muscle occur not necessarily along the muscle fibers. New studies are indicated to achieve a good understanding of gross muscle and fascicle length changes vs. local fiber direction strains as this has high functional relevance. The mechanism providing a biomechanical explanation to the heterogeneous nature of local strains shown presently is addressed below.

Overall, demons algorithm is highly suitable for assessing muscle tissue deformations within a three-dimensional volume with fairly good resolution. Note that, no pre-processing was performed on MRI data prior to the deformation analyses:

1. Avoiding resolution matching between MR and DT images prevents data from plausible non-physiological outcome of related interpolations.
2. Aligning MR image coordinates rigidly with DT image coordinates avoids synthetic deformation. Deformation vectors obtained were mapped to the correct coordinate system representing deformed state fibers.

In sum, we demonstrate a novel and reliable tool capable of assessing human muscle function in vivo, by utilizing physiologically relevant fiber direction strains.

3.5.2 Explanations for inhomogeneity of muscle fiber direction strains

A major finding is inhomogeneity of muscle fiber direction strains. This involves a general fiber direction strain pattern showing lengthened proximal and shortened distal track segments. Hence local lengthening can occur simultaneously with local shortening within different parts of the same tracts. Repeatability test conducted confirmed consistency of such general deformation pattern. Strain artifacts cannot explain this because the amplitudes of muscle fiber direction strain distribution are much higher. Inter-sarcomere dynamics [132], or instability theories [133, 134] also cannot explain such inhomogeneity because of the inactive state of present testing. Note that earlier modeling [88, 124, 135] and MR imaging analyses [44] did show inhomogeneity of strain within muscle. Blemker et al. [136] developed a model which incorporates skeletal muscle mechanical properties and structural properties of biceps brachii muscle to assess the causes of non-uniform strains reported earlier in a dynamic imaging study by Pappas et al. [41]. They attributed distribution of length changes along the fascicles primarily to muscle architecture including fascicle length and curvature variations within muscle. Authors also reported major along-fiber shear strains and indicated

this as a factor affecting the potential for muscle fibers to transmit force laterally via intra-muscular connective tissues. Particularly considering force transmission in series-fibered muscle, concept of shear linkage between adjacent structures by intra-muscular connective tissues was introduced [2, 137, 138, 139]. Our present findings also show substantial along-fiber shear strains representing shearing between GM fascicles. As muscle fibers are not directly connected to each other, such shearing presents evidence for major mechanical interaction occurring between the muscle fibers and the extra-cellular matrix (ECM). This mediates interaction between different muscle fibers and comprises a mechanism for muscle architecture to affect deformation along muscle fibers. Hence, muscle fiber–ECM mechanical interactions are central to the biomechanical explanation of the present findings. In general, deformation along any member is determined by the force equilibrium. Muscle fibers are widely considered as members under uniaxial loading because they are regarded as mechanically constrained only at their ends, where the myotendinous junctions (MTJs) are [25]. For such a member, the deformation should be uniform along its length, but the present findings do not confirm this. However, muscle fibers and the ECM have multi-molecular connections along the full peripheral length of the muscle fiber [89]. Therefore, additional to the forces acting on a muscle fiber at MTJs, loads can act also along its full length. Accordingly, considering muscle fiber as a member under uniaxial loading is mechanically incomplete. In an earlier experiment, Street [21] freed a muscle fiber from its surrounding fibers only in the middle and assessed its length changes on imposed passive stretch. This yielded different sarcomere lengths in exposed fiber, indicating inhomogeneous deformation. This mechanism has been referred to as myofascial force transmission [23], and the loads along the muscle fiber originating from the ECM and the neighboring muscle fibers have been referred to as myofascial loads [32]. Huijing et al. [22] and Jaspers et al. [140] showed that a discontinuity in the ECM affects functioning of muscle fibers differentially within muscle and causes muscle force to change. Mechanism of effects of muscle fiber–ECM mechanical interactions has been studied extensively using finite element modeling (FEM), which confirmed theoretically that myofascial loads can cause inhomogeneity of fiber direction strains with major implications for muscle's force production [24, 141] and outcome of treatments [66, 67, 68, 142]. Present data shows valuable evidence for this mechanism for human muscles in vivo.

Note the analogy between a muscle fiber and the whole muscle. Although MTJs are essential for bodily movement, they are not the exclusive sites for mechanical interaction between muscle belly and its surroundings. Instead, direct collagenous linkages exist between the epimysia of adjacent muscles. Additionally, collagen reinforced neuro-vascular tracts (NVT) provide indirect inter-muscular connections between distant muscles (e.g., [31]). These connections are in continuity with other connective tissues such as inter-muscular septum, inter-osseal membrane, and compartmental fasciæ and show complex mechanics stemming from non-linear, inhomogeneous material properties, and pre-strain [28]. Joint movement causes relative position of muscle belly to change leading to stretching of those tissues connecting it to its surroundings [143]. Consequently, epimuscular myofascial loads of varying magnitudes and directions can act along muscle belly and further affect muscle's mechanics via muscle fiber–ECM mechanical interactions [32].

Present experiment involves knee extension. This means that the proximal end of GM is stretched in the proximal direction because it spans the knee joint. Fascicle lengthening in the proximal GM regions agrees with the imposed muscle stretch by the tendon. However, variation of that along those fascicles and shortening occurring in distal GM regions cannot be explained solely by imposed muscle stretch. Instead, findings indicate presence of distally directed epimuscular myofascial loads acting along the fascicles. Note that rest of the lower leg muscles are mono-articular, spanning only the ankle joint. Therefore, upon imposed knee extension, GM position relative to those muscles is changed. Hence, not only the muscle, but also its epimuscular connections are proximally stretched causing distally directed epimuscular myofascial loads to act on GM muscle belly. These loads affect mechanical equilibrium locally inside the muscle, which explains the diminished elongation in proximal regions of GM fascicles towards mid-GM muscle belly and the compression in distal regions. This is also reflected on distribution of deep GM aponeurosis strains. However, inter-subject variability exists indicating that magnitudes and directions of those loads should be more complex, ascribed to complex mechanical properties of epimuscular connections. Plausibly, stiffer collagenous linkages between GM and SOL muscles could contribute to the complexity in strain distributions, anchoring fascicle parts in more distal GM

regions.

Bojsen-Møller et al. [37] showed displacement gradients in GM and SOL muscles upon passive knee extension, capable of imposing differential myofascial loading. Others presented heterogeneous local deformations [46] and fascicle length changes [144] within SOL despite being in global isometric condition ascribable to myofascial interaction mechanism. Contribution of the shared distal tendon providing mechanical coupling of GM and SOL muscles cannot be overlooked [144, 145]. However, inter-muscular mechanical interaction via the shared tendon cannot be the dominant mechanism for present findings since the length changes reported by e.g., Tian et al. [144] for the Achilles tendon are much smaller than those shown locally within the muscle. Besides, interaction via the Achilles tendon is unlikely to lead to sizable fascicle shortening in passive test conditions. Present imaging did not involve the tendons. Hence, no deformation data is available for the Achilles tendon. However, deep GM aponeurosis strains are heterogeneous over its surface. This supports previously shown aponeurosis strain distributions [136, 146, 147] in a three-dimensional analysis. Moreover, direction of the peak deep GM aponeurosis strains is not necessarily aligned with the Achilles tendon. These findings indicate that myotendinous structures play a highly complex role in muscle functioning, which involves not only transmission of muscle force to the tendon but also sustaining the mechanical equilibrium within muscle by bearing loads in various directions and amplitudes.

3.5.3 Limitations and implications

Tracts obtained are representative of muscle fascicles and not individual muscle fibers. This is bound by the resolution of the state of the art DTI acquisition methods for large enough muscle volumes. Wu et al. [148] reached a finer, 0.125 mm isometric resolution for DTI acquisition. However, they worked on rat brain, which requires a much smaller field of view compared to human muscles. On the other hand, using a comparable field of view at the cost of assessing a local small muscle volume only, would still be insufficient for resolving individual sarcomeres. Therefore, the present

methodology provides a superb tool for assessing physiologically relevant human muscle tissue deformations in vivo, but calculates length changes of only large groups of sarcomeres within a volume. Consequently, possible distribution of sarcomere length changes along several segments of fascicles can be determined objectively. Accordingly, the strain values obtained represent averages of those of numerous sarcomeres within a voxel. Hence, deformation heterogeneity along the tracked fascicles can be considered to underestimate the underlying heterogeneity at sarcomere level.

The present study shows serial and parallel distribution of strain along the GM fibers, which, bound to the limitations addressed may represent serial and parallel heterogeneity of sarcomere lengths. Serial sarcomere length distributions were correlated to muscle's length range of force exertion [149, 150]. Moreover, a shift of muscle optimum length to a longer length was shown with increasing parallel heterogeneity [151]. Previous modeling showed mechanism of that in healthy (e.g., [68, 88]) and treated muscle [67, 68], and how that relates to muscle length range of force exertion. Therefore, the metrics our methodology provides are relevant for assessing changes in joint range of motion of human subjects. This is a central parameter for human mobility, as decreased joint mobility is a common problem in e.g., cerebral palsy patients [152]. Pre- vs. post-treatment comparison of such patients using the present technique can help assess the outcomes of common interventions (e.g., aponeurotomy, botulinum toxin injections) objectively.

The present study was performed in passive conditions. However, the methods described here can also be applied to conditions involving sub-maximal effort. These conditions can be used to simulate postural demands of daily tasks such as driving, key pressing, cycling. Human muscle function can be assessed with potential implications also for ergonomics. The acquisition time may limit the effort level, and lack of joint movement during acquisition could be considered a limitation. Yet, a single joint angle manipulation in active or passive state suffices for the assessment of targeted deformation along the fiber direction within a three-dimensional muscle volume. Other imaging methods with repetitive joint motion requirements could present a problem particularly for patient groups with movement disorders, such as cerebral palsy patients. However,

an appropriate use of the present methodology can allow for a major improvement in our understanding of the condition of these patients' muscles.

In conclusion, using advanced MRI–DTI techniques combined, a methodology was developed which yields physiologically relevant muscle fiber direction deformation information. Effects of knee movement assessed indicate major strain distribution along human GM muscle fibers.

4. FINITE ELEMENT MODELING ASSESSMENT OF THE MECHANISM OF COMBINED LOCAL LENGTHENING AND SHORTENING ALONG MUSCLE FIBERS

4.1 Introduction

Findings of the previous chapter indicating negative mean fiber direction strain within distinguished tracts belonging to in vivo lengthened GM [153] does not imply fascicles that shortened on average [154, 155]: it must be noted that tractography was limited to fascicle lengths of 30–50 mm based on Chow et al. [123], however it is possible that the analyzed tracts might be incomplete fascicle segments, thus are not representative of an allegedly erroneous global shortening of fascicles within lengthened passive muscle. Indeed, others have found human GM fascicles to be above [156, 157] the fascicle length interval considered during the tractography performed in previous chapter. A more comprehensive way of performing tractography to ensure full coverage of each fiber is using aponeuroses as tract seeding points [61], however tractography software did not allow much user intervention graphically at the time, thus tracts were seeded from polygonal regions of interest within GM, marked on b0 images [153]. While such cases are possible considering remainder musculature of the limb, along with relevant connectome to include the inter-muscular linkages and a more extensive representation of the NVTs, shortening of entire fascicles within a passively lengthened muscle is not considered within context of the present work.

Also among the findings of the previous chapter are fascicles with lengthening and shortening sections, despite globally lengthened state of in vivo GM muscle. Such deformation distributions were indeed shown in numerous model studies (for a review, see [32, 141]) and their particular implications on muscle function were discussed. In particular, a previous model study took extra-muscular linkages of muscle into account in order to peer into local metrics of strain and stress within muscle [88, 143], which were also globally studied as muscle length and force [88, 33]. However, experiments

of the previous chapter were conducted in the passive state [153]. Therefore, an assessment of the principles of the mechanical mechanism for shortened sections within fascicles of a globally lengthened passive muscle is needed and finite element modeling (FEM) is an ideal tool for that. To address this, present chapter aimed at studying the effects of imposed muscle relative position changes and certain muscle lengthening of passive EDL muscle of the rat using FEM. An increased understanding of local mechanics within muscle and its anatomical relations to extra-muscular linkages, particularly NVTs, will help illustrating the plausible role of epimuscular myofascial loads on imposing locally shortening regions within a longer muscle.

4.2 Methods

4.2.1 Description of the "linked fiber–matrix mesh model"

In the linked fiber–matrix mesh model (LFMM model), skeletal muscle is considered explicitly as two separate domains:

1. The intra-cellular domain and
2. the extra-cellular matrix (ECM) domain.

The trans-sarcolemmal attachments are considered as elastic links between the two domains. Two self-programmed elements were developed and were introduced as user-defined elements into the finite element program ANSYS 12.0 [24, 88]. One of these elements represents the ECM, which includes the basal lamina and connective tissue components such as endomysium and perimysium (ECM element). A second element models the muscle fibers (myofiber element). Within the biological context, the combined muscle element represents a segment within a large bundle of muscle fibers with identical material properties, its connective tissues and the links between them. This is realized as a linked system of the ECM and myofiber elements. A

schematic 2D-representation of an arrangement of these muscle elements is shown in Figure 4.1a and elsewhere [67].

In LFMM model, the ECM domain is represented by a mesh of ECM elements (matrix mesh). Within the same space, a separate mesh of myofiber elements is built to represent the intra-cellular domain (fiber mesh). These two meshes are rigidly connected to single layers of elements modeling the proximal and distal aponeuroses also at myotendinous connection sites and are linked elastically at the intermediate nodes. The ECM and myofiber elements each have eight nodes, linear interpolation functions and a large deformation analysis formulation. A 3D-local coordinate system representing fiber, cross-fiber (normal to the fiber direction) and thickness directions is used.

4.2.2 Myofiber element

Passive muscle is studied and sarcomeres are assumed to have identical material properties within muscle fibers. Force–velocity characteristics are not considered due to isometric nature of present work. Total stress of the intra-cellular domain (σ_{22}) is a Cauchy stress acting in local fiber direction exclusively and is the sum of active stress produced by contractile elements ($\sigma_{22contr}$) and stress due to titin ($\sigma_{22titin}$). It is assumed that, at initial muscle length in passive state, sarcomeres arranged in-series within muscle fibers have identical lengths and material properties, and fiber direction strain (ϵ_{22}) is zero.

To define stress due to titin in passive state, experimental tension–sarcomere length data [158] for single rabbit skeletal muscle fibers was fit with a quadratic function (Eq. 4.1, Figure 4.1) and scaled to make it compatible to the stress–strain characteristics of the contractile part, described in Chapter 5.

$$\sigma_{22titin}(\epsilon_{22}) = \begin{cases} t_1\epsilon_{22}^2 + t_2\epsilon_{22} + t_3 & \text{if} \quad \epsilon_{22} > 0 \\ 0 & \text{if} \quad \epsilon_{22} < 0 \end{cases} \tag{4.1}$$

where t_1, t_2 and t_3 are constants (Table 4.1).

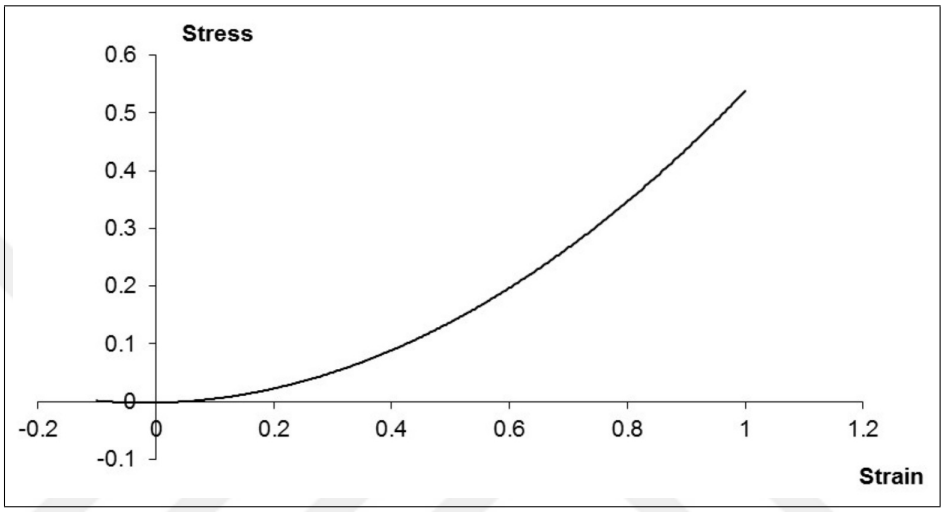

Figure 4.1 Stress–strain relation for intra-cellular passive elements representing titin in the myofiber element, per Eq. 4.1.

4.2.3 ECM element

The ECM element represents the basal lamina and intra-muscular connective tissue components including the endomysium, perimysium and epimysium. A strain energy density function accounts for the non-linear and anisotropic material properties, and the constancy of muscle volume.

Stress formulation, $\underline{S}$, based on second Piola–Kirchoff definition constitutes the derivative of strain energy density function, W, with respect to the Green–Lagrange strain tensor, $d\underline{L}^G$.

Table 4.1
Values and definitions of the model constants.

Constant	Value	Definition
t_1	0.522	Coefficient for stress–strain relation of the intra-cellular passive elements (Eq. 4.1)
t_2	0.019	Coefficient for stress–strain relation of the intra-cellular passive elements (Eq. 4.1)
t_3	-0.002	Coefficient for stress–strain relation of the intra-cellular passive elements (Eq. 4.1)
k	0.05	Initial passive stiffness (Eq. 4.4)
a_{11}	8.0	Passive cross-fiber direction stiffness, $a_{11} = a_{33}$ (Eq. 4.4)
a_{22}	6.0	Passive fiber direction stiffness (Eq. 4.4)
a_{12}	6.0	Passive cross-fiber direction stiffness, $a_{12} = a_{23} = a_{31}$ (Eq. 4.4)
λ_S	5.0	Weight factor in the penalty function for the solid volume (Eq. 4.5)
λ_F	20.0	Weight factor in the penalty function for the fluid volume (Eq. 4.5)

$$\underline{S} = \frac{dW}{d\underline{L}^G} \tag{4.2}$$

The strain energy density function that mechanically characterizes the ECM consists of two parts:

$$W = W_1 + W_2 \tag{4.3}$$

The first part represents the non-linear and anisotropic material properties [159]:

$$W_1 = W_{ij}(\epsilon_{ij}) = \begin{cases} k\,[\,e^{a_{ij}\cdot\epsilon_{ij}} - a_{ij}\cdot\epsilon_{ij}\,] & \text{if} \quad \epsilon_{22} > 0 \\ 0 & \text{if} \quad \epsilon_{22} < 0 \;\; or \;\; i \neq j \end{cases} \tag{4.4}$$

where ϵ_{ij} are the Green–Lagrange strains in the local coordinates. The indices $i = 1, \ldots, 3$ and $j = 1, \ldots, 3$ represent local cross-fiber, fiber and thickness directions,

respectively. a_{ij} and k are constants (Table 4.1). Resulting stress–strain curves are shown in Figure 4.2.

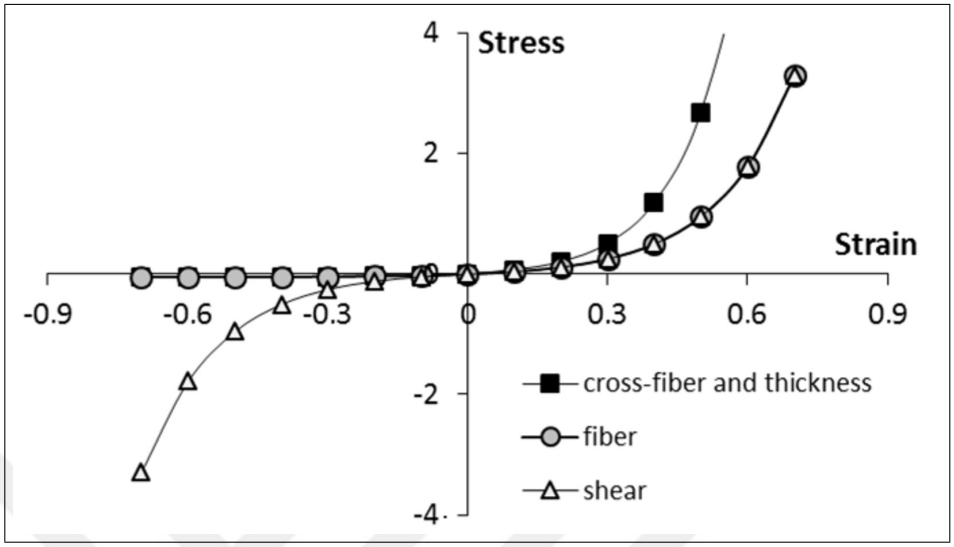

Figure 4.2 ECM element's stress–strain relations in cross-fiber and thickness, along-fiber, and shear directions, per Eq. 4.4.

The second part includes a penalty function to account for the constancy of muscle volume:

$$W_2 = \lambda_S \left(I_3 - 1\right)^2 + \lambda_F \left(I_3^{avg} - 1\right)^2 \tag{4.5}$$

where, I_3 is the third invariant of the right Cauchy–Green strain tensor and is a measure for the local volume for each Gaussian integration point. If all the I_3s are kept as one, the element is considered as solid and the local volumes are conserved. If the weighted mean of all I_3s per element, $I_3^{avg} - 1$, is kept as one, the element is considered as a fluid. Penalty parameters λ_S (for solid volume) and λ_F (for fluid volume) (Table 4.1), allow determining the emphasis given for each part.

4.2.4 Elements linking fiber and matrix meshes

For the elastic links between two meshes, which represent the trans-membranous attachments between the cytoskeleton and the ECM, COMBIN39 standard element from ANSYS 12.0 element library is used. This is a 2-node uniaxial spring element, defined separately and identically for each global direction, with linear stiffness characteristics determined according to Yucesoy et al. [88].

4.2.5 Aponeurosis element

To represent the aponeuroses, HYPER58 standard 3D, 8-node element from ANSYS 12.0 element library is used. This element has a hyper-elastic mechanical formulation and its strain energy density function is defined using Mooney–Rivlin material law.

4.2.6 Model of EDL muscle with extra-muscular connections

EDL muscle of the rat is modeled. This muscle has a relatively simple geometry: it is a unipennate muscle with rather small pennation angles and with minimal variation in fiber direction within the muscle belly. Geometry of the model is sufficiently defined as contour of the longitudinal slice at the middle of the isolated rat EDL muscle belly. Three muscle elements in-series and six in-parallel fill this slice (Figure 4.3, bottom panel). Therefore, any collection of three muscle elements arranged in-series represents a rather large muscle fascicle. All aponeurosis elements have identical mechanical properties but using a variable thickness in the fiber–cross-fiber plane, the increasing cross-sectional area of the aponeurosis toward the tendon is accounted for (Figure 4.3, top panel). Elements representing the extra-muscular connections for the three proximal fascicle interfaces are four times stiffer than the remainder 4 distal fascicle interfaces (Figure 4.3, top panel).

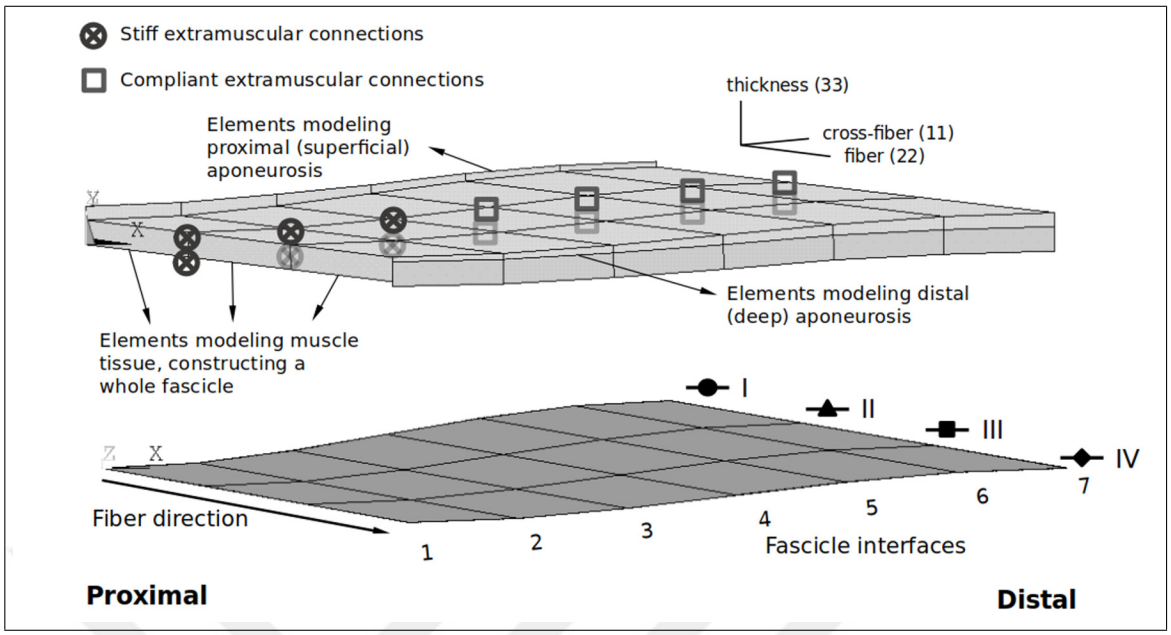

Figure 4.3 Geometry of the rat EDL model studied. Locations and stiffness of the extra-muscular connections (top panel), fascicle interfaces (1–7) and serial fascicle sections (I–IV) (bottom panel).

4.2.7 Solution procedure

Analysis type used in ANSYS is static and large strain effects were included. Throughout the solution procedure, studied models are stable and no mesh refinement is performed. A force-based convergence criterion is used with a tolerance of 0.5%.

The muscle was kept passive throughout the analysis. Through alternating translation of the proximal and distal end nodes, the modeled muscle was displaced distally (ΔEDL position) by 7 mm. This caused the ends of the spring elements providing extra-muscular connections connected to the muscle to be displaced and as the other ends were kept mechanically grounded, these connections were stretched. Once relative position change was complete, the proximal end of the muscle was fixed and the distal was displaced 0.5 mm distally to impose muscle lengthening. Consequently, epimuscular myofascial loads were developed to act on the muscle. Note that, ΔEDL position = 0 mm was referred to as the reference case and ΔEDL position = 7 mm was referred to as the relative position change case.

4.2.8 Processing of data

Strain (ϵ_{22}) along nodes of serial fascicle sections (I–IV) were studied across fascicle interfaces 1–7, to quantify local deformations throughout muscle in reference and relative position change cases.

4.3 Results

4.3.1 Strain along serial fascicle sections I–IV

For the reference case all nodes of all fascicles show positive strains indicating occurrence of only lengthening along every fiber (Figure 4.4a). Per serial sections I–IV, nodes of sections I and II present monotonous decrease in strain proximo–distally (across interfaces 1–7), whereas sections III and IV present monotonous increase across same direction. This is due to model geometry and extra-muscular linkages. Yet, fiber direction strain IQR for fascicle interfaces remained small, between 0.34 and 2.34% (Figure 4.4b).

In contrast, for the relative position change case, the distal lengthening imposed resulted in shortening of all nodes across section I (Figure 4.4c). Shortening is more restricted in the first three nodes with stiffer extra-muscular connections. Such variation in the restriction of myofascial constraints persists also for all other serial sections, however section II presents near-zero strains for all its nodes, indicating no noteworthy local length change across this section, whereas sections III and IV present only positive strains, thus only lengthening segments of fibers. Similarly, IQRs for fiber direction strains per fascicle interface remained variable: for section II which is along the extra-muscular connections, IQR is down to 1.76%, while for remainder sections II–IV, it is in excess of 11.9% (Figure 4.4d).

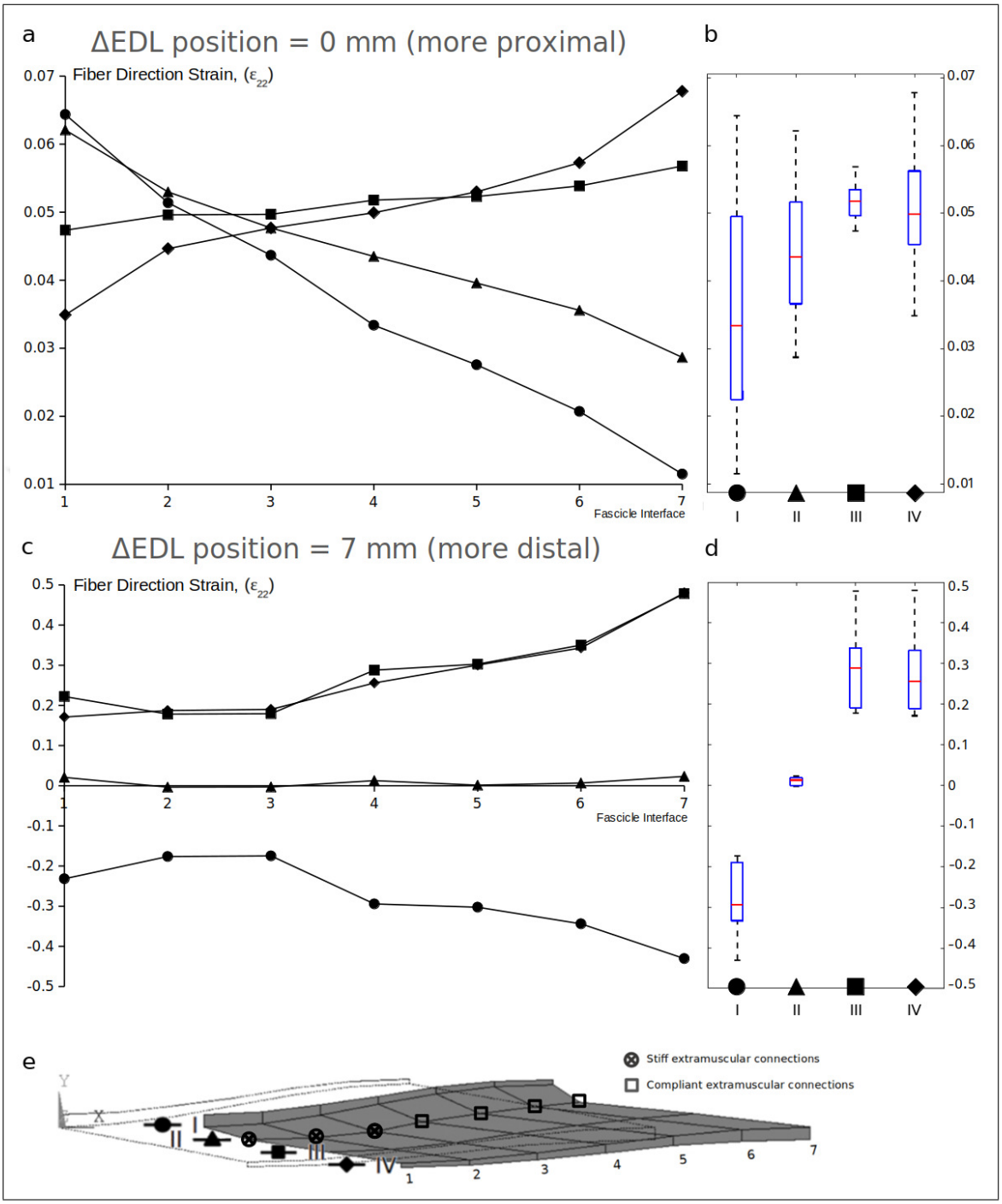

Figure 4.4 Nodal fiber direction strains per serial sections I–IV vs. fascicle interface curves at long muscle length without (a) and with (c) relative position change. For each case, distributions of fiber direction strain across fascicle sections are also depicted using box and whiskers in (b) and (d), respectively. Locations of serial sections I–IV, fascicle interfaces 1–7 and extra-muscular connections are reminded in (e).

4.4 Discussion

Relative position change of passive muscle was assessed presently to help understand heterogeneous distribution of strains along muscle fibers, in contrast to previous

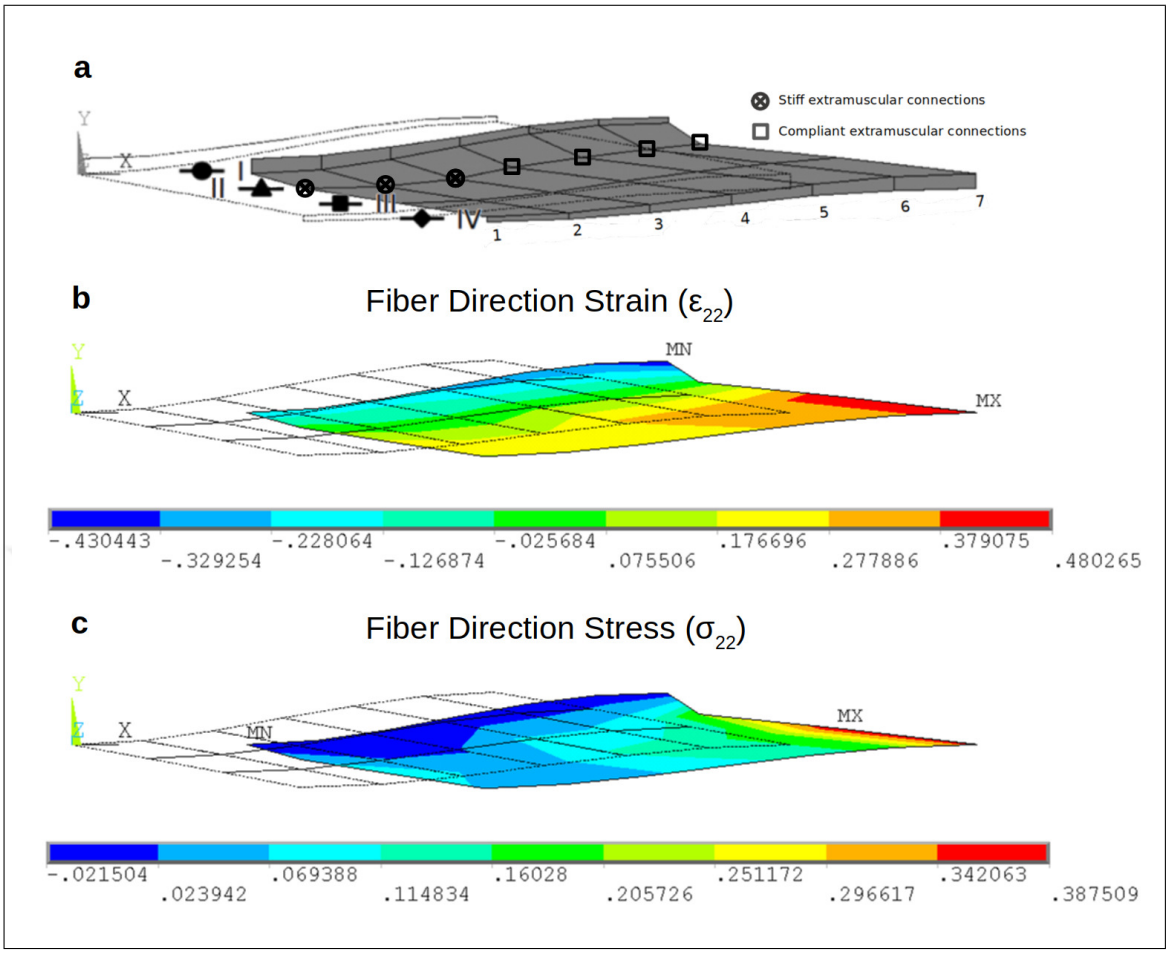

Figure 4.5 Fiber direction strain and stress contour plots for model with extra-muscular connections, after 7 mm distal relative position change and subsequently lengthening to L_{opt} + 0.5 mm. Locations of fascicle sections I–IV, fascicle interfaces 1–7 and extra-muscular connections are reminded (a). Fiber direction strain plot depicts much shortening in proximal fascicle sections, with lengthening in distal sections (b). Note the near-zero strain zone corresponding to section II, where the extra-muscular connections are (a). Most extreme stresses are observed for distalmost fascicle and negative stresses are limited to sections proximal to the extra-muscular connections (c).

model study of fully active muscle [143]. Such relative position changes stretch muscle's extra-muscular connections causing forces to develop and act on the muscle at locations of their mutual intersections. The net value of those epimuscular myofascial loads result in increasing proximo–distal force differences of the muscle (not shown) globally. More importantly, locally, the mechanical equilibrium within the muscle is altered, which in turn results in shortened axial sections within muscle fibers, despite total length increase in the fibers.

Between sections I and II, average strain for all fascicle interfaces are negative, indicating sections of fascicles with shortening only. Note that the extra-muscular connections are along section II, where a mechanical balance is established at zero strain. Increase in magnitudes of strains across fascicles after fascicle interface 3 is due to the change in the compliance of the extra-muscular connections. Strain magnitudes increase distally too, due to change in aponeurosis thickness and model geometry with remainder heterogeneity due to model geometry. At $L_{opt} + 0.5$ mm, in model with relative position change, there exists wide shortening fascicle segments whereas without relative position change, such heterogeneity does not present.

Fascicle sections I and II, i.e., proximal sections of modeled fascicles, coincide with the shortened distal sections presented in human experiment of previous chapter, where proximally directed lengthening was imposed by femur via GM's proximal tendon. As such, present model study did show shortened segments (Figure 4.4b and Figure 4.5, fascicle sections I and II, represented by circle and triangle, respectively) within overall lengthened fascicles of passively lengthened muscle. Also recall that reconstructed tracks represent only part of GM, and not the entire muscle. Thus it is possible, and also of great interest to see whether such shortening biased results occur when all GM fascicles are included. Finally, magnitudes of lengthening and shortening along fascicles do seem to coincide in present analyses (Figure 4.4d). Regardless, present chapter emphasizes how extra-muscular structures such as NVTs affect strain distributions within muscle fascicles. Indeed, we have shown similar interactions in another experiment [160], results of which are exemplified in Appendix B.

While it is clear that human GM muscle and the rat muscle modeled are not the same, such modeling facilitated an assessment of the principles of the issue. It must be noted that the NVTs and other myofascial structures are plausibly non-linearly stiff in human [161] with conceivable pre-strain on them [28]. Consequently, similar muscle relative position changes imposed as those studied presently can force the in vivo muscle's epimuscular connections to operate in the stiffer parts of their respective length-force relationships leading to building up of higher and possible more variable myofascial loads to act on different parts of the muscle. Note also that, only a certain

limited muscle lengthening was imposed presently, which in vivo, may be much more pronounced with joint position changes. Therefore, different, more complex and plausibly more pronounced effects of local length changes are tenable for muscle function in vivo. Thus, considerations regarding in vivo limitations on relative position change of rat EDL muscle [154] are disregarded in favor of other previous studies [33, 143] assessing the core of the issue. As such, present modeling was capable of showing that epimuscular myofascial loads developed; and acting on the modeled muscle, were capable of representing the local effects seen in the human study [153].

5. FINITE ELEMENT ASSESSMENT OF TITIN'S POTENTIAL ROLE IN MUSCLE'S FORCE PRODUCTION

5.1 Introduction

Two-myofilament model of the sarcomere's force production has long been used to explain various phenomena in muscle physiology. Thin and thick myofilaments of the sarcomere lattice consist of actin and myosin chains, respectively. Formation of cross-bridges between these myofilaments are considered the sole source of active force production in muscle, with the amount of force produced depending on the degree of overlap between the two myofilaments [6, 162]. Owing to various intricate mechanisms such as "swinging, tilting, cross-bridge sliding filament mechanism" [4, 5] within the actin–myosin cross-bridges, much has been understood regarding the production of muscle force.

Titin is considered the backbone of sarcomere [8, 163]. It spans half the sarcomere, beginning from its C-terminus located at M-line, where opposing tails of myosin filaments meet, throughout the immunoglobulin (Ig) and fibronectin super-repeats, around which myosin molecules form their thick filament structures. This is the stiff A-band titin. In skeletal muscle, the elastic I-band titin can be considered as a series of springs, which start with a distal Ig tandem, followed by a proline-glutamate-valine-lysine (PEVK) rich region including an N2A region, and a longer Ig tandem (proximal) region, finally terminating at its N-terminus along the Z-line. Overall, the intra-cellular passive tension of sarcomeres has been predominantly attributed to titin [158, 164].

On the other hand, N2A, PEVK and Ig tandems are sensitive to $[Ca^{2+}]$ transients [7]. Also, N2A region is highly susceptible to additional mechanical interaction with actin filaments upon changes in calcium concentration [9, 16, 165]. Consequently, active state titin gets stiffer compared to its passive state [10, 17, 166, 167]. Therefore, considering titin as a passive elastic component with state independent mechanical

properties is not accurate. This viewpoint stems from, or lends explanations for a key muscle mechanics phenomenon regarding the descending limb of muscle's length force characteristics i.e., the residual force enhancement (RFE). RFE characterizes a velocity-independent [168, 169, 170] excess in actively lengthened muscle's force, compared to its force encountered at the same length following passive lengthening and subsequent activation [13, 171]. This is ascribed to active state titin's higher stiffness, which remains effective also during muscle shortening [16, 17]. Accordingly, much attention was paid also to re-shortening from a long length, which preserves some RFE, whereas passively lengthened muscle returns back to same force level. Taking these into account, titin has been considered part of a three-myofilament paradigm to describe eccentric contraction of skeletal muscles [8, 172]. These important issues were most often studied in sarcomere or fiber section levels [12, 173].

However, a better understanding of the mechanism and functional consequences of such three-myofilament paradigm requires local as well as global assessments performed after placing active state titin in the context of entire muscle. Globally, effects of active state titin on muscle force have been the main focus, but how this may affect its length range of force exertion has not been studied. Locally, two important issues have not been addressed:

1. Effects of active state titin on distribution of length changes along muscle fibers, and

2. Separate contributions of actin–myosin apparatus and active state titin to force production.

In order to address these interrelated points, our aim was to implement active state titin within our linked fiber–matrix mesh model (LFMM) [24, 32] and to elaborate on the mechanism of its effects on muscle function both locally and globally.

5.2 Methodology: Linked Fiber–Matrix Mesh Finite Element Model

5.2.1 Myofiber Element

To define the active stress of the contractile elements (Figure 5.1a) hence to represent active length–force characteristics, cubic and quartic exponential partial functions (Eq. 5.1, Figure 5.2) were fit to the experimental data of small rat GM fiber bundles [174]. This function is scaled such that at L_{opt}, ϵ_{22} is zero and the maximal stress value is normalized as one. Note that force–velocity relationship for active muscle is not included in this definition.

$$\sigma_{22contr}(\epsilon_{22}) = \begin{cases} b_3 e^{b_2 \epsilon_{22}^3} & \text{if} \quad \epsilon_{22} > 0 \\ b_3 e^{b_1 \epsilon_{22}^4} & \text{if} \quad \epsilon_{22} < 0 \end{cases} \tag{5.1}$$

where b_1, b_2 and b_3 are constants (Table 5.1).

Experimental tension–sarcomere length data [158] for single rabbit skeletal muscle fibers were fit with a quadratic function (Eq. 5.2 Figure 5.3, gray triangles) which was scaled to make it compatible to stress–strain characteristics of the contractile part. Reference model incorporates passive state properties of titin (Eq. 5.1) also during active state analyses.

$$\sigma_{22titin}(\epsilon_{22}) = \begin{cases} t_1 \epsilon_{22}^2 + t_2 \epsilon_{22} + t_3 & \text{if} \quad \epsilon_{22} > 0 \\ 0 & \text{if} \quad \epsilon_{22} < 0 \end{cases} \tag{5.2}$$

where t_1, t_2 and t_3 are constants (Table 5.1).

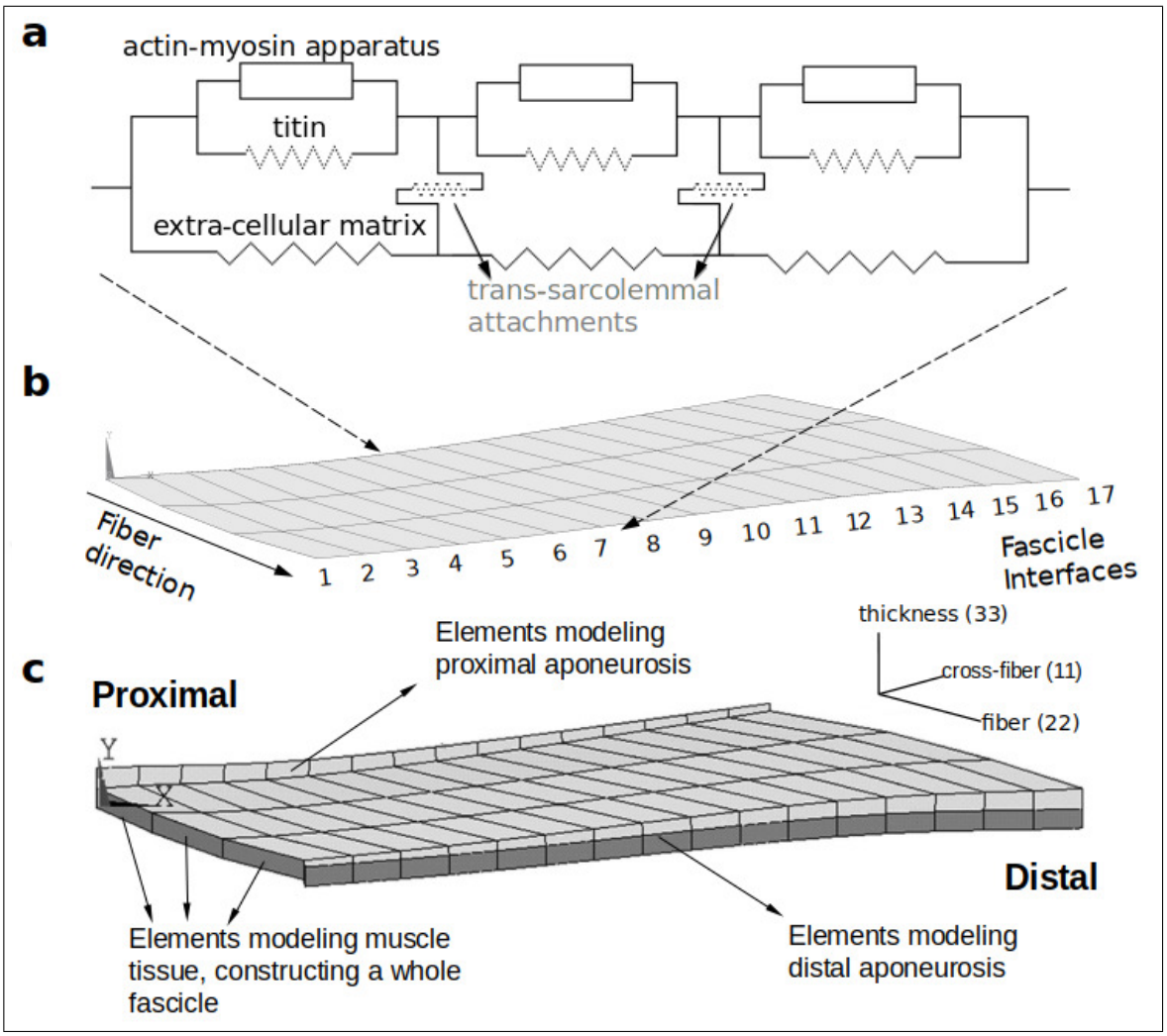

Figure 5.1 (a) Two-dimensional-schematic representation of an arrangement of muscle elements. The intra-cellular domain, which is composed of the active contractile elements (actin–myosin contractile apparatus) and intra-cellular "passive" cytoskeleton (titin), is linked to the extra-cellular matrix domain elastically through trans-sarcolemmal attachments. (b) The model consists of three muscle elements in series and sixteen in parallel. Three muscle elements arranged in series construct a whole fascicle. (c) Muscle elements located proximally and distally are connected to elements representing muscle's aponeuroses. A 3D-local coordinate system representing the fiber, cross-fiber (normal to the fiber direction), and thickness directions is used for the analysis and presentation of the model results [31]. Note that the 16 fascicle model was preferred in the final analysis of shifted titin for increased nodal resolution, whereas for other models 6 fascicle geometry suffices.

In contrast, the extended model distinguishes active state titin. To define stress–strain characteristics of titin in active state, one way is by obtaining normalized titin stresses during active lengthening beginning at initial sarcomere length of the present model. Therefore, normalized total, cross-bridge and passive forces for a sarcomere actively lenghtening from 2.4 μm initial length were acquired from Heidlauf

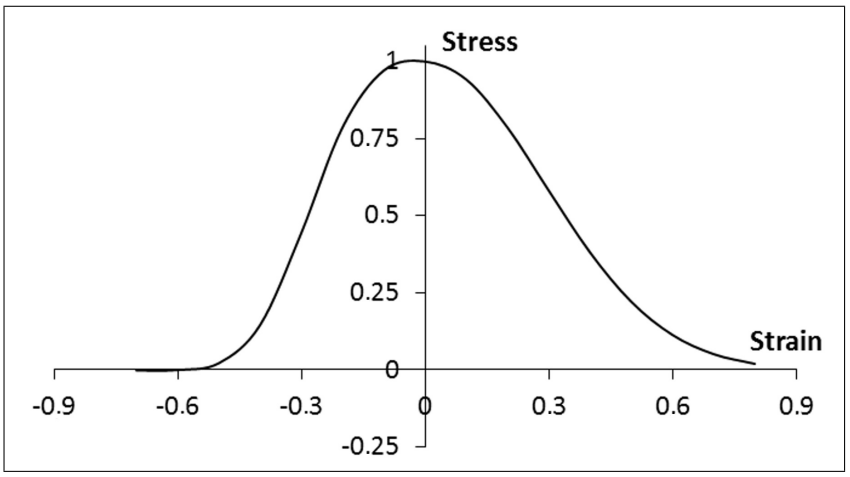

Figure 5.2 Active stress–strain properties of the myofiber element representing the contractile apparatus, which is valid only for the local fiber direction.

et al. [18] and Schappacher-Tilp et al. [1] models. Force due to active state stiffened titin is calculated by subtracting passive and cross-bridge forces from total force. A cubic function fit to resulting active state titin normalized stress data points constitutes stiffened titin's equation (Eq. D.1, Figure 5.3, black rhombi) in stiffened titin case. See Appendix D for details.

$$\sigma_{22titin}(\epsilon_{22}) = \begin{cases} h_1\epsilon_{22}^3 + h_2\epsilon_{22}^2 + h_3\epsilon_{22} & \text{if} \quad \epsilon_{22} > 0 \\ 0 & \text{if} \quad \epsilon_{22} < 0 \end{cases} \tag{5.3}$$

where h_1, h_2 and h_3 are constants (Table 5.1).

Alternatively, titin's increased affinity to bind with actin upon calcium concentration increase (i.e., activation) near its N2A region in vitro could result in reduced free spring length of titin, which was implemented into the model with a leftward (i.e., stiffer) shift in titin's constitutive equation using a titin shift coefficient ϵ_{shift} (Eq. 5.4, Figure 5.4), and assessed in shifted titin case.

Table 5.1
Values and definitions of the model constants.

Constant	Value	Definition
b_1	30.0	Coefficient for stress–strain relation of the contractile elements (Eq. 5.1)
b_2	-6.0	Coefficient for stress–strain relation of the contractile elements (Eq. 5.1)
b_3	1.0	Coefficient for stress–strain relation of the contractile elements (Eq. 5.1)
t_1	0.522	Coefficient for stress–strain relation of the intra-cellular passive elements (Eq. 5.2)
t_2	0.019	Coefficient for stress–strain relation of the intra-cellular passive elements (Eq. 5.2)
t_3	-0.002	Coefficient for stress–strain relation of the intra-cellular passive elements (Eq. 5.2)
h_1	-8.242	Coefficient for stress–strain relation for active state stiffened titin (Eq. D.1)
h_2	11.88	Coefficient for stress–strain relation for active state stiffened titin (Eq. D.1)
h_3	-0.052	Coefficient for stress–strain relation for active state stiffened titin (Eq. D.1)
k	0.05	Initial passive stiffness (Eq. 5.7)
a_{11}	8.0	Passive cross-fiber direction stiffness, $a_{11} = a_{33}$ (Eq. 5.7)
a_{22}	6.0	Passive fiber direction stiffness (Eq. 5.7)
a_{12}	6.0	Passive cross-fiber direction stiffness, $a_{12} = a_{23} = a_{31}$ (Eq. 5.7)
λ_S	5.0	Weight factor in the penalty function for the solid volume (Eq. 5.8)
λ_F	20.0	Weight factor in the penalty function for the fluid volume (Eq. 5.8)

$$\sigma_{22titin}(\epsilon_{22}) = t_1 \left(\epsilon_{22} + \epsilon_{shift}\right)^2 + t_2 \left(\epsilon_{22} + \epsilon_{shift}\right) + t_3 \tag{5.4}$$

where t_1, t_2 and t_3 are constants (Table 5.1) and ϵ_{shift} equaled a third of imposed active muscle lengthening, a ratio based on fascicle length to muscle length ratio, namely reference titin's constitutive equation is shifted by one third of the active lengthening imposed cumulatively.

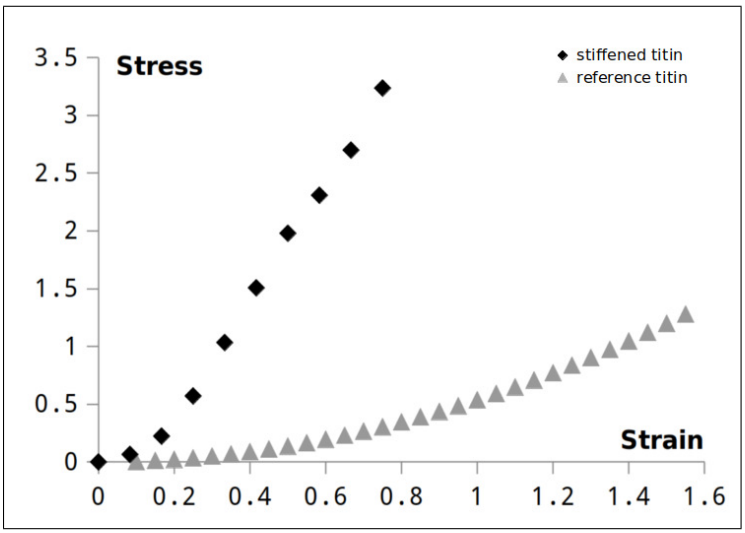

Figure 5.3 Stress–strain relation of intra-cellular titin in myofiber domain for reference passive and stiffened active states.

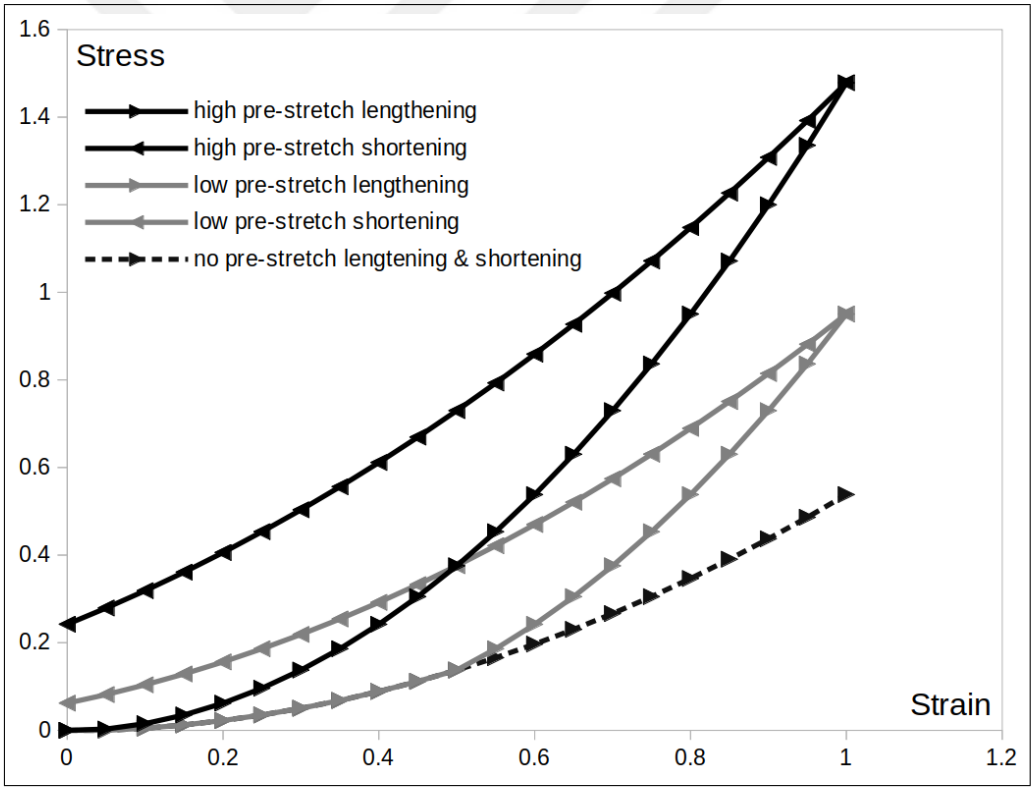

Figure 5.4 Stress–strain relation of intra-cellular titin in myofiber domain for passive and shifted active states.

5.2.2 ECM element

The ECM element represents the basal lamina and intra-muscular connective tissue components including the endomysium, perimysium and epimysium. A strain

energy density function accounts for the non-linear and anisotropic material properties, and the constancy of muscle volume.

Stress formulation, $\underline{S}$, based on second Piola–Kirchoff definition constitutes the derivative of strain energy density function, W, with respect to Green–Lagrange strain tensor, $d\underline{L}^G$:

$$\underline{S} = \frac{dW}{d\underline{L}^G} \tag{5.5}$$

Strain energy density function that mechanically characterizes the ECM consists of two parts:

$$W = W_1 + W_2 \tag{5.6}$$

The first part represents the non-linear and anisotropic material properties [159]:

$$W_1 = W_{ij}(\epsilon_{ij}) = \begin{cases} k\left[e^{a_{ij}\cdot\epsilon_{ij}} - a_{ij}\cdot\epsilon_{ij}\right] & \text{if} \quad \epsilon_{22} > 0 \\ 0 & \text{if} \quad \epsilon_{22} < 0 \;\; or \;\; i \neq j \end{cases} \tag{5.7}$$

where ϵ_{ij} are the Green–Lagrange strains in the local coordinates. Indices $i = 1\,, \ldots\,, 3$ and $j = 1\,, \ldots\,, 3$ represent local cross-fiber, fiber and thickness directions, respectively. a_{ij} and k are constants (Table 5.1). Resulting stress–strain curves are shown in Figure 4.2.

The second part includes a penalty function to account for the constancy of muscle volume:

$$W_2 = \lambda_S \left(I_3 - 1\right)^2 + \lambda_F \left(I_3^{avg} - 1\right)^2 \tag{5.8}$$

where, I_3 is the third invariant of the right Cauchy–Green strain tensor and is a measure for the local volume for each Gaussian integration point. If all the I_3s are kept as one, the element is considered as solid and the local volumes are conserved. If the weighted mean of all I_3s per element, $I_3^{avg} - 1$, is kept as one, the element is considered as a fluid. Penalty parameters λ_S (for solid volume) and λ_F (for fluid volume) (Table 5.1), allow determining the emphasis given for each part.

5.2.3 Elements linking the fiber and matrix meshes

For the elastic links between two meshes representing the trans-membranous attachments of the cytoskeleton and the ECM, COMBIN39 standard element from ANSYS 12.0 element library was used. This is a 2-node uniaxial spring element, defined separately and identically for each global direction, with linear stiffness characteristics determined according to [88].

5.2.4 Aponeurosis element

To represent the aponeuroses, HYPER58 standard element from ANSYS 12.0 element library was used. This 3D element has 8-nodes and a hyperelastic mechanical formulation for which strain energy density function is defined using Mooney–Rivlin material law.

5.2.5 Model of isolated EDL muscle

EDL muscle of the rat was modeled. This muscle has unipennate geometry with rather small pennation angles and minimal variation of the fiber direction within muscle belly. Model geometry (Figure 5.1b) is defined as the contour of a longitudinal slice at the middle of isolated rat EDL muscle belly. Three muscle elements in-series and sixteen in-parallel fill this slice. Therefore, any collection of three muscle elements

arranged in series represents a big muscle fascicle. All aponeurosis elements have identical mechanical properties but using a variable thickness in fiber–cross-fiber plane, such that aponeurosis' increasing cross-sectional areas toward their tendons are accounted for (Figure 5.1c).

5.2.6 Reference model with passive state titin vs. extended models incorporating active state titin

For all muscle models studied, in passive state, activation coefficient b_3 (Eq. 5.1) initially equaled 0. Maximal activation of muscles modeled was achieved by increasing b3 incrementally to 1, using fixed increments, while models were kept fixed at initial muscle length (28.7 mm). Note that, from here on this will be regarded as optimum length (L_{opt}). Muscle length was changed by changing the position of muscle's most distal nodes in distal direction in order to lengthen the muscle by a certain amount. Muscle's proximal end was fixed during the procedure.

5.2.6.1 Stiffened titin case.

The proximal end is fixed and distal end of muscle is displaced 3.2 mm distally to impose muscle lengthening.

5.2.6.2 Stiffened titin case with extra-muscular linkages.

Through alternating translation of the proximal and distal end nodes, muscle is displaced distally by 7 mm, while the ends of extra-muscular connections are kept mechanically grounded. Once relative position change is complete, the proximal end is fixed and distal end of muscle is displaced 3.2 mm distally to impose muscle lengthening. Elements representing the extra-muscular connections for the three proximal fascicle interfaces are four times stiffer than the remainder 4 distal fascicle interfaces (Figure 4.1a).

5.2.6.3 Shifted titin case.

Alternatively, active state shifted titin's model implementation was studied for isolated model rat EDL muscle in the following three cases:

1. No pre-stretch: reference titin constitutive equation was used, hence no activation effect on titin stress–strain characteristics in active state was accounted for.

2. Low pre-stretch: first, muscle was passively lengthened to $L_{opt} + 1$ mm, which had no effect on the shift coefficient, ϵ_{shift}; activated at this length, and was subsequently lengthened to $L_{opt} + 2$ mm using active state shifted titin case. Therefore, ϵ_{shift} remained zero for the first 1 mm and was gradually increased with imposed active muscle lengthening, equaling 1/3 at $L_{opt} + 2$ mm (Eq. 5.4).

3. High pre-stretch: muscle was activated at L_{opt}, before being lengthened to $L_{opt} + 2$ mm. Therefore, ϵ_{shift} was gradually increased with imposed active muscle lengthening, equaling 2/3 at $L_{opt} + 2$ mm (Eq. 5.4).

Note that: (i) in addition to those of the reference model, Figure 5.4 shows also the altered titin stress–strain characteristics of active state model by exemplifying the relevant curves representing $L_{opt} + 2$ mm for cases (2) and (3). (ii) During subsequent shortening, titin remains on the curve corresponding to its lengthening history attained at $L_{opt} + 2$ mm (Figure 5.4, shortening curves).

5.2.7 Solution procedure

Analysis type used in ANSYS was static and large strain effects were included. Throughout the solution procedure, studied models were stable and no mesh refinement was performed. A force-based convergence criterion was used with a tolerance of 0.5%.

5.2.8 Processing of data

Muscle length–force data were studied to quantify changes in total muscle force. All forces were normalized to total force at L_{opt} of reference model ($F_{ref}@L_{opt}$). Mean fiber direction nodal strain and nodal stresses (total, contractile apparatus, and titin stresses separately) along the fascicle interfaces were calculated for high vs. no pre-stretch cases at $L_{opt} + 2$ mm and back at L_{opt}. Coefficient of variation (CV) for mean fiber direction nodal strains defined as the ratio of the standard deviation to the mean was calculated as an indicator of parallel sarcomere length heterogeneity. Areas under mean fiber direction nodal stress–fascicle interface curves were calculated to quantify changes in total, contractile and titin stresses in order to assess their relative contributions to muscle's force production.

5.3 Results

5.3.1 Global: Effects of active state titin on muscle length–force

5.3.1.1 Stiffened titin case.

Figure 5.5 shows no shift in muscle optimum length.

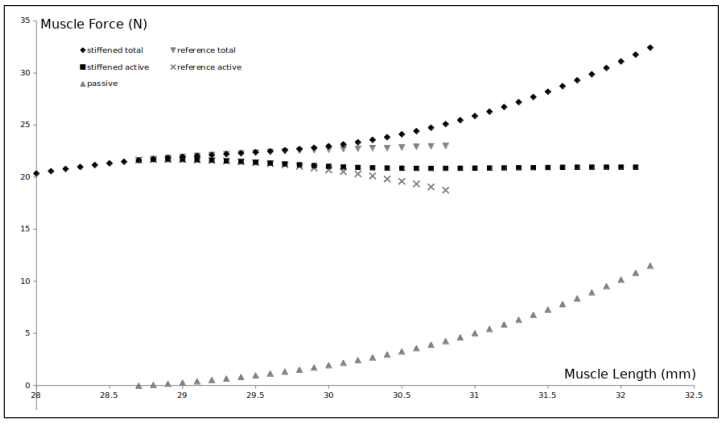

Figure 5.5 Active muscle force decreases beyond optimum length with no apparent shift in muscle optimum length for stiffened titin case.

5.3.1.2 Stiffened titin case with extra-muscular linkages.

Figure 5.6 shows no shift in muscle optimum length.

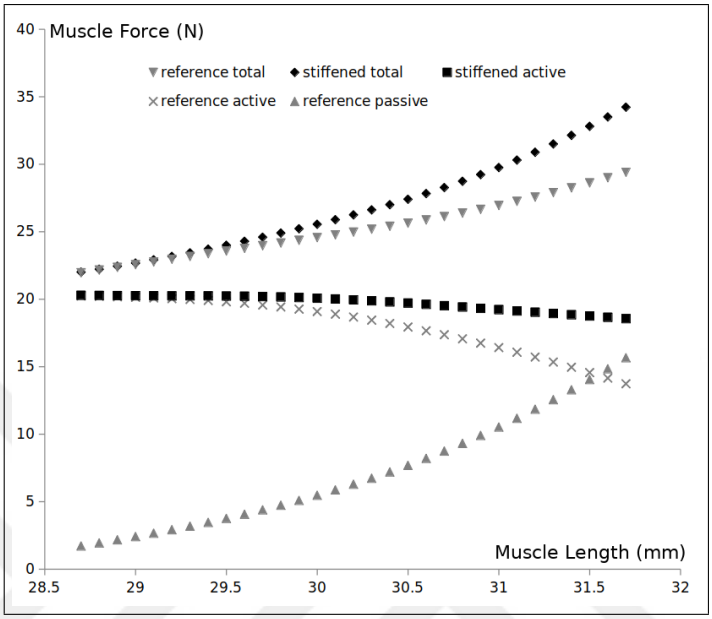

Figure 5.6 Muscle length vs total, active, and passive force results for reference and stiffened titin in muscle relative position change models.

5.3.1.3 Shifted titin case.

Figure 5.7 shows muscle length–total force characteristics for the reference and two shifted titin cases studied. The two panels allow assessing effects of active state shifted titin on muscle force during muscle lengthening (Figure 5.7a) and subsequent muscle shortening (Figure 5.7b).

For the extended model, Figure 5.7a indicates that active state shifted titin leads to elevated muscle forces calculated for all muscle lengths studied. Note that compared to no pre-stretch case, force increase rate per 1 mm muscle length increment in pre-stretched cases is not the same, but increases: for L_{opt} to $L_{opt} + 1$ mm, high pre-stretch case yields 4.8%; whereas for $L_{opt} + 1$ to $L_{opt} + 2$ mm, low pre-stretch case yields 7.8% and high pre-stretch yields 24.6% increase in total muscle force. Remarkably, the

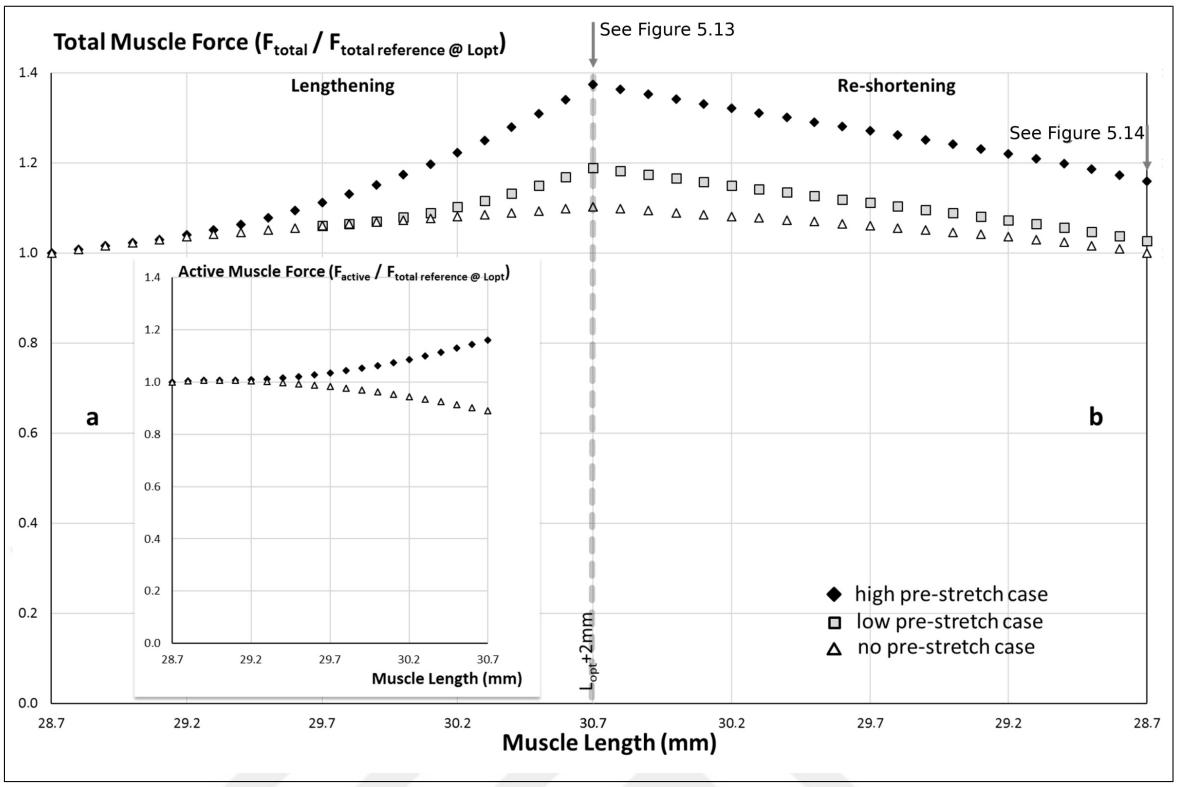

Figure 5.7 Total force–length characteristics of modeled EDL muscles in the range of muscle lengths studied, L_{opt} and $L_{opt}+2$ mm. Total isometric muscle forces of different model cases are normalized to the maximum of that in reference model (no pre-stretch case) at optimum length ($F_{ref}@L_{opt}$). In high pre-stretch (diamonds), low pre-stretch (squares) and no pre-stretch (triangles) cases, muscle is fully activated at L_{opt}, $L_{opt}+1$ mm and $Lopt+2mmrespectively.Subsequently, musclesareactivelylengthenedto L_{opt}+2$ mm and shifts are employed in titin's constitutive relation corresponding to the case studied (Figure 5.3). The shift employed in the lengthening half of the protocol (left) was kept effectual in the shortening half (right). (a) Total force increases with increasing muscle length in all cases, however disproportionately. High pre-stretch case yields most force increase per active lengthening, especially so in the second millimeter of the studied range. Inset: Active muscle force–length characteristics for no pre-stretch and high pre-stretch case muscles. Note that the initial length is the optimum length for the reference model, with active forces decreasing at longer lengths. It is also of note that the high pre-stretch case muscle's active force increases monotonously.

muscle length–active force characteristics (Figure 5.7a inset) shows that elevated muscle force is not the sole effect of active state shifted titin. By definition, no pre-stretch case attains its maximum active force at Lopt and decreases thereon. In contrast, high pre-stretch case shows that active force keeps increasing, indicating that its muscle optimum length shifts to a longer length (beyond 30.7 mm). Figure 5.7b shows that shortening from $L_{opt}+2$ mm, much of the differences in total muscle force between high and no pre-stretch cases persists even back at L_{opt} (16.0%). Also, low pre-stretch case shows such RFE (2.6%) compared to no pre-stretch case.

5.3.2 Local: mechanism of RFE based on muscle fiber direction strains and stresses

5.3.2.1 Stiffened titin case local strain and stresses.

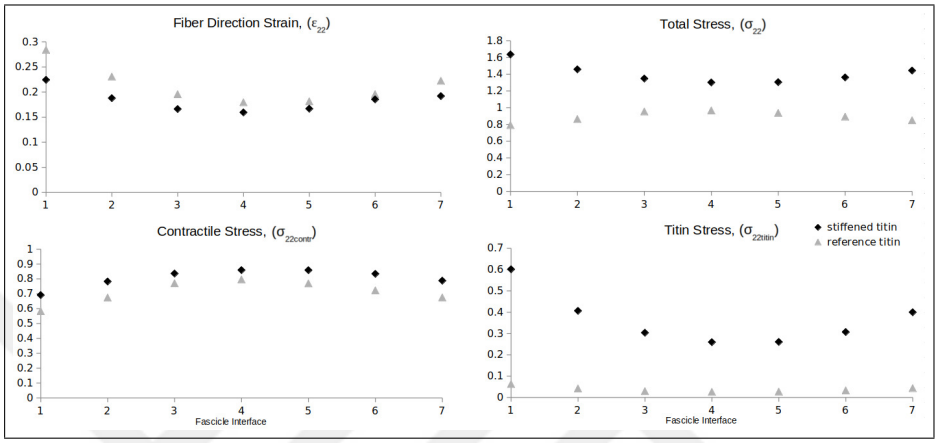

Figure 5.8 Mean nodal fiber direction strain/stresses vs. fascicle interface curves at long ($L_{opt} + 3.2$ mm) muscle length. (a) Mean fiber direction strain, ϵ_{22}, per fascicles indicates restricted lengthening in stiffened active state titin case (black diamonds), compared to reference passive titin case (gray triangles). CV of strains dropped from 17.3% to 12.0%, however heterogeneity remained substantial. (b) Mean fiber direction total stress, σ_{22}, across fascicles for reference and stiff titin cases. Area under the curves ($\Sigma\,\sigma_{22}$) indicates increased active force production capacity of muscle, which is increased by 57.5% for stiffened titin case. (c) Mean nodal fiber direction contractile stress, $\sigma_{22contr}$, across fascicle interfaces. Contribution of contractile apparatus to active force production increased by 13.2% for stiffened titin case. (d) Mean nodal fiber direction titin stress, $\sigma_{22titin}$. Titin took part in active force production.

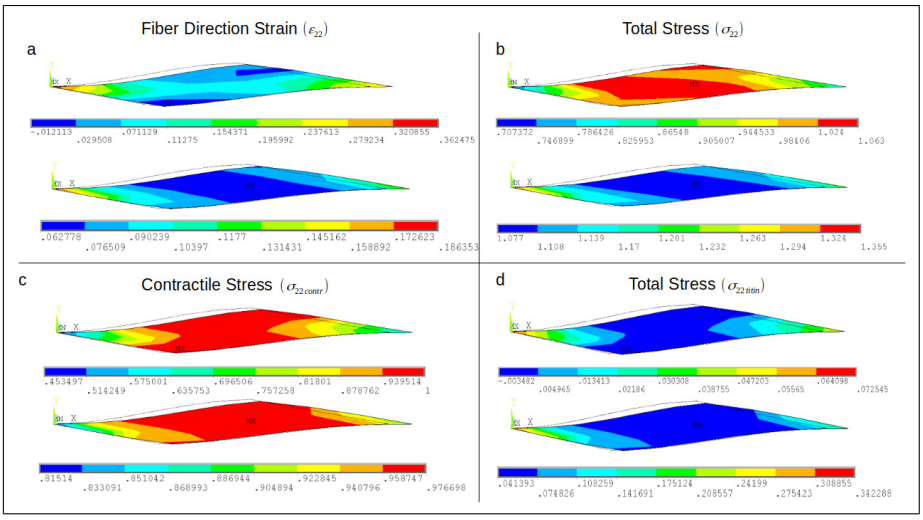

Figure 5.9 Contour plots of reference titin (top plots) and stiffened titin (bottom plots) cases showing (a) fiber direction strain (ϵ_{22}), (b) total fiber direction stress (σ_{22}), (c) stress due to actin–myosin contractile apparatus ($\sigma_{22contr}$), (d) stress due to titin ($\sigma_{22titin}$).

5.3.2.2 Stiffened titin relative position change case local strain and stresses.

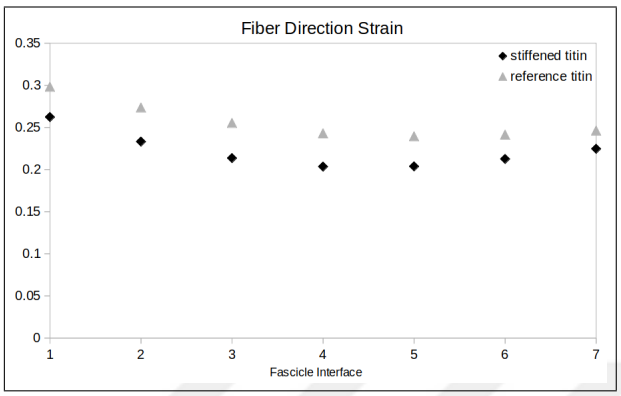

Figure 5.10 Nodal fiber direction strain per fascicle interface for stiffened and reference titin cases in active lengthening after muscle relative position change.

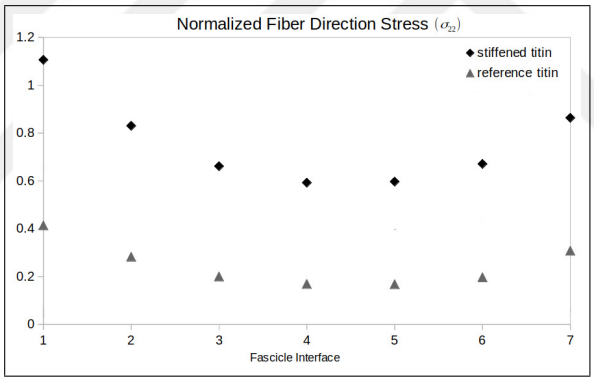

Figure 5.11 Nodal fiber direction total stress per fascicle interface for stiffened and reference titin cases in active lengthening after muscle relative position change.

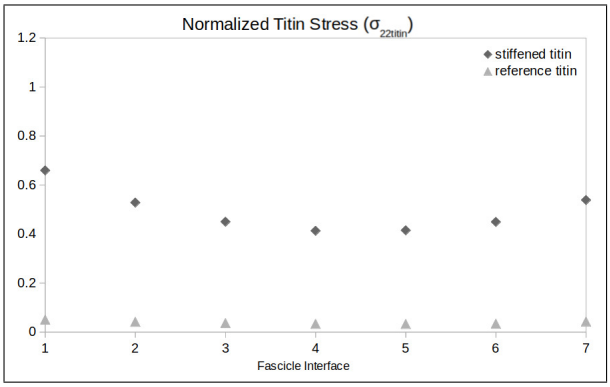

Figure 5.12 Nodal fiber direction titin stress per fascicle interface for stiffened and reference titin cases in active lengthening after muscle relative position change.

5.3.2.3 Shifted titin case local strains and stresses.

Figure 5.13 shows relevant muscle mechanics metrics at $L_{opt} + 2$ mm in order to assess the mechanism of RFE (Figure 5.13a) by comparing no pre-stretch vs. high pre-stretch cases:

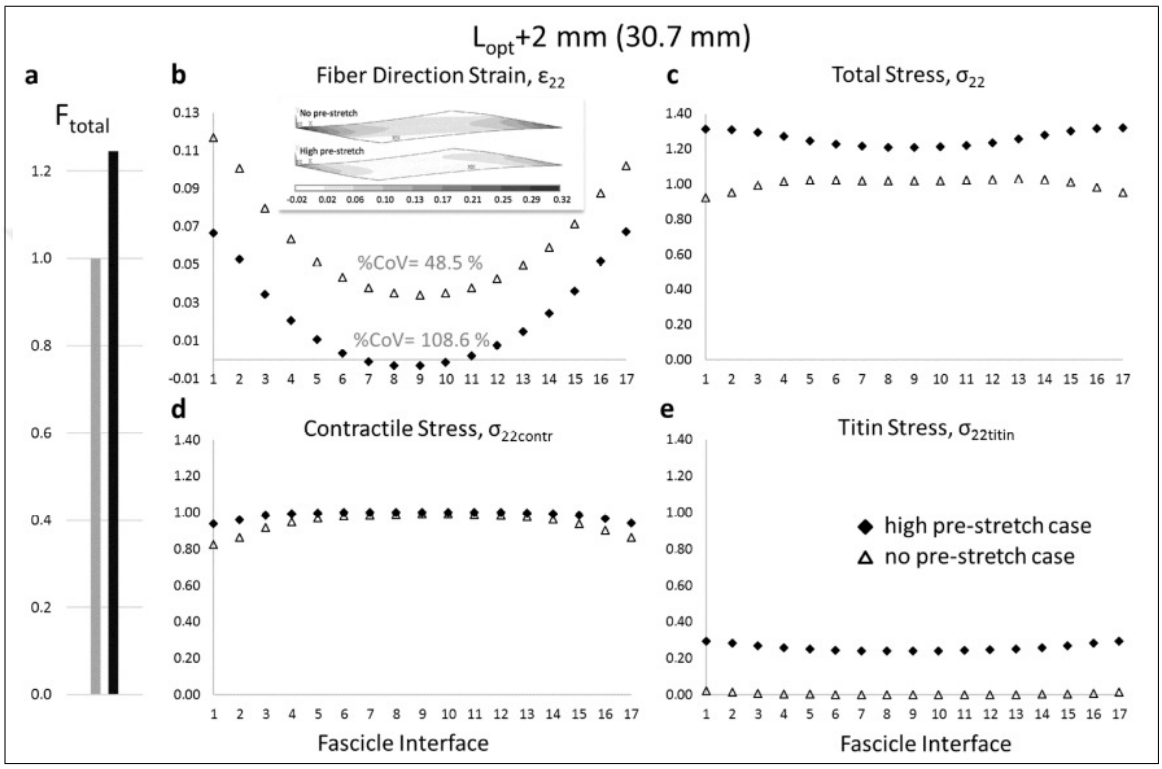

Figure 5.13 Total muscle force and mean fiber direction nodal strain/stresses vs. fascicle interface curves at long ($L_{opt} + 2$ mm) muscle length. (a) Total muscle force for no pre-stretch (gray bar) and high pre-stretch (black bar) cases. (b) Mean fiber direction strain, ϵ_{22}, across fascicles indicates increased shortening in high pre-stretch case (diamonds), compared to no pre-stretch case (triangles). A decrease in CV of strains was observed, however heterogeneity remained substantial. Inset: Fiber direction nodal strains at long muscle length. MN (minimum) and MX (maximum) denote the extrema for shortening and lengthening, respectively. X and Y axes form cross-fiber plane and $X \otimes Y$ gives the local fiber direction. (c) Mean fiber direction total stress, σ_{22}, across fascicles for no pre-stretch and high pre-stretch cases. Area under the curves ($\Sigma \sigma_{22}$) indicates increased active force production capacity of muscle. Inset: Contour strain plots at long muscle length. (d) Mean fiber direction nodal contractile stress, ($\sigma_{22contr}$), across fascicle interfaces. Contribution of contractile apparatus to active force production decreased for high pre-stretch case. (e) Mean fiber direction nodal titin stress, $\sigma_{22titin}$. Titin took part in active force production.

Effects on sarcomere lengths at $L_{opt} + 2$ mm: CV for mean fascicle interface nodal strains were calculated to be 48.5% and 108.6% for no pre-stretch and high pre-stretch cases, respectively (Figure 5.13b). This indicates that high pre-stretch case

leads to elevated parallel sarcomere length heterogeneity. However, the nature of the sarcomere length distribution is not only variable across fascicle interfaces, but is also remarkable. Overall, high pre-stretch case shows much less sarcomere lengthening (for proximal fascicle interfaces 1–6 and for distal fascicle interfaces 12–17; by up to 42.9% for fascicle interface 1). Notably, for middle fascicle interfaces (7–11) even sarcomere shortening was found (up to 3.1% for fascicle interface 9 in high pre-stretch case, whereas the same fascicle interface shows 3.4% lengthening in no pre-stretch case), although the muscle is lengthened. Contour plots (Figure 5.13b inset) i.e., a representation of all fiber direction nodal strains indicate that in agreement with the muscle's increased length, the tendon ends of the most distal and proximal fascicle interfaces show elongation. However, for high pre- stretch case sarcomeres are restricted from lengthening in entire middle part of the muscle. Therefore, the characteristic effect of shifted active state titin is a shorter sarcomere effect.

Effects on force production at $L_{opt} + 2$ mm: Area under total stress curve increased by 24.8% (Figure 5.13c), which is in concert with the elevated muscle force. This overall effect however, is not uniform across different fascicle interfaces. In high pre-stretch case, mean fascicle interface total stress is greater by 28.4% for proximal and distal, and by 19.3% for middle fascicle interfaces. A remarkable finding is that for high pre-stretch case, contribution of the contractile apparatus to muscle force production is limited (area under contractile stress curve increased only by 3.7%) (Figure 5.13d). In contrast, titin stresses are high (Figure 5.13e). Therefore, the difference in total stress is ascribed predominantly to shifted active state titin. This shows that shifted active state titin plays the dominant role in the elevated muscle forces.

Figure 5.14 shows relevant muscle mechanics metrics back at L_{opt} in order to assess mechanisms of RFE (Figure 5.14a) by comparing no pre-stretch vs. high pre-stretch cases:

Effects on sarcomere lengths back at L_{opt}: CV for mean fascicle interface nodal strains were calculated to be 15.5% and 14.9% for no pre-stretch and high pre-stretch cases, respectively (Figure 5.14b). This indicates that high pre-stretch case leads to

somewhat reduced parallel sarcomere length heterogeneity, back at L_{opt}. However, more importantly, high pre-stretch case shows more pronounced sarcomere shortening (e.g., by 14.5% for fascicle interface 7). This sustains the characteristic shorter sarcomere effect.

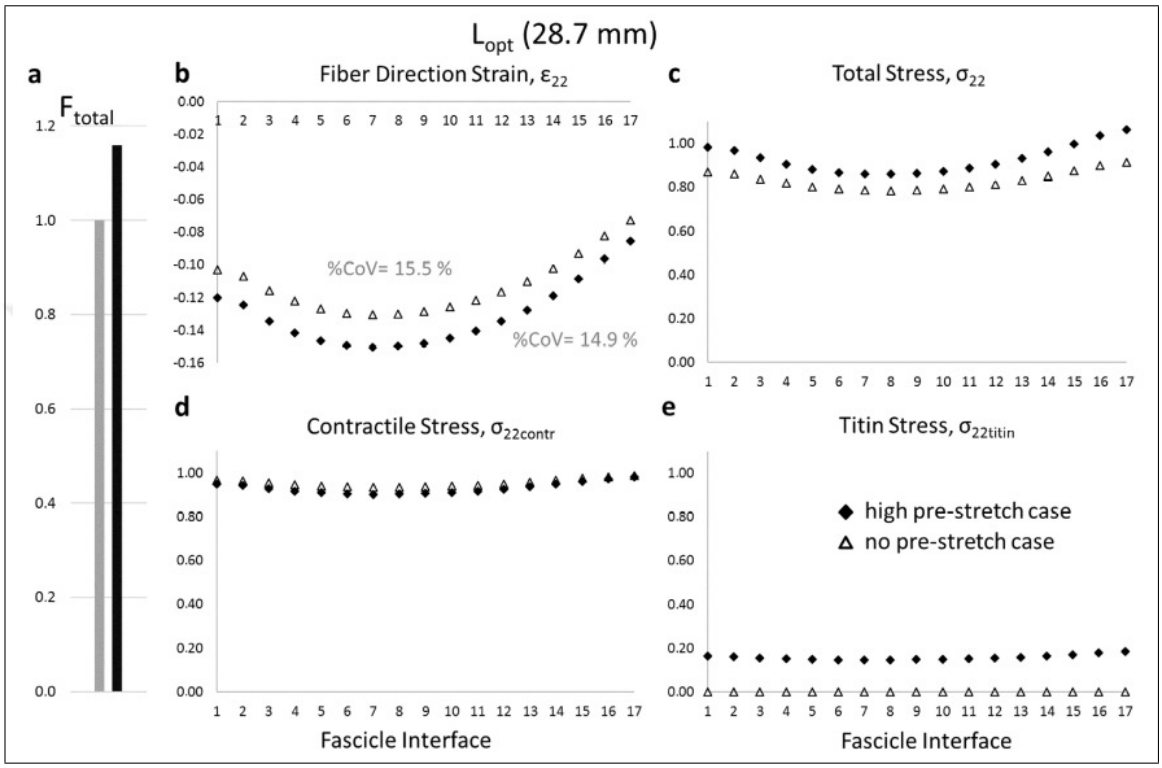

Figure 5.14 Total muscle force and mean fiber direction nodal strain/stresses vs. fascicle interface curves back at original (L_{opt}) muscle length. (a) Total muscle force for no pre-stretch (gray bar) and high pre-stretch (black bar) cases. (b) Mean fiber direction strain, ϵ_{22}, across fascicles indicates increased shortening in high pre-stretch case (diamonds), compared to no pre-stretch case (triangles). A decrease in CV of strains was observed, however heterogeneity remained substantial. Inset: Fiber direction nodal strains at long muscle length. MN (minimum) and MX (maximum) denote the extrema for shortening and lengthening, respectively. X and Y axes form cross-fiber plane and $X \otimes Y$ gives the local fiber direction. (c) Mean fiber direction total stress, σ_{22}, across fascicles for no pre-stretch and high pre-stretch cases. Area under the curves ($\Sigma\,\sigma_{22}$) indicates increased active force production capacity of muscle. Inset: Contour strain plots at long muscle length. (d) Mean fiber direction nodal contractile stress, ($\sigma_{22contr}$), across fascicle interfaces. Contribution of contractile apparatus to active force production decreased for high pre-stretch case. (e) Mean fiber direction nodal titin stress, $\sigma_{22titin}$. Titin took part in active force production.

Effects on force production back at L_{opt}: Area under the total stress curve did increase (by 11.6%) (Figure 5.14c) in concert with the elevated muscle force. Remarkably, despite that, the contribution of the contractile apparatus to active force production is reduced (area under contractile stress curve decreased by 2.5%) for high pre-stretch

case (Figure 5.14d). Therefore, RFE is actually compromised by the contractile apparatus. In contrast, the high pre-stretch case shows high titin stresses (Figure 5.14e) indicating that active state titin's dominant role in elevated muscle forces for muscle lengthening becomes the exclusive mechanism after muscle re-shortening.

5.4 Discussion

Present study showed following major effects of active state titin on muscle mechanics: Muscle lengthening assessment indicates unique, previously unconsidered effects. Globally, muscle's optimum length shifts to a longer length only for active state shifted titin case. Locally, characteristic effect of active state titin is shorter sarcomere effect in both stiffened and shifted titin case representations. Sarcomere length heterogeneity across different muscle fascicles increases. Muscle re-shortening assessment confirms the well-known persisting RFE effect. However, distinguishing the contributions of contractile apparatus and titin on muscle's force development capacity indicates that active state titin not only plays prominent role during muscle lengthening, but can be source of elevated force for muscle re-shortening as seen in the case of shifted titin. Shorter sarcomere effect leads to somewhat increased contractile apparatus force production for muscle lengthening but does cause a reduced force production for muscle re-shortening.

Present modeling indicates major functional implications of active state titin via shorter sarcomere effect. For muscle lengthening this keeps the contractile apparatus closer to optimum length, leading to greater contractile force production. However, by distinguishing their relative contributions the model representation demonstrates that main role in muscle's elevated force at the tendon is played by increased titin stress ascribed to imposed shift in its constitutive properties. Yet, what present modeling remarkably indicates is that the well-known muscle force increase is not the only outcome, but active state shifted titin also leads to a shift in optimum length of lengthening muscle to a longer length. Elevated parallel sarcomere length heterogeneity shown for high pre-stretch case can explain this change in muscle's length–force characteristics. This

was shown earlier experimentally to affect muscle's optimum length and previous modeling coupled with animal experiments also related such shift to elevated heterogeneity of mean fiber direction strains of different fascicle interfaces. Consequently, present modeling representation shows that active state titin alters the lengths at which sarcomeres function, effects of which change muscle's contribution to joint mechanics, making it a motor effective for a much wider joint range of motion. This is highly relevant for musculoskeletal disorders in which the pathological condition is limited joint mobility, such as cerebral palsy. Spastic muscle's one typical property is considered to be a shift of its optimum force to shorter muscle lengths. Present findings suggest that lacking or limited effectiveness of active state titin may be a cause for spastic muscle's early production of high forces in flexed joint positions, and an unfavorable mechanics remaining for extended joint positions. This needs to be studied.

Along with such major functional relevance of active state titin characterized, present study initiates a philosophical discussion about muscular mechanics. As an integral part of the three-filament paradigm, and locally at sarcomere level, active state titin affects the length determining the other two myofilaments' force production capability. Present modeling indicates that this effect characteristically is a lengthening restriction. Within the context of entire muscle however, results show that this is not a uniform effect either within a fascicle or across the muscle. What causes this length restriction and its variability across the muscle is the muscle fiber–ECM mechanical interaction, thus myofascial force transmission (MFT) . Myotendinous junctions provide connections of muscle fibers at their ends to ECM and are specialized for transmission of developed force to the aponeurosis and from there to muscle's tendon. However, myofiber cytoskeleton and trans-sarcolemmal connections to the basal lamina are also involved in connections of muscle fibers to ECM, but peripherally, along their full lengths. These molecular structures can be considered in four essential categories:

1. Proteins belonging to the cytoskeleton proper,
2. Cytoskeletal proteins associated to intra-cellular sarcolemma,
3. Proteins associated to extra-cellular sarcolemma, and

4. ECM proteins.

Costameres, sub-sarcolemmal proteins appearing rib-like stripes in the level of Z-discs were considered to anchor the peri-sarcomeric cytoskeleton of peripheral myofibrils to the basal lamina and ECM. Connections between Z-discs of peripheral myofibrils and sarcolemma were revealed using electron microscopy and their role in force transmission was shown in muscle fiber preparations and in whole muscle level. Note that, peripheral myofibrils are connected to internal myofibrils within the muscle fiber. Consequently, length of a sarcomere cannot be determined by its interaction with sarcomeres arranged in series with it in the same muscle fiber exclusively. Instead, the force balance determining the length of a sarcomere is much more involved and includes myofascial loads i.e., forces exerted on it by ECM, as well as forces components from sarcomeres located in neighboring muscle fibers. Previous modeling using the reference LFMM model showed that such muscle fiber–ECM mechanical interactions affect muscular mechanics substantially such that changes imposed by manipulating stiffness of connections between them or by creating a discontinuity within ECM affect lengths, hence mechanical contributions of sarcomeres to muscle's length force curves. Strain distributions along muscle fibers, often involving non-uniformities locally, manipulate force production and length range of force exertion of the muscle globally. Therefore, muscle fiber–ECM mechanical interactions have major functional significance, relevant for also present modeling.

Recent simulation of muscle exposed to botulinum toxin indicated a remarkable effect referred to as longer sarcomere effect: as a consequence of partial muscle paralyzation, muscle fiber–ECM mechanical interactions were shown to restrict sarcomere shortening within botulinum toxin treated muscle. Although using the extended LFMM model to incorporate active state titin, the specific effect shown in present modeling is the opposite, influence of muscle fiber–ECM mechanical interactions on muscular mechanics is analogous. Shorter sarcomere effect shown in this study therefore not only characterizes the central mechanism of active state titin's effects, but also indicates that the three-myofilament paradigm and MFT mechanism must interact: myofascial

loads manipulate outcome of the three-myofilament paradigm. Therefore, a suggestion to improve our understanding of fundamental muscle mechanics is the following: Despite the fact that trans-sarcolemmal connections are multi-molecular structures and no finding is available showing their calcium dependency, they, as a lumped element, may be considered as a fourth component, which interferes with and determines the output of the three calcium-dependent myofilaments. In this suggestion, integrity of trans-sarcolemmal connections is a tenable variation based on Duchenne and Becker types of muscular dystrophy. Inability to synthesize a sarcolemma-associated cytoskeletal protein in this structure, i.e., dystrophin, leads to these severe muscular diseases. Therefore, present modeling of isolated muscle indicates that via trans-sarcolemmal connections, MFT plays an important role in how active state titin affects muscular mechanics. Note that, MFT effects have been shown to be much more pronounced beyond single isolated muscle level as myofascial loads then involve also forces exerted onto muscle belly by other muscles or connective tissues. Previously, modeling conditions representative of muscle's mechanical interactions with its surroundings showed that strain distribution along muscle fibers can be non-uniform such that shortened and lengthened segments can be present along the same fascicles. Such muscle fiber strain heterogeneity was revealed also in human medial gastrocnemius muscle in vivo, after imposing passive knee movement and sustained sub-maximal contractions using magnetic resonance imaging analyses. Those findings suggest that the three-myofilament paradigm and MFT interaction may become even more important for conditions representing in vivo function. This needs to be studied in new modeling analyses.

In conclusion, the present modeling indicates that the characteristic effect of active state titin is the shorter sarcomere effect, which globally causes muscle's optimum length to shift to a longer length and locally causes sarcomeres to produce more force predominantly or exclusively by the contribution of titin. Consequently, for eccentric contraction, active state titin keeps the contractile apparatus at lengths favorable for active force production. This prevents the muscle from being exhausted at long lengths, which is relevant for pathologies involving limited joint extensibility such as cerebral palsy. Present modeling also indicates a determining role of muscle fiber–ECM mechanical interactions on this characteristic mechanism of effects of active state titin.

6. GENERAL DISCUSSION

6.1 Continuity and Integrity of Fascial Networks within Human Lower Limb

Myofascial connectivity and its relation to external loading, joint angle configuration and muscle activity have been assessed in vivo using diffusion tensor and magnetic resonance imaging analyses combined and also computationally using finite element modeling.

6.2 Use of Advanced MRI and DTI Analyses Methodologies for the Assessment of Deformations in Human Limb

Quantification of local muscle deformation and architecture using MRI and DTI is a multi-scaled problem:

1. MRI compatible devices are utilized for recording physiological data such as joint angle change or joint torque while experimental activity including muscle contraction or joint angle change is performed. These devices are designed and manufactured keeping the experiment in mind: For good cyclic data acquisition, out of plane motion should be minimized, and for reliable registration results adequate and repeatable fixation of body is a must. Additionally, care must be taken to avoid unintended tissue deformations due to fixation apparatus near area of interest. Determination of muscle activity using EMG is also an important issue to address (as inquired by Prof. Dr. Ahmet Usta in BIYOMUT 2015), whether to establish passive state or to ensure steady muscle activity throughout image acquisition. While we did have MRI-compatible EMG (i.e., no artifacts caused in the acquired MRI data), noise on EMG electrodes during MR data acquisition

far suppressed the signal, thus use of EMG was limited to assessment during volunteers' protocol orientation in the lab, where a non-MRI compatible fixation device was present to produce joint angle configuration and allow measurement of isometric plantar-flexion torque level identical to the MRI-compatible fixation device.

2. MR image data sets are acquired using modalities and imaging sequences available and suitable for the experimental scenario. For T1-weighted anatomical images, field of view must be preserved by duplicating sequences during acquisition to make sure they cover the same space within scanner's bore in order to limit effects of B0 and B1 field inhomogeneities. Also, entire tissue between coils should be imaged with appropriate phase encoding direction to avoid folding artifacts and use of 3D sequences that allow homogeneous data acquisition over volume of interest over time. For DTI, data are acquired in maximum number of directions with some signal averaging for improved signal-to-noise ratio, also keeping a suitable b-value keeping targeted tissues in mind. For PC, available modality limited data acquisition to 2D plane, and available DTI sequences were also planar. While triggered DTI acquisition was performed in same session with PC, only voxel diffusivity based fiber direction could be determined due to planar sequence and covering entire volume with thin enough slices for reliable tractography required unsustainable acquisition time. However, as 3D PC and DTI sequences become available, ability to assess muscle mechanics during cyclic motion are expected to improve.

3. Acquired data are post-processed and analyzed using the appropriate image processing tools. For reliable registration, minimum gross change in location of limb within image, minimum interpolation, and minimum transformation, which could all induce synthetic results, must be maintained. For robust tractography, absence of which causes "spotty" strain patterns on muscle fibers due to rapid changes in fiber curvature (as pointed out by Prof. Dr. Robert Herbert in ISEK 2014), suppression of Rician noise to eliminate vibration artifacts is a must. Alignment of tractography and deformation tensor spaces (i.e., DTI and anatomical image data sets) must be done with utmost care to avoid misleading

results.

Magnetic resonance imaging, and subsequent image registration and analyses allowed quantification of principal tissue deformations upon externally applied mechanical load. Diffusion tensor imaging, and subsequent tractography combined these techniques allowed determination of muscle fascicle direction strains upon single passive knee extension and during sustained sub-maximal plantar-flexion activity. Principal and shear strains of non-muscular structures including aponeuroses and neuro-vascular tracts have been quantified and related with muscle fascicle strains. While these technical improvements provide fresh insight into anatomy and mechanics of muscle, validation of demons registration algorithm using a deformable phantom is called for [155] and are to be done following present thesis. Yet, porcine phantoms with MR translucent gold markers have been imaged with MR and multi-planar X-rays separately, for undeformed and deformed states, and related data have been made available only very recently [175, 176, 177]. While these images or similar phantom assessments could indeed provide a good candidate for assessment of the demons algorithm used presently and understanding its capabilities further in quantifying local deformations, use of synthetic deformable phantoms is also a viable option. Nonetheless, further in vivo assessments in human lower limb, and also in upper limb, where issues revolving around shared tendon of triceps suræ are circumvented, providing evidence in support of myofascial loads acting on muscle [178], are underway.

APPENDIX A. DISTRIBUTION OF PRINCIPAL STRAINS IN LOWER LEG AFTER KINESIO TAPE APPLICATION

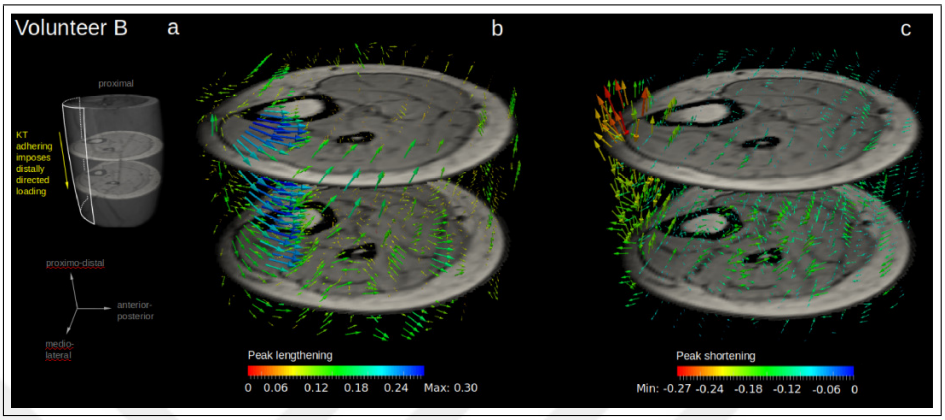

Figure A.1 Distributions of local tissue deformations due to KT application per volunteer. Deformation fields belong to Volunteer B. Deformation fields are visualized using glyphs. Each glyph represents deformation of a voxel. However, for clarity of presentation, glyphs have been masked uniformly. Direction of each glyph is determined by the corresponding eigenvector. Length of each glyph is proportional to size of local tissue lengthening or shortening. (a) Representation of KT applied zone within imaged volume. Two anatomical image slices are shown for reference. These slices, also shown in parts (b) and (c) are proximally and distally 20 slices away from the centrally located slide within analyzed volume. Superior–inferior (representing tape direction), anterior–posterior and medio–lateral directions are indicated. Deformations fields are shown distinguishing (b) local tissue lengthening and (c) local tissue shortening (first and third principal strains, respectively).

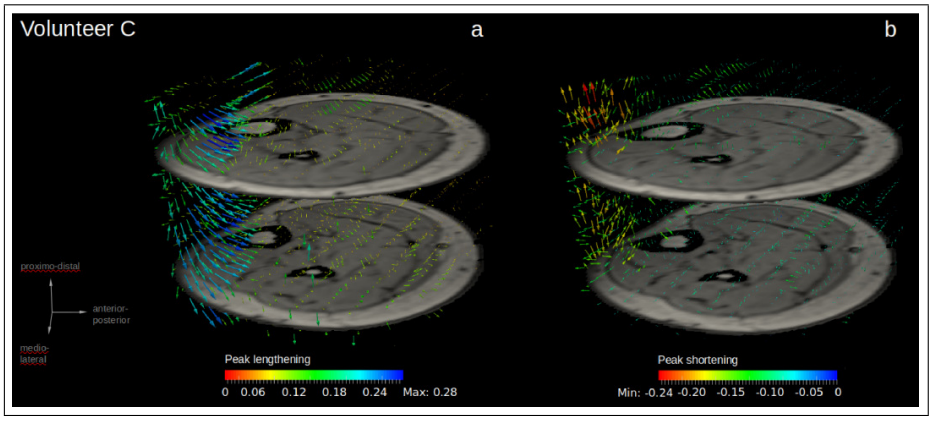

Figure A.2 Distributions of local tissue deformations due to KT application per volunteer. Deformation fields belong to Volunteer C. Deformation fields are visualized using glyphs. Each glyph represents deformation of a voxel. However, for clarity of presentation, glyphs have been masked uniformly. Direction of each glyph is determined by the corresponding eigenvector. Length of each glyph is proportional to size of local tissue lengthening or shortening. (a) Representation of KT applied zone within imaged volume. Two anatomical image slices are shown for reference. These slices, also shown in parts (b) and (c) are proximally and distally 20 slices away from the centrally located slide within analyzed volume. Superior–inferior (representing tape direction), anterior–posterior and medio–lateral directions are indicated. Deformations fields are shown distinguishing (b) local tissue lengthening and (c) local tissue shortening (first and third principal strains, respectively).

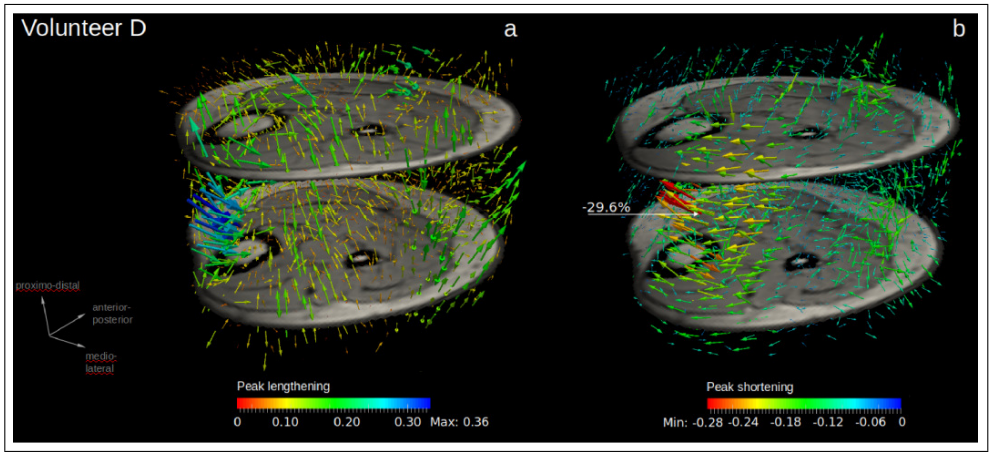

Figure A.3 Distributions of local tissue deformations due to KT application per volunteer. Deformation fields belong to Volunteer D. Deformation fields are visualized using glyphs. Each glyph represents deformation of a voxel. However, for clarity of presentation, glyphs have been masked uniformly. Direction of each glyph is determined by the corresponding eigenvector. Length of each glyph is proportional to size of local tissue lengthening or shortening. (a) Representation of KT applied zone within imaged volume. Two anatomical image slices are shown for reference. These slices, also shown in parts (b) and (c) are proximally and distally 20 slices away from the centrally located slide within analyzed volume. Superior–inferior (representing tape direction), anterior–posterior and medio–lateral directions are indicated. Deformations fields are shown distinguishing (b) local tissue lengthening and (c) local tissue shortening (first and third principal strains, respectively). Note that the strain range in panel (b) was adjusted to show local tissue shortening values of a majority of voxels clearly, and accordingly maximal strain value (29.6%) is shown separately.

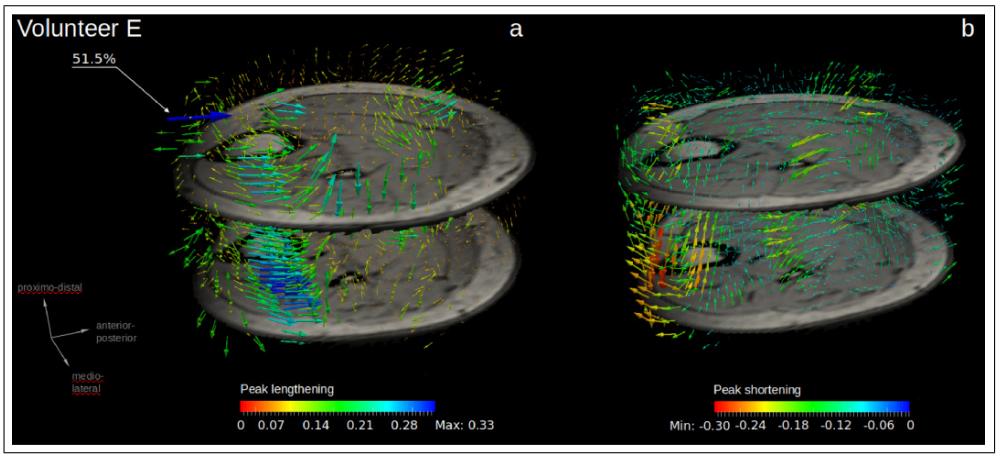

Figure A.4 Distributions of local tissue deformations due to KT application per volunteer. Deformation fields belong to Volunteer E. Deformation fields are visualized using glyphs. Each glyph represents deformation of a voxel. However, for clarity of presentation, glyphs have been masked uniformly. Direction of each glyph is determined by the corresponding eigenvector. Length of each glyph is proportional to size of local tissue lengthening or shortening. (a) Representation of KT applied zone within imaged volume. Two anatomical image slices are shown for reference. These slices, also shown in parts (b) and (c) are proximally and distally 20 slices away from the centrally located slide within analyzed volume. Superior–inferior (representing tape direction), anterior–posterior and medio–lateral directions are indicated. Deformations fields are shown distinguishing (b) local tissue lengthening and (c) local tissue shortening (first and third principal strains, respectively). Note that the strain range in panel (b) was adjusted to show local tissue shortening values of a majority of voxels clearly, and accordingly maximal strain value (51.5%) is shown separately.

APPENDIX B. MAGNETIC RESONANCE AND DIFFUSION TENSOR IMAGING FOR ASSESSMENT OF VOLUNTARY SUB-MAXIMAL ISOMETRIC PLANTAR-FLEXION IN VIVO

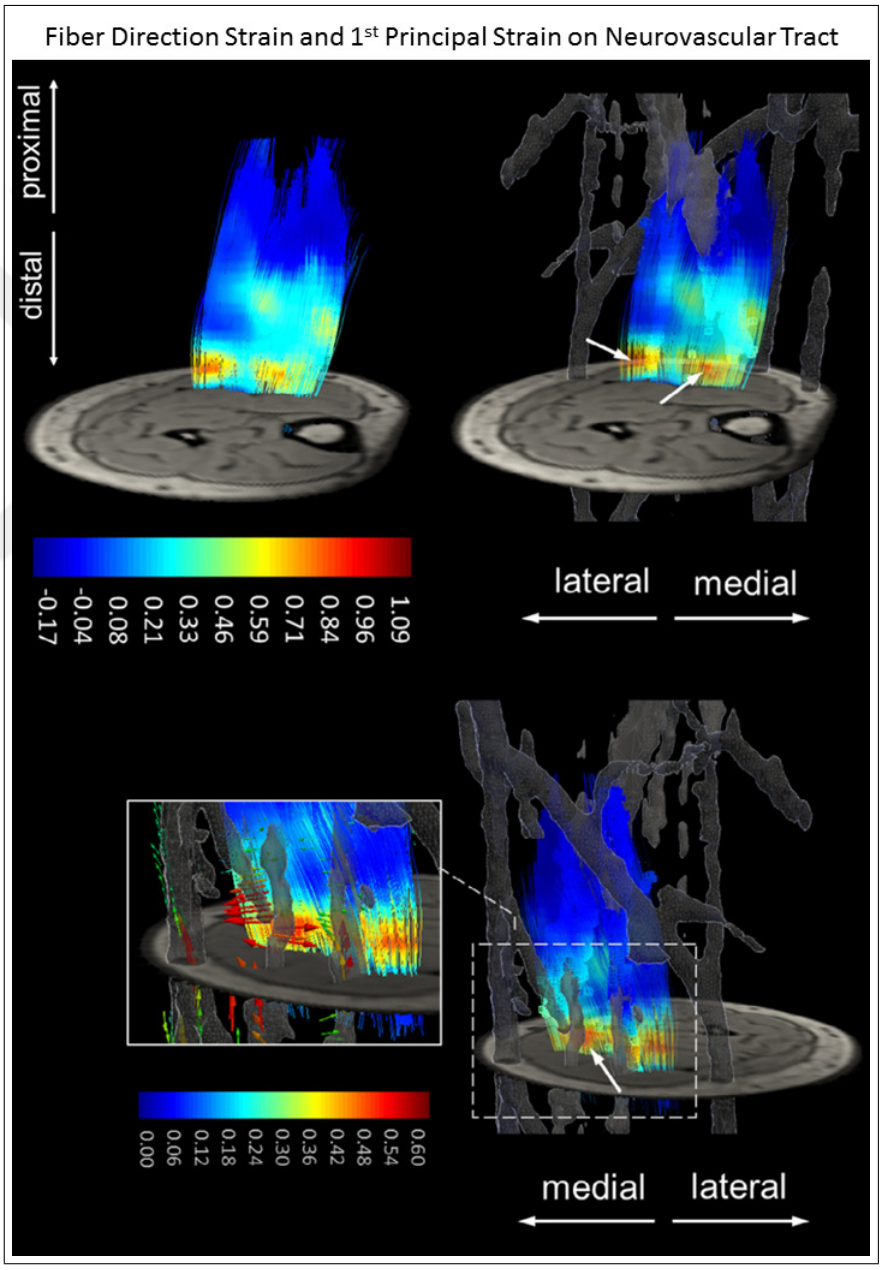

Figure B.1 Distributions of GM fiber direction strains (top left), and also first principal strains for local tissue deformations on NVTs (bottom left) due to sub-maximal plantar-flexion activity for one volunteer. Top panels provide anterior view whereas bottom panels provide posterior view.

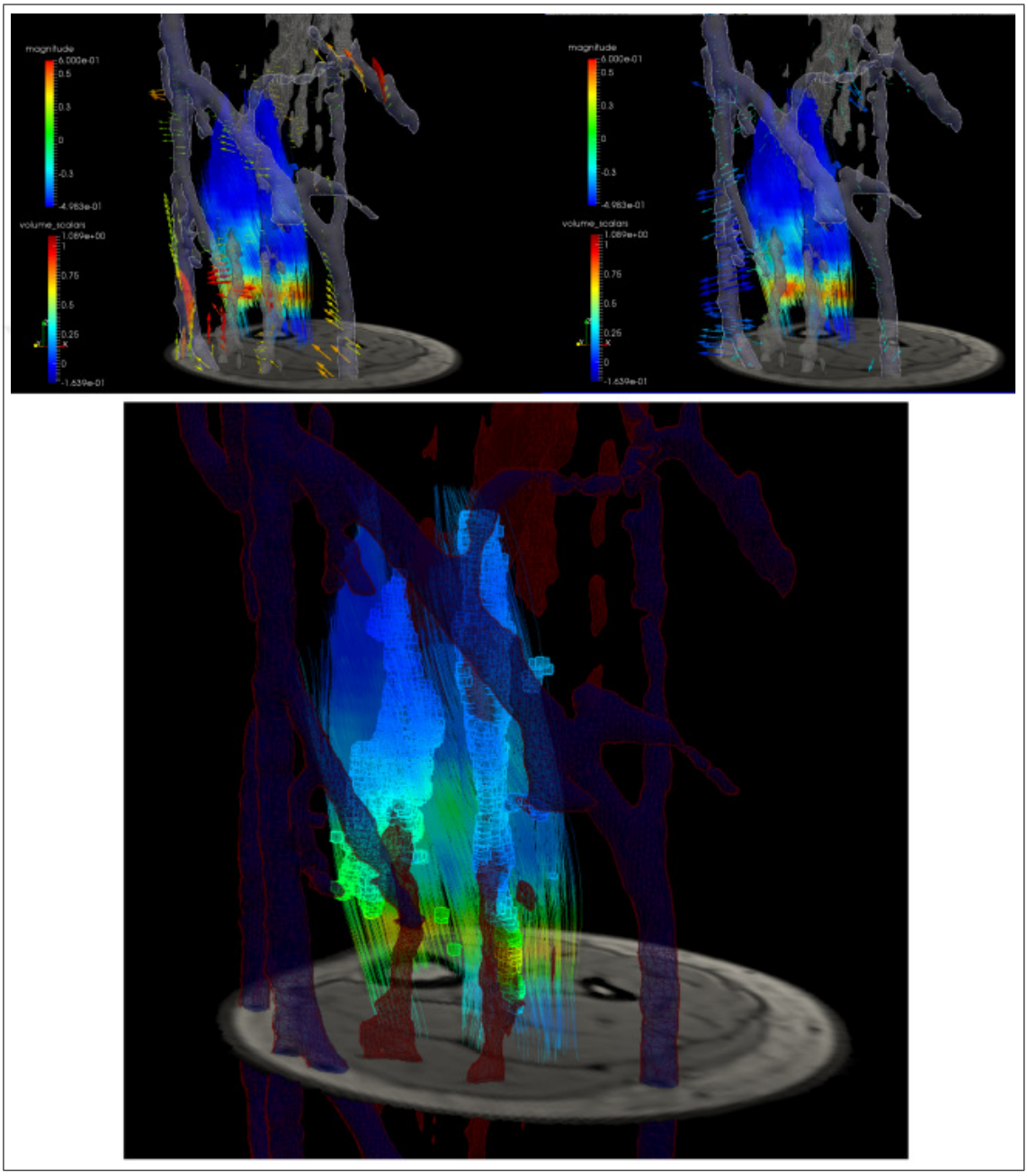

Figure B.2 Distributions of GM fiber direction strains, along with NVTs and local lengthening on them (top panels), and their intersections with GM tracts seen from posterior (bottom panel) view for the volunteer in Figure B.1.

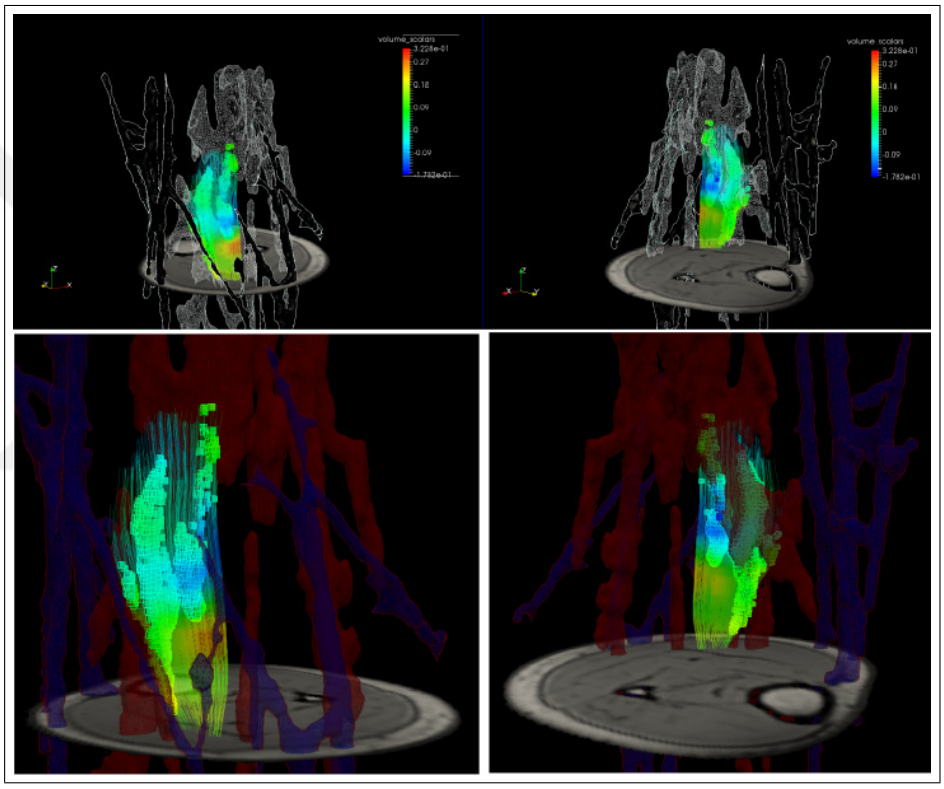

Figure B.3 Distributions of GM fiber direction strains (top panels), along with NVTs and their intersections (bottom panels) with GM tracts seen from posterior (left) and anterior (right) views for another volunteer.

APPENDIX C. MAGNETIC RESONANCE AND DIFFUSION TENSOR IMAGING FOR ASSESSMENT OF VOLUNTARY CYCLIC JOINT MOTION

C.1 MRI Compatible Joint Angle Measurement

In order to allow joint motion be traced by the fiber-optic rotary encoder (Micronor, MR328-D06C10), one malleolar support cup is coupled with a gear that transfers the motion to another axis, where it can be coupled with the rotary encoder. Rotary encoder signal is optically transmitted to the controller module (Micronor, MR320) in the MRI control room, where the signal is sent to data acquisition unit (BIOPAC, MP150)

Real-time ankle angle information is relayed to volunteers visually via an MRI compatible monitor. Also, a metronome output to MRI's patient sound channel helps volunteers keep periodicity of their cyclic plantar-flexion throughout the imaging sequence.

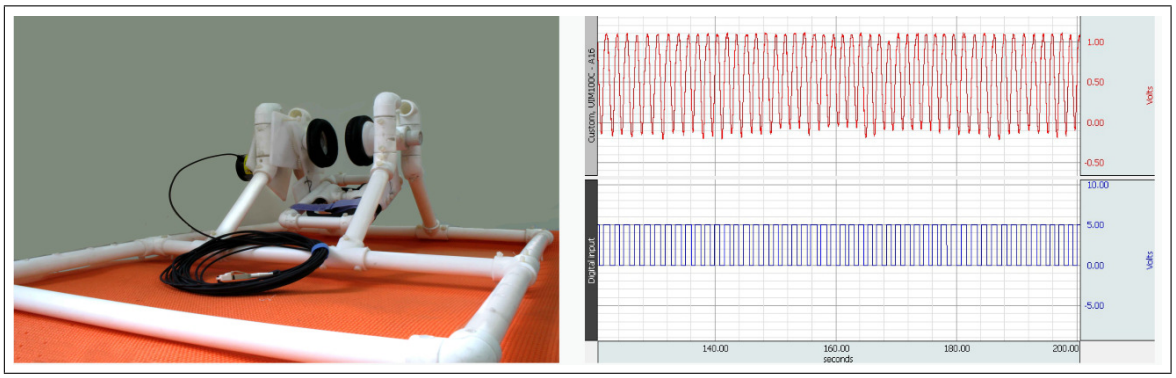

Figure C.1 Motion guiding fixation device (left) and recorded angular information by fiber-optic rotary encoder (right, top) along with resulting trigger waveforms (right, bottom).

C.2 Motion Triggering of MRI Device

AcqKnowledge (BIOPAC) software to define a threshold function that delivers a digial trigger signal. Digital output from MP150 is converted into optical signal using a custom-made circuit, passed on to MRI chamber and which is converted into trigger signal compatible with Siemens Trio 3 T by another converter (TELEMED), and sent to MRI device from the RCA external input located on the left side of the MRI, near the patient table control board.

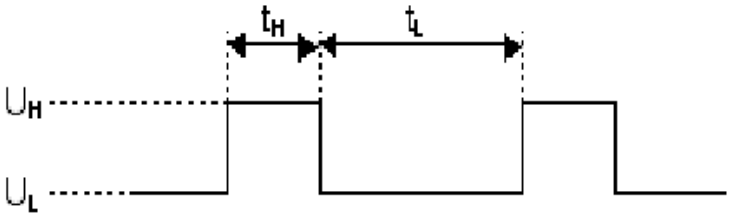

Voltage-time diagram for external triggering of the PMU

Name	Value
U_L	0 V ... 0.8 V
U_H	2 V ... 15 V
t_L(min.)	10 ms
t_H(min.)	10 ms
Input current	min. 2 mA
Input voltage	max. ± 20 V
Internal contact	+
External contact	–

The measurement sequence is triggered with the rising edge of the external signal.

Figure C.2 External trigger signal characteristics used in the study as required by for the Siemens Trio 3 T device.

Table C.1
PC and DT imaging parameters. [a] resampled at 128 x 128.

	PC Imaging Parameters	DT Imaging Parameters.
Sequence	cine 2D PC MRA	ss-EPI
Slice orientation	Sagittal	Sagittal
Repetition time (TR) (ms)	63.4	4900
Echo time (TE (ms)	5.4	61
FOV (mm^2)	192 x 192	180 x 180
Matrix (px^2	192 x 192	64 x 64[a]
Pixel size (mm^2)	1.25 x 1.25	1.4 x 1.4
Slice thickness (mm)	5.0	2.8
Flip angle (°)	30	90
Bandwidth (Hz/px)	143	2003
b-value (s/mm^2)	N/A	450
Number of diffusion directions	N/A	12
Velocity encoding v_{enc}	20	N/A

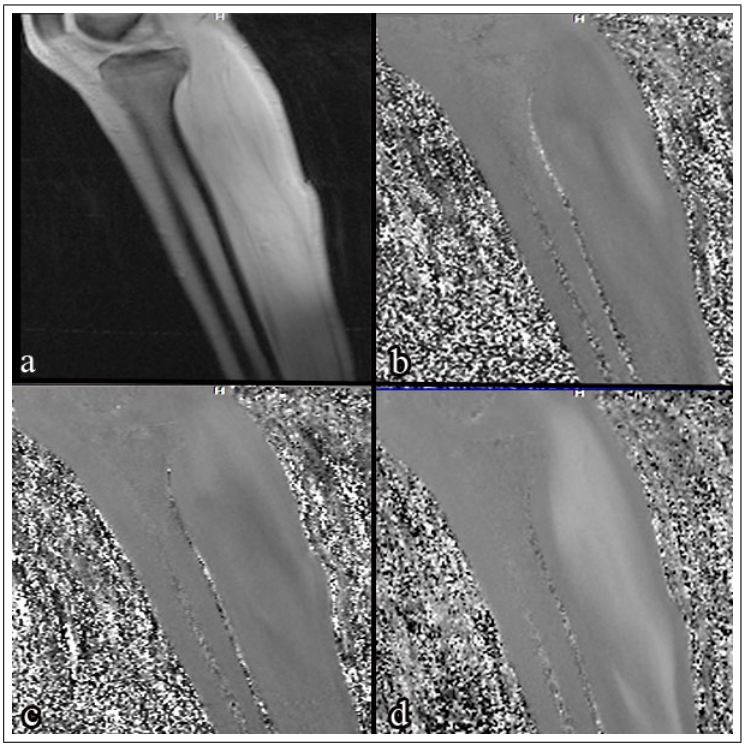

Figure C.3 (a) Magnitude image belonging to phase images, (b) x direction phase image, (c) y directon phase image and (d) z direction phase image. x, y and z directions correspond to medio–lateral, anterior–posterior and inferior–superior anatomical directions inside the MRI device, respectively.

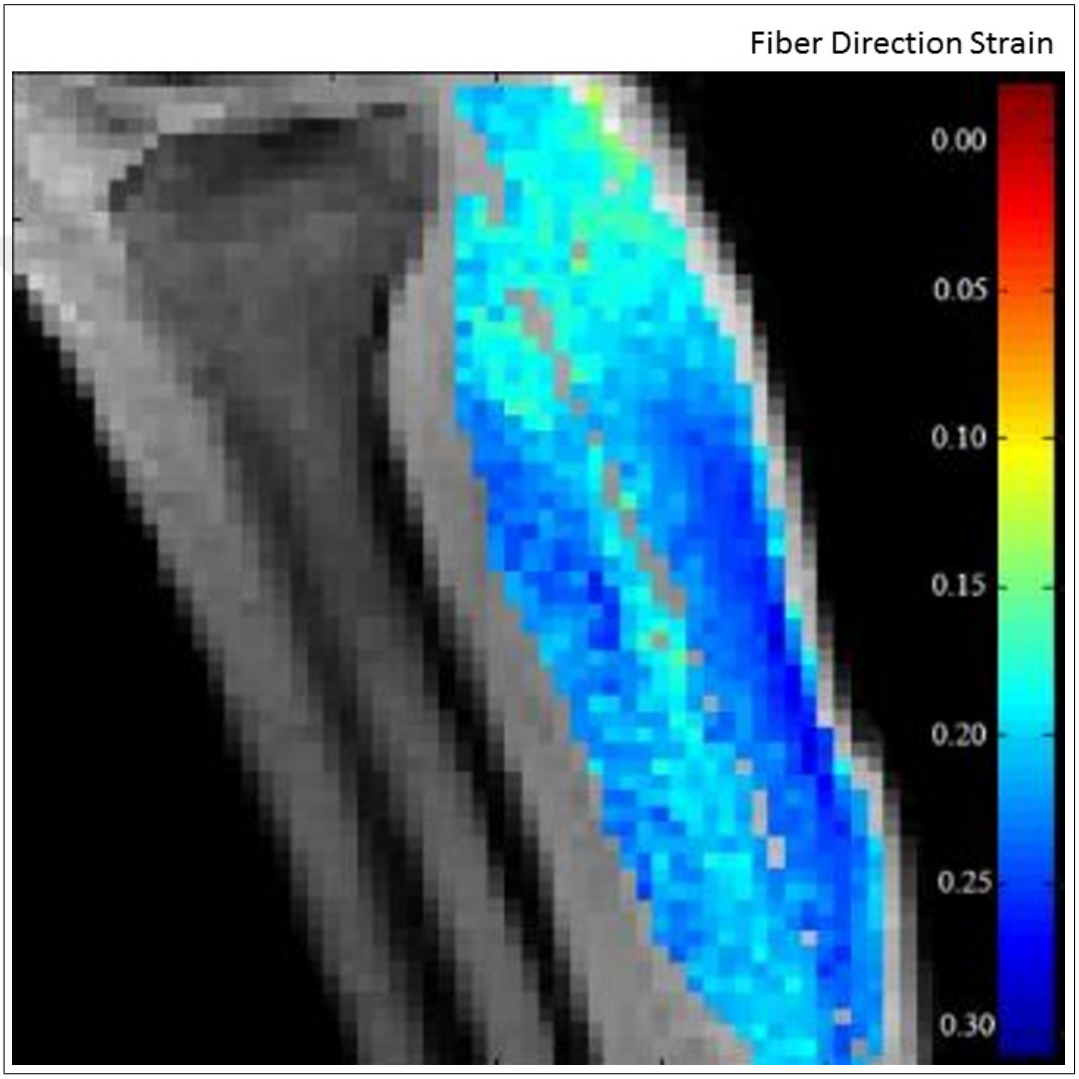

Figure C.4 Distributions of GM and SOL fiber direction strains during plantar-flexion phase of voluntary cyclic ankle plantar- and dorsi-flexion, displayed on a sagittal slice.

APPENDIX D. DETERMINATION OF ACTIVE STATE STIFFENED TITIN CONSTITUTIVE EQUATION

Active, actin–myosin cross-bridge force–length of sarcomeres which are actively stretched from 2.4 μm is acquired from Heidlauf et al. [18] (Figure D.1, their Figure 5). Passive and total force (during active stretch) data points are acquired from Schappacher-Tilp et al. [1] (their Figure 1) and are normalized to total active force at 2.4 μm (Figure D.2). Removing the cross-bridge force and passive force from total force would yield a constitutive equation describing active behavior of titin in eccentric contractions starting from 2.4 μm sarcomere length, which is a good approximation for the 2.4–2.5 μm initial sarcomere length range of present model.

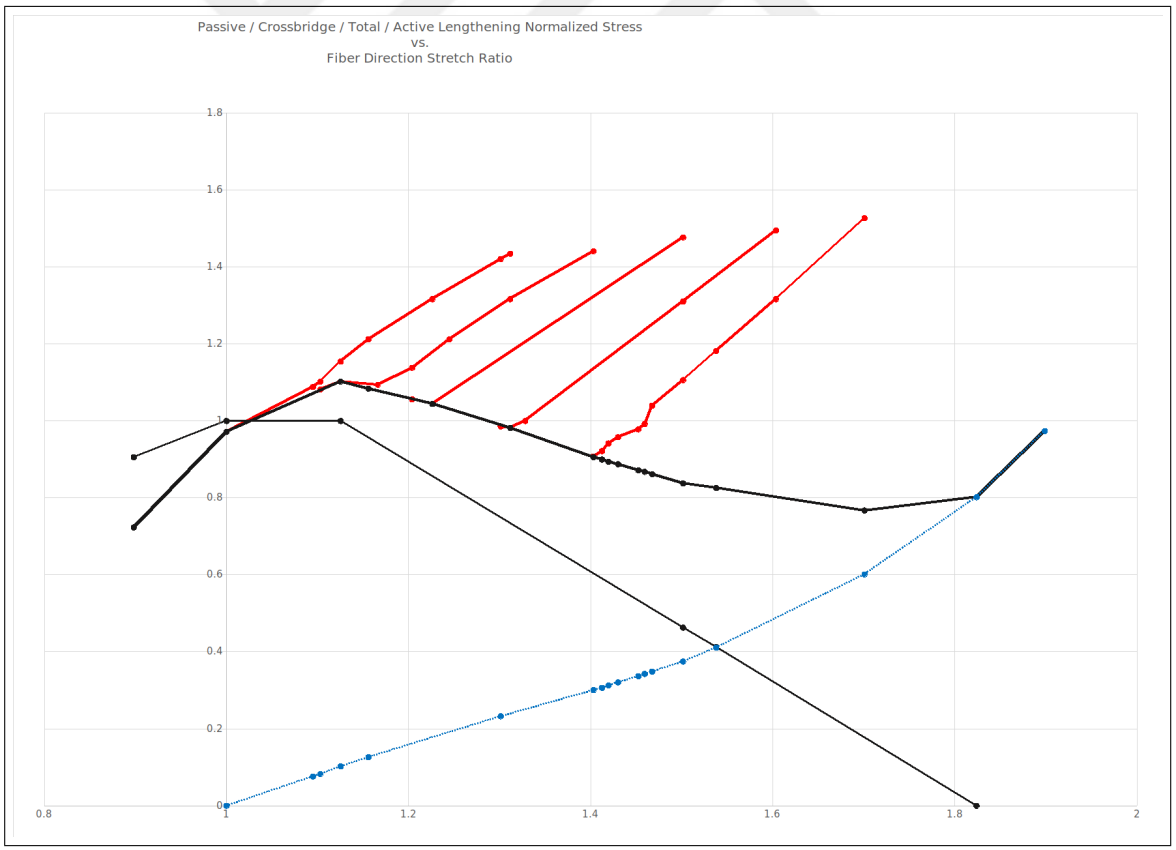

Figure D.1 Active stretch (red) simulations for different muscle lengths at start of activation (corresponding to initial fiber direction strains of 1.0, 1.1, 1.2, 1.3, 1.4). Isometric stressâstrain relations determined from continuum mechanical model (bold black) along with the active stress (black) obtained by subtracting passive stress (blue) from total stress are depicted. Data acquired from [18].

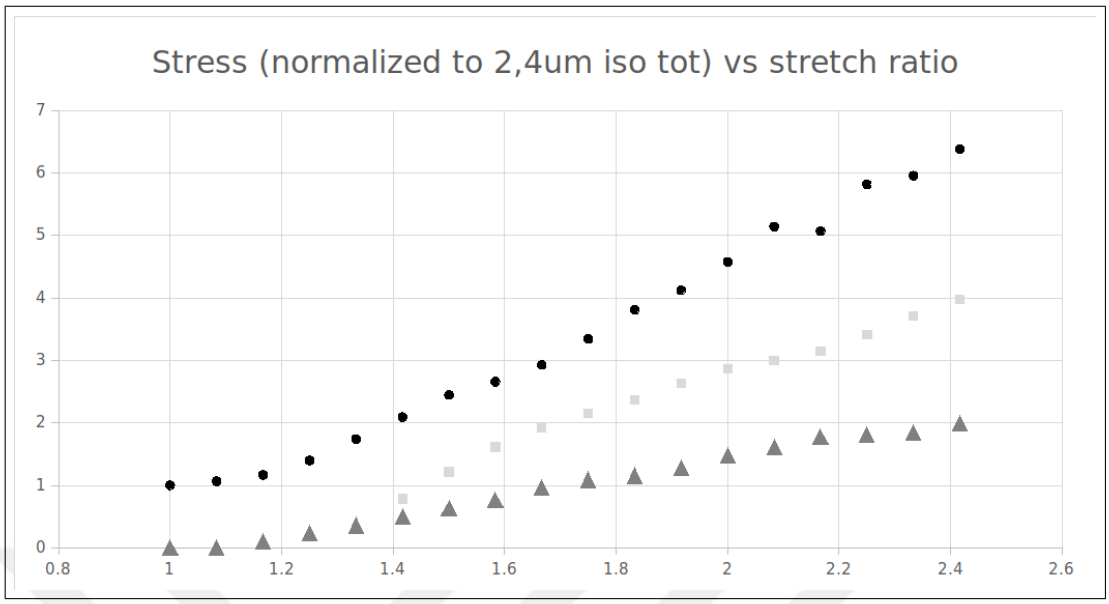

Figure D.2 Stress–strain relation for myofibrils stretched (i) in low [Ca^{2+}] solution (passive stretch, triangles), and in high [Ca^{2+}] solution from an initial sarcomere length of (ii) 2.4 μm (active stretch, circles) and (iii) 3.4 μm (active stretch from 3.4 μm, squares). Stresses are normalized to isometric total stress at 2.4 μm. Data acquired from [1].

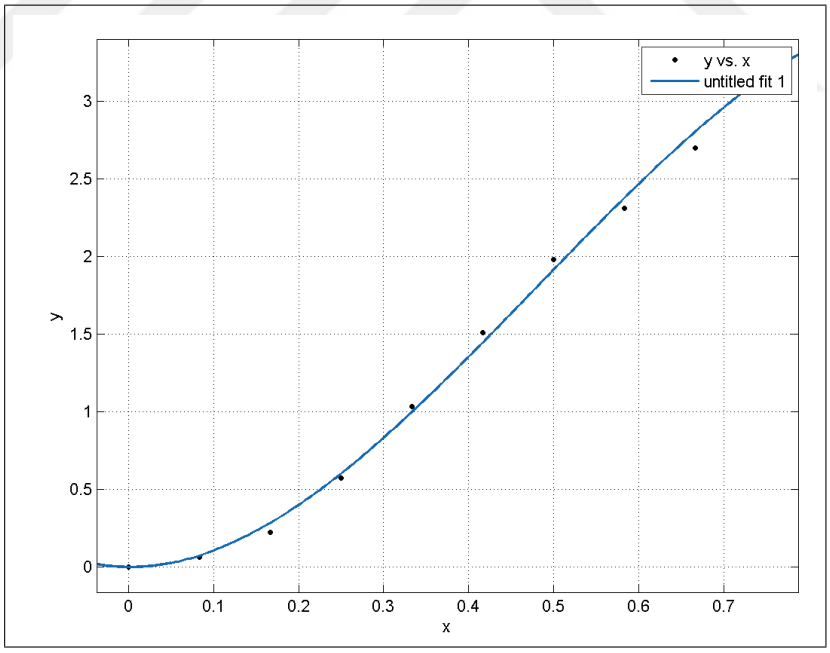

Figure D.3 Stress–strain constitutive equation of active state stiffened titin (Eq. 5.3) for active lengthening starting at 2.4 μm sarcomere length, acquired by subtracting passive force (Figure D.2) and actin–myosin cross-bridge force (Figure D.1) form total force (Figure D.2).

Recall that Eq. 5.3 reads

$$\sigma_{22titin}(\epsilon_{22}) = \begin{cases} h_1\epsilon_{22}^3 + h_2\epsilon_{22}^2 + h_3\epsilon_{22} & \text{if} \quad \epsilon_{22} > 0 \\ 0 & \text{if} \quad \epsilon_{22} < 0 \end{cases} \tag{D.1}$$

where h_1, h_2 and h_3 are constants (Table 5.1).

REFERENCES

1. Schappacher-Tilp, G., T. Leonard, G. Desch, and W. Herzog, "A novel three-filament model of force generation in eccentric contraction of skeletal muscles," *PLOS ONE*, Vol. 10, p. e0117634, Mar. 2015.

2. Trotter, J. A., and P. P. Purslow, "Functional morphology of the endomysium in series fibered muscles," *J. Morphol.*, Vol. 212, pp. 109–122, May 1992.

3. Huxley, A. F., "Muscle structure and theories of contraction," *Prog Biophys Biophys Chem*, Vol. 7, pp. 255–318, 1957.

4. Huxley, H. E., "Fifty years of muscle and the sliding filament hypothesis," *Eur. J. Biochem.*, Vol. 271, pp. 1403–1415, Apr. 2004.

5. Huxley, H. E., "The mechanism of muscular contraction," *Science*, Vol. 164, pp. 1356–1365, June 1969.

6. Huxley, A. F., and R. Niedergerke, "Measurement of the striations of isolated muscle fibres with the interference microscope," *J. Physiol. (Lond.)*, Vol. 144, pp. 403–425, Dec. 1958.

7. Labeit, D., K. Watanabe, C. Witt, H. Fujita, Y. Wu, S. Lahmers, T. Funck, S. Labeit, and H. Granzier, "Calcium-dependent molecular spring elements in the giant protein titin," *Proc. Natl. Acad. Sci. U.S.A.*, Vol. 100, pp. 13716–13721, Nov. 2003.

8. Linke, W. A., "Titin gene and protein functions in passive and active muscle," *Annual Review of Physiology*, Vol. 80, pp. 389–411, Feb. 2018.

9. Dutta, S., C. Tsiros, S. L. Sundar, H. Athar, J. Moore, B. Nelson, M. J. Gage, and K. Nishikawa, "Calcium increases titin n2a binding to f-actin and regulated thin filaments," *Scientific Reports*, Vol. 8, Dec. 2018.

10. Powers, K., G. Schappacher-Tilp, A. Jinha, T. Leonard, K. Nishikawa, and W. Herzog, "Titin force is enhanced in actively stretched skeletal muscle," *Journal of Experimental Biology*, Vol. 217, pp. 3629–3636, Oct. 2014.

11. Herzog, W., "Mechanisms of enhanced force production in lengthening (eccentric) muscle contractions," *Journal of Applied Physiology*, Vol. 116, pp. 1407–1417, June 2014.

12. Rassier, D. E., E.-J. Lee, and W. Herzog, "Modulation of passive force in single skeletal muscle fibres," *Biol. Lett.*, Vol. 1, pp. 342–345, Sept. 2005.

13. Herzog, W., and T. R. Leonard, "Force enhancement following stretching of skeletal muscle: a new mechanism," *J. Exp. Biol.*, Vol. 205, pp. 1275–1283, May 2002.

14. Rode, C., T. Siebert, and R. Blickhan, "Titin-induced force enhancement and force depression: a 'sticky-spring' mechanism in muscle contractions?," *J. Theor. Biol.*, Vol. 259, pp. 350–360, July 2009.

15. Tomalka, A., C. Rode, J. Schumacher, and T. Siebert, "The active force-length relationship is invisible during extensive eccentric contractions in skinned skeletal muscle fibres," *Proc. Biol. Sci.*, Vol. 284, May 2017.

16. Nishikawa, K. C., J. A. Monroy, T. E. Uyeno, S. H. Yeo, D. K. Pai, and S. L. Lindstedt, "Is titin a 'winding filament'? a new twist on muscle contraction," *Proceedings of the Royal Society B: Biological Sciences*, Vol. 279, pp. 981–990, Mar. 2012.

17. Rivas-Pardo, J., E. Eckels, I. Popa, P. Kosuri, W. Linke, and J. Fernández, "Work done by titin protein folding assists muscle contraction," *Cell Reports*, Vol. 14, pp. 1339–1347, Feb. 2016.

18. Heidlauf, T., T. Klotz, C. Rode, E. Altan, C. Bleiler, T. Siebert, and O. Röhrle, "A multi-scale continuum model of skeletal muscle mechanics predicting force enhancement based on actinâtitin interaction," *Biomechanics and Modeling in Mechanobiology*, Vol. 15, pp. 1423–1437, Dec. 2016.

19. Heidlauf, T., T. Klotz, C. Rode, T. Siebert, and O. Röhrle, "A continuum-mechanical skeletal muscle model including actin-titin interaction predicts stable contractions on the descending limb of the force-length relation," *PLoS Comput. Biol.*, Vol. 13, p. e1005773, Oct. 2017.

20. Ramsey, R. W., and S. F. Street, "The isometric length-tension diagram of isolated skeletal muscle fibers of the frog," *Journal of Cellular and Comparative Physiology*, Vol. 15, pp. 11–34, Feb. 1940.

21. Street, S. F., "Lateral transmission of tension in frog myofibers: a myofibrillar network and transverse cytoskeletal connections are possible transmitters," *J. Cell. Physiol.*, Vol. 114, pp. 346–364, Mar. 1983.

22. Huijing, P. A., G. C. Baan, and G. T. Rebel, "Non-myotendinous force transmission in rat extensor digitorum longus muscle," *J. Exp. Biol.*, Vol. 201 (Pt 12), pp. 683–691, June 1998.

23. Huijing, P. A., "Muscle as a collagen fiber reinforced composite: a review of force transmission in muscle and whole limb," *J Biomech*, Vol. 32, pp. 329–345, Apr. 1999.

24. Yucesoy, C. A., B. H. F. J. M. Koopman, P. A. Huijing, and H. J. Grootenboer, "Three-dimensional finite element modeling of skeletal muscle using a two-domain approach: linked fiber-matrix mesh model," *J Biomech*, Vol. 35, pp. 1253–1262, Sept. 2002.

25. Tidball, J. G., "Myotendinous junction injury in relation to junction structure and molecular composition," *Exerc Sport Sci Rev*, Vol. 19, pp. 419–445, 1991.

26. Hawkins, D., and M. Bey, "Muscle and tendon force-length properties and their interactions in vivo," *J Biomech*, Vol. 30, pp. 63–70, Jan. 1997.

27. Adstrum, S., G. Hedley, R. Schleip, C. Stecco, and C. A. Yucesoy, "Defining the fascial system," *J Bodyw Mov Ther*, Vol. 21, pp. 173–177, Jan. 2017.

28. Yucesoy, C. A., G. C. Baan, B. H. F. J. M. Koopman, H. J. Grootenboer, and P. A. Huijing, "Pre-strained epimuscular connections cause muscular myofascial force transmission to affect properties of synergistic 'ehl' and 'edl' muscles of the rat," *J Biomech Eng*, Vol. 127, pp. 819–828, Oct. 2005.

29. Huijing, P. A., and G. C. Baan, "Myofascial force transmission causes interaction between adjacent muscles and connective tissue: effects of blunt dissection and compartmental fasciotomy on length force characteristics of rat extensor digitorum longus muscle," *Arch. Physiol. Biochem.*, Vol. 109, pp. 97–109, Apr. 2001.

30. Huijing, P. A., and G. C. Baan, "Extramuscular myofascial force transmission within the rat anterior tibial compartment: proximo-distal differences in muscle force," *Acta Physiol. Scand.*, Vol. 173, pp. 297–311, Nov. 2001.

31. Yucesoy, C. A., and P. A. Huijing, "Substantial effects of epimuscular myofascial force transmission on muscular mechanics have major implications on spastic muscle and remedial surgery," *J Electromyogr Kinesiol*, Vol. 17, pp. 664–679, Dec. 2007.

32. Yucesoy, C. A., "Epimuscular myofascial force transmission implies novel principles for muscular mechanics," *Exerc Sport Sci Rev*, Vol. 38, pp. 128–134, July 2010.

33. Maas, H., G. C. Baan, and P. A. Huijing, "Muscle force is determined also by muscle relative position: isolated effects," *J Biomech*, Vol. 37, pp. 99–110, Jan. 2004.

34. Narici, M. V., T. Binzoni, E. Hiltbrand, J. Fasel, F. Terrier, and P. Cerretelli, "In vivo human gastrocnemius architecture with changing joint angle at rest and during graded isometric contraction," *J. Physiol. (Lond.)*, Vol. 496 (Pt 1), pp. 287–297, Oct. 1996.

35. Kawakami, Y., Y. Ichinose, and T. Fukunaga, "Architectural and functional features of human triceps surae muscles during contraction," *J. Appl. Physiol.*, Vol. 85, pp. 398–404, Aug. 1998.

36. Wakahara, T., H. Kanehisa, Y. Kawakami, and T. Fukunaga, "Effects of knee joint angle on the fascicle behavior of the gastrocnemius muscle during eccentric plantar flexions," *J Electromyogr Kinesiol*, Vol. 19, pp. 980–987, Oct. 2009.

37. Bojsen-Møller, J., S. Schwartz, K. K. Kalliokoski, T. Finni, and S. P. Magnusson, "Intermuscular force transmission between human plantarflexor muscles in vivo," *J. Appl. Physiol.*, Vol. 109, pp. 1608–1618, Dec. 2010.

38. Asakawa, D. S., G. P. Pappas, S. S. Blemker, J. E. Drace, and S. L. Delp, "Cine phase-contrast magnetic resonance imaging as a tool for quantification of skeletal muscle motion," *Semin Musculoskelet Radiol*, Vol. 7, pp. 287–295, Dec. 2003.

39. Pelc, N. J., R. J. Herfkens, A. Shimakawa, and D. R. Enzmann, "Phase contrast cine magnetic resonance imaging," *Magn Reson Q*, Vol. 7, pp. 229–254, Oct. 1991.

40. Kim, D., W. D. Gilson, C. M. Kramer, and F. H. Epstein, "Myocardial tissue tracking with two-dimensional cine displacement-encoded mr imaging: development and initial evaluation," *Radiology*, Vol. 230, pp. 862–871, Mar. 2004.

41. Pappas, G. P., D. S. Asakawa, S. L. Delp, F. E. Zajac, and J. E. Drace, "Nonuniform shortening in the biceps brachii during elbow flexion," *J. Appl. Physiol.*, Vol. 92, pp. 2381–2389, June 2002.

42. Asakawa, D. S., S. S. Blemker, G. E. Gold, and S. L. Delp, "In vivo motion of the rectus femoris muscle after tendon transfer surgery," *J Biomech*, Vol. 35, pp. 1029–1037, Aug. 2002.

43. Kinugasa, R., D. Shin, J. Yamauchi, C. Mishra, J. A. Hodgson, V. R. Edgerton, and S. Sinha, "Phase-contrast mri reveals mechanical behavior of superficial and deep aponeuroses in human medial gastrocnemius during isometric contraction," *J. Appl. Physiol.*, Vol. 105, pp. 1312–1320, Oct. 2008.

44. Zhong, X., F. H. Epstein, B. S. Spottiswoode, P. A. Helm, and S. S. Blemker, "Imaging two-dimensional displacements and strains in skeletal muscle during joint motion by cine dense mr," *J Biomech*, Vol. 41, no. 3, pp. 532–540, 2008.

45. Fiorentino, N. M., F. H. Epstein, and S. S. Blemker, "Activation and aponeurosis morphology affect in vivo muscle tissue strains near the myotendinous junction," *J Biomech*, Vol. 45, pp. 647–652, Feb. 2012.

46. Huijing, P. A., A. Yaman, C. Ozturk, and C. A. Yucesoy, "Effects of knee joint angle on global and local strains within human triceps surae muscle: Mri analysis indicating in vivo myofascial force transmission between synergistic muscles," *Surg Radiol Anat*, Vol. 33, pp. 869–879, Dec. 2011.

47. Thirion, J. P., "Image matching as a diffusion process: an analogy with maxwell's demons," *Med Image Anal*, Vol. 2, pp. 243–260, Sept. 1998.

48. Prompers, J. J., J. A. L. Jeneson, M. R. Drost, C. C. W. Oomens, G. J. Strijkers, and K. Nicolay, "Dynamic mrs and mri of skeletal muscle function and biomechanics," *NMR in Biomedicine*, Vol. 19, pp. 927–953, Nov. 2006.

49. Van Donkelaar, C. C., L. J. Kretzers, P. H. Bovendeerd, L. M. Lataster, K. Nicolay, J. D. Janssen, and M. R. Drost, "Diffusion tensor imaging in biomechanical studies of skeletal muscle function," *J. Anat.*, Vol. 194 (Pt 1), pp. 79–88, Jan. 1999.

50. Budzik, J. F., V. Le Thuc, X. Demondion, M. Morel, D. Chechin, and A. Cotten, "In vivo mr tractography of thigh muscles using diffusion imaging: initial results," *Eur Radiol*, Vol. 17, pp. 3079–3085, Dec. 2007.

51. Galbán, C. J., S. Maderwald, K. Uffmann, A. de Greiff, and M. E. Ladd, "Diffusive sensitivity to muscle architecture: a magnetic resonance diffusion tensor imaging study of the human calf," *Eur. J. Appl. Physiol.*, Vol. 93, pp. 253–262, Dec. 2004.

52. Tseng, W.-Y. I., V. J. Wedeen, T. G. Reese, R. N. Smith, and E. F. Halpern, "Diffusion tensor mri of myocardial fibers and sheets: correspondence with visible cut-face texture," *J Magn Reson Imaging*, Vol. 17, pp. 31–42, Jan. 2003.

53. A M Heemskerk, T K Sinha, K. J. W. B. M. D., "Change in water diffusion properties with altered muscle architecture," in *Proc 16th Annual Meeting ISMRM*, Vol. 1787, (Toronto), May 2008.

54. Heemskerk, A. M., M. R. Drost, G. S. van Bochove, M. F. M. van Oosterhout, K. Nicolay, and G. J. Strijkers, "Dti-based assessment of ischemia-reperfusion in mouse skeletal muscle," *Magn Reson Med*, Vol. 56, pp. 272–281, Aug. 2006.

55. Schwenzer, N. F., G. Steidle, P. Martirosian, C. Schraml, F. Springer, C. D. Claussen, and F. Schick, "Diffusion tensor imaging of the human calf muscle: distinct changes in fractional anisotropy and mean diffusion due to passive muscle shortening and stretching," *NMR Biomed*, Vol. 22, pp. 1047–1053, Dec. 2009.

56. Damon, B. M., Z. Ding, A. W. Anderson, A. S. Freyer, and J. C. Gore, "Validation of diffusion tensor mri-based muscle fiber tracking," *Magn Reson Med*, Vol. 48, pp. 97–104, July 2002.

57. Heemskerk, A. M., T. K. Sinha, K. J. Wilson, Z. Ding, and B. M. Damon, "Repeatability of dti-based skeletal muscle fiber tracking," *NMR in Biomedicine*, pp. n/a–n/a, 2010.

58. Damon, B. M., "Effects of image noise in muscle diffusion tensor (dt)-mri assessed using numerical simulations," *Magn Reson Med*, Vol. 60, pp. 934–944, Oct. 2008.

59. Saupe, N., L. M. White, M. S. Sussman, A. Kassner, G. Tomlinson, and M. D. Noseworthy, "Diffusion tensor magnetic resonance imaging of the human calf: Comparison between 1.5t and 3.0t â preliminary results," *Investigative Radiology*, Vol. 43, pp. 612–618, Sept. 2008.

60. Froeling, M., A. J. Nederveen, D. F. R. Heijtel, A. Lataster, C. Bos, K. Nicolay, M. Maas, M. R. Drost, and G. J. Strijkers, "Diffusion-tensor mri reveals the complex muscle architecture of the human forearm," *J Magn Reson Imaging*, Vol. 36, pp. 237–248, July 2012.

61. Lansdown, D. A., Z. Ding, M. Wadington, J. L. Hornberger, and B. M. Damon, "Quantitative diffusion tensor mri-based fiber tracking of human skeletal muscle," *J. Appl. Physiol.*, Vol. 103, pp. 673–681, Aug. 2007.

62. Sinha, U., S. Sinha, J. A. Hodgson, and R. V. Edgerton, "Human soleus muscle architecture at different ankle joint angles from magnetic resonance diffusion tensor imaging," *J. Appl. Physiol.*, Vol. 110, pp. 807–819, Mar. 2011.

63. Bolsterlee, B., T. Finni, A. D'Souza, J. Eguchi, E. C. Clarke, and R. D. Herbert, "Three-dimensional architecture of the whole human soleus muscle in vivo," *PeerJ*, Vol. 6, p. e4610, 2018.

64. Kan, J. H., A. M. Heemskerk, Z. Ding, A. Gregory, G. Mencio, K. Spindler, and B. M. Damon, "Dti-based muscle fiber tracking of the quadriceps mechanism in lateral patellar dislocation," *J Magn Reson Imaging*, Vol. 29, pp. 663–670, Mar. 2009.

65. Turkoglu, A. N., P. A. Huijing, and C. A. Yucesoy, "Mechanical principles of effects of botulinum toxin on muscle length-force characteristics: an assessment by finite element modeling," *J Biomech*, Vol. 47, pp. 1565–1571, May 2014.

66. Turkoglu, A. N., and C. A. Yucesoy, "Simulation of effects of botulinum toxin on muscular mechanics in time course of treatment based on adverse extracellular matrix adaptations," *J Biomech*, Vol. 49, no. 7, pp. 1192–1198, 2016.

67. Yucesoy, C. A., B. H. F. J. M. Koopman, H. J. Grootenboer, and P. A. Huijing, "Finite element modeling of aponeurotomy: altered intramuscular myofascial force transmission yields complex sarcomere length distributions determining acute effects," *Biomech Model Mechanobiol*, Vol. 6, pp. 227–243, July 2007.

68. Yucesoy, C. A., and P. A. Huijing, "Assessment by finite element modeling indicates that surgical intramuscular aponeurotomy performed closer to the tendon enhances intended acute effects in extramuscularly connected muscle," *Journal of Biomechanical Engineering*, Vol. 131, no. 2, p. 021012, 2009.

69. Bassett, K. T., S. A. Lingman, and R. F. Ellis, "The use and treatment efficacy of kiaesthetic taping for musculoskeletal conditions: A systematic review," *NZJ Physiother*, Vol. 38, pp. 56–62, Jan. 2010.

70. Williams, S., C. Whatman, P. A. Hume, and K. Sheerin, "Kinesio taping in treatment and prevention of sports injuries: a meta-analysis of the evidence for its effectiveness," *Sports Med*, Vol. 42, pp. 153–164, Feb. 2012.

71. Fratocchi, G., F. Di Mattia, R. Rossi, M. Mangone, V. Santilli, and M. Paoloni, "Influence of kinesio taping applied over biceps brachii on isokinetic elbow peak torque. a placebo controlled study in a population of young healthy subjects," *J Sci Med Sport*, Vol. 16, pp. 245–249, May 2013.

72. Hsu, Y.-H., W.-Y. Chen, H.-C. Lin, W. T. J. Wang, and Y.-F. Shih, "The effects of taping on scapular kinematics and muscle performance in baseball players with shoulder impingement syndrome," *J Electromyogr Kinesiol*, Vol. 19, pp. 1092–1099, Dec. 2009.

73. Słupik, A., M. Dwornik, D. Białoszewski, and E. Zych, "Effect of kinesio taping on bioelectrical activity of vastus medialis muscle. preliminary report," *Ortop Traumatol Rehabil*, Vol. 9, pp. 644–651, Dec. 2007.

74. González-Iglesias, J., C. Fernández-de Las-Peñas, J. A. Cleland, P. Huijbregts, and M. Del Rosario Gutiérrez-Vega, "Short-term effects of cervical kinesio taping on pain and cervical range of motion in patients with acute whiplash injury: a randomized clinical trial," *J Orthop Sports Phys Ther*, Vol. 39, pp. 515–521, July 2009.

75. Thelen, M. D., J. A. Dauber, and P. D. Stoneman, "The clinical efficacy of kinesio tape for shoulder pain: a randomized, double-blinded, clinical trial," *J Orthop Sports Phys Ther*, Vol. 38, pp. 389–395, July 2008.

76. Chang, H.-Y., K.-Y. Chou, J.-J. Lin, C.-F. Lin, and C.-H. Wang, "Immediate effect of forearm kinesio taping on maximal grip strength and force sense in healthy collegiate athletes," *Phys Ther Sport*, Vol. 11, pp. 122–127, Nov. 2010.

77. Karwacińska, J., W. Kiebzak, B. Stepanek-Finda, I. M. Kowalski, H. Protasiewicz-Fałdowska, R. Trybulski, and M. Starczyńska, "Effectiveness of kinesio taping on hypertrophic scars, keloids and scar contractures," *Polish Annals of Medicine*, Vol. 19, pp. 50–57, Jan. 2012.

78. Shim, J.-Y., H.-R. Lee, and D.-C. Lee, "The use of elastic adhesive tape to promote lymphatic flow in the rabbit hind leg," *Yonsei Med. J.*, Vol. 44, pp. 1045–1052, Dec. 2003.

79. Aguilar-Ferrándiz, M. E., A. M. Castro-Sánchez, G. A. Matarán-Peñarrocha, F. García-Muro, T. Serge, and C. Moreno-Lorenzo, "Effects of kinesio taping on venous symptoms, bioelectrical activity of the gastrocnemius muscle, range of ankle motion, and quality of life in postmenopausal women with chronic venous insufficiency: a randomized controlled trial," *Arch Phys Med Rehabil*, Vol. 94, pp. 2315–2328, Dec. 2013.

80. Alexander, C., S. Stynes, A. Thomas, J. Lewis, and P. Harrison, "Does tape facilitate or inhibit the lower fibres of trapezius?," *Manual Therapy*, Vol. 8, pp. 37–41, Feb. 2003.

81. Alexander, C. M., M. McMullan, and P. J. Harrison, "What is the effect of taping along or across a muscle on motoneurone excitability? a study using triceps surae," *Man Ther*, Vol. 13, pp. 57–62, Feb. 2008.

82. Briem, K., H. Eythörsdöttir, R. G. Magnúsdóttir, R. Pálmarsson, T. Rúnarsdöttir, and T. Sveinsson, "Effects of kinesio tape compared with nonelastic sports tape and the untaped ankle during a sudden inversion perturbation in male athletes," *J Orthop Sports Phys Ther*, Vol. 41, pp. 328–335, May 2011.

83. Lee, M. H., C. R. Lee, J. S. Park, S. Y. Lee, T. G. Jeong, G. S. Son, J. Y. Lee, E. C. Kim, and Y. K. Kim, "Influence of kinesio taping on the motor neuron conduction velocity," *Journal of Physical Therapy Science*, Vol. 23, no. 2, pp. 313–315, 2011.

84. Halseth, T., J. W. McChesney, M. Debeliso, R. Vaughn, and J. Lien, "The effects of kinesioâ taping on proprioception at the ankle," *J Sports Sci Med*, Vol. 3, pp. 1–7, Mar. 2004.

85. Kase, K., J. Wallis, and T. Kase, *Clinical therapeutic applications of the kinesio taping method*, New Mexico: Kinesio Taping Association, 2013. OCLC: 925510517.

86. Tamburella, F., G. Scivoletto, and M. Molinari, "Somatosensory inputs by application of 'kinesiotaping': effects on spasticity, balance, and gait in chronic spinal cord injury," *Frontiers in Human Neuroscience*, Vol. 8, May 2014.

87. Huijing, P. A., "Epimuscular myofascial force transmission: a historical review and implications for new research. international society of biomechanics muybridge award lecture, taipei, 2007," *J Biomech*, Vol. 42, pp. 9–21, Jan. 2009.

88. Yucesoy, C. A., B. H. F. J. M. Koopman, G. C. Baan, H. J. Grootenboer, and P. A. Huijing, "Effects of inter- and extramuscular myofascial force transmission on adjacent synergistic muscles: assessment by experiments and finite-element modeling," *J Biomech*, Vol. 36, pp. 1797–1811, Dec. 2003.

89. Berthier, C., and S. Blaineau, "Supramolecular organization of the subsarcolemmal cytoskeleton of adult skeletal muscle fibers. a review," *Biol. Cell*, Vol. 89, pp. 413–434, Oct. 1997.

90. Maas, H., G. C. Baan, and P. A. Huijing, "Intermuscular interaction via myofascial force transmission: effects of tibialis anterior and extensor hallucis longus length on force transmission from rat extensor digitorum longus muscle," *Journal of Biomechanics*, Vol. 34, pp. 927–940, July 2001.

91. Rijkelijkhuizen, J. M., H. J. M. Meijer, G. C. Baan, and P. A. Huijing, "Myofascial force transmission also occurs between antagonistic muscles located within opposite compartments of the rat lower hind limb," *J Electromyogr Kinesiol*, Vol. 17, pp. 690–697, Dec. 2007.

92. Yucesoy, C. A., G. Baan, and P. A. Huijing, "Epimuscular myofascial force transmission occurs in the rat between the deep flexor muscles and their antagonistic muscles," *J Electromyogr Kinesiol*, Vol. 20, pp. 118–126, Feb. 2010.

93. Yaman, A., C. Ozturk, P. A. Huijing, and C. A. Yucesoy, "Magnetic resonance imaging assessment of mechanical interactions between human lower leg muscles in vivo," *J Biomech Eng*, Vol. 135, p. 91003, Sept. 2013.

94. Norkin, C. C., and D. J. White, *Measurement of joint motion: a guide to goniometry*, Philadelphia: F.A. Davis, 4th ed ed., 2009. OCLC: ocn244265662.

95. Weis, J., A. Ericsson, and A. Hemmingsson, "Chemical shift artifact-free imaging: a new option in mri?," *Magn Reson Imaging*, Vol. 16, pp. 839–844, Sept. 1998.

96. Gao, H., A. Allan, C. McComb, X. Luo, and C. Berry, "Left ventricular strain and its pattern estimated from cine cmr and validation with dense," *Phys Med Biol*, Vol. 59, pp. 3637–3656, July 2014.

97. Mansi, T., J.-M. Peyrat, M. Sermesant, H. Delingette, J. Blanc, Y. Boudjemline, and N. Ayache, "Physically-constrained diffeomorphic demons for the estimation of 3d myocardium strain from cine-mri," in *Functional Imaging and Modeling of the Heart* (Ayache, N., H. Delingette, and M. Sermesant, eds.), Vol. 5528, pp. 201–210, Berlin, Heidelberg: Springer Berlin Heidelberg, 2009.

98. Moglo, K. E., and A. Shirazi-Adl, "Cruciate coupling and screw-home mechanism in passive knee joint during extension–flexion," *J Biomech*, Vol. 38, pp. 1075–1083, May 2005.

99. Wang, H., L. Dong, J. O'Daniel, R. Mohan, A. S. Garden, K. K. Ang, D. A. Kuban, M. Bonnen, J. Y. Chang, and R. Cheung, "Validation of an accelerated 'demons' algorithm for deformable image registration in radiation therapy," *Phys Med Biol*, Vol. 50, pp. 2887–2905, June 2005.

100. Latifi, K., G. Zhang, M. Stawicki, W. van Elmpt, A. Dekker, and K. Forster, "Validation of three deformable image registration algorithms for the thorax," *Journal of Applied Clinical Medical Physics*, Vol. 14, pp. 19–30, Jan. 2013.

101. Shi, J., J.-Y. Guo, S.-X. Hu, and Y.-P. Zheng, "Recognition of finger flexion motion from ultrasound image: A feasibility study," *Ultrasound in Medicine & Biology*, Vol. 38, pp. 1695–1704, Oct. 2012.

102. Fedorov, A., E. Billet, M. Prastawa, G. Gerig, A. Radmanesh, S. K. Warfield, R. Kikinis, and N. Chrisochoides, "Evaluation of brain mri alignment with the robust hausdorff distance measures," in *Advances in Visual Computing* (Hutchison, D., T. Kanade, J. Kittler, J. M. Kleinberg, F. Mattern, J. C. Mitchell, M. Naor, O. Nierstrasz, C. Pandu Rangan, B. Steffen, M. Sudan, D. Terzopoulos, D. Tygar, M. Y. Vardi, G. Weikum, G. Bebis, R. Boyle, B. Parvin, D. Koracin, P. Remagnino, F. Porikli, J. Peters, J. Klosowski, L. Arns, Y. K. Chun, T.-M. Rhyne, and L. Monroe, eds.), Vol. 5358, pp. 594–603, Berlin, Heidelberg: Springer Berlin Heidelberg, 2008.

103. Vercauteren, T., X. Pennec, A. Perchant, and N. Ayache, "Diffeomorphic demons: efficient non-parametric image registration," *Neuroimage*, Vol. 45, pp. S61–72, Mar. 2009.

104. Chang, J., T.-S. Suh, and D.-S. Lee, "Development of a deformable lung phantom for the evaluation of deformable registration," *Journal of Applied Clinical Medical Physics*, Vol. 11, pp. 281–286, Dec. 2010.

105. van Zuijlen, P. P. M., J. J. B. Ruurda, H. A. van Veen, J. van Marle, A. J. M. van Trier, F. Groenevelt, R. W. Kreis, and E. Middelkoop, "Collagen morphology in human skin and scar tissue: no adaptations in response to mechanical loading at joints," *Burns*, Vol. 29, pp. 423–431, Aug. 2003.

106. Langevin, H. M., and P. A. Huijing, "Communicating about fascia: history, pitfalls, and recommendations," *Int J Ther Massage Bodywork*, Vol. 2, pp. 3–8, Dec. 2009.

107. Nash, L. G., M. N. Phillips, H. Nicholson, R. Barnett, and M. Zhang, "Skin ligaments: regional distribution and variation in morphology," *Clin Anat*, Vol. 17, pp. 287–293, May 2004.

108. Wilkes, G. L., I. A. Brown, and R. H. Wildnauer, "The biomechanical properties of skin," *CRC Crit Rev Bioeng*, Vol. 1, pp. 453–495, Aug. 1973.

109. Huijing, P. A., "Epimuscular myofascial force transmission between antagonistic and synergistic muscles can explain movement limitation in spastic paresis," *J Electromyogr Kinesiol*, Vol. 17, pp. 708–724, Dec. 2007.

110. Purves, D., and S. M. Williams, eds., *Neuroscience*, Sunderland, Mass: Sinauer Associates, 2nd ed ed., 2001.

111. Grigg, P., "Stretch sensitivity of mechanoreceptor neurons in rat hairy skin," *Journal of Neurophysiology*, Vol. 76, pp. 2886–2895, Nov. 1996.

112. Liljencrantz, J., and H. Olausson, "Tactile c fibers and their contributions to pleasant sensations and to tactile allodynia," *Frontiers in Behavioral Neuroscience*, Vol. 8, Mar. 2014.

113. Hotta, H., R. F. Schmidt, S. Uchida, and N. Watanabe, "Gentle mechanical skin stimulation inhibits the somatocardiac sympathetic c-reflex elicited by excitation of unmyelinated c-afferent fibers," *Eur J Pain*, Vol. 14, pp. 806–813, Sept. 2010.

114. Ristow, O., C. Pautke, n. Victoria Kehl, S. Koerdt, K. Schwärzler, L. Hahnefeld, and B. Hohlweg-Majert, "Influence of kinesiologic tape on postoperative swelling, pain and trismus after zygomatico-orbital fractures," *J Craniomaxillofac Surg*, Vol. 42, pp. 469–476, July 2014.

115. Matthews, P. B., "Evolving views on the internal operation and functional role of the muscle spindle," *J. Physiol. (Lond.)*, Vol. 320, pp. 1–30, Nov. 1981.

116. Bridgman, C. F., and E. Eldred, "Hypothesis for a pressure-sensitive mechanism in muscle spindles," *Science*, Vol. 143, pp. 481–482, Jan. 1964.

117. Han, H., and J. Kim, "Active muscle stiffness sensor based on piezoelectric resonance for muscle contraction estimation," *Sensors and Actuators A: Physical*, Vol. 194, pp. 212–219, May 2013.

118. Zhou, H., and J. E. Novotny, "Cine phase contrast mri to measure continuum lagrangian finite strain fields in contracting skeletal muscle," *J Magn Reson Imaging*, Vol. 25, pp. 175–184, Jan. 2007.

119. Englund, E. K., C. P. Elder, Q. Xu, Z. Ding, and B. M. Damon, "Combined diffusion and strain tensor mri reveals a heterogeneous, planar pattern of strain development during isometric muscle contraction," *Am. J. Physiol. Regul. Integr. Comp. Physiol.*, Vol. 300, pp. R1079–1090, May 2011.

120. Gallichan, D., J. Scholz, A. Bartsch, T. E. Behrens, M. D. Robson, and K. L. Miller, "Addressing a systematic vibration artifact in diffusion-weighted mri," *Hum Brain Mapp*, Vol. 31, pp. 193–202, Feb. 2010.

121. Descoteaux, M., R. Deriche, T. R. Knösche, and A. Anwander, "Deterministic and probabilistic tractography based on complex fibre orientation distributions," *IEEE Trans Med Imaging*, Vol. 28, pp. 269–286, Feb. 2009.

122. Bolsterlee, B., H. E. J. D. Veeger, F. C. T. van der Helm, S. C. Gandevia, and R. D. Herbert, "Comparison of measurements of medial gastrocnemius architectural parameters from ultrasound and diffusion tensor images," *J Biomech*, Vol. 48, pp. 1133–1140, Apr. 2015.

123. Chow, R. S., M. K. Medri, D. C. Martin, R. N. Leekam, A. M. Agur, and N. H. McKee, "Sonographic studies of human soleus and gastrocnemius muscle architecture: gender variability," *Eur. J. Appl. Physiol.*, Vol. 82, pp. 236–244, June 2000.

124. Blemker, S. S., and S. L. Delp, "Three-dimensional representation of complex muscle architectures and geometries," *Ann Biomed Eng*, Vol. 33, pp. 661–673, May 2005.

125. C. Criscione, J., A. S. Douglas, and W. C. Hunter, "Physically based strain invariant set for materials exhibiting transversely isotropic behavior," *Journal of the Mechanics and Physics of Solids*, Vol. 49, pp. 871–897, Apr. 2001.

126. Fedorov, A., R. Beichel, J. Kalpathy-Cramer, J. Finet, J.-C. Fillion-Robin, S. Pujol, C. Bauer, D. Jennings, F. Fennessy, M. Sonka, J. Buatti, S. Aylward, J. V. Miller, S. Pieper, and R. Kikinis, "3d slicer as an image computing platform for the quantitative imaging network," *Magn Reson Imaging*, Vol. 30, pp. 1323–1341, Nov. 2012.

127. Rana, M., G. Hamarneh, and J. M. Wakeling, "3d fascicle orientations in triceps surae," *J. Appl. Physiol.*, Vol. 115, pp. 116–125, July 2013.

128. Pamuk, U., and C. A. Yucesoy, "Mri analyses show that kinesio taping affects much more than just the targeted superficial tissues and causes heterogeneous deformations within the whole limb," *J Biomech*, Vol. 48, pp. 4262–4270, Dec. 2015.

129. Felton, S. M., T. A. Gaige, T. Benner, R. Wang, T. G. Reese, V. J. Wedeen, and R. J. Gilbert, "Associating the mesoscale fiber organization of the tongue with local strain rate during swallowing," *Journal of Biomechanics*, Vol. 41, no. 8, pp. 1782–1789, 2008.

130. Christen, D., A. Levchuk, S. Schori, P. Schneider, S. K. Boyd, and R. Müller, "Deformable image registration and 3d strain mapping for the quantitative assessment of cortical bone microdamage," *J Mech Behav Biomed Mater*, Vol. 8, pp. 184–193, Apr. 2012.

131. De Monte, G., A. Arampatzis, C. Stogiannari, and K. Karamanidis, "In vivo motion transmission in the inactive gastrocnemius medialis muscle-tendon unit during ankle and knee joint rotation," *J Electromyogr Kinesiol*, Vol. 16, pp. 413–422, Oct. 2006.

132. Julian, F. J., and D. L. Morgan, "The effect on tension of non-uniform distribution of length changes applied to frog muscle fibres," *J. Physiol. (Lond.)*, Vol. 293, pp. 379–392, Aug. 1979.

133. Allinger, T. L., M. Epstein, and W. Herzog, "Stability of muscle fibers on the descending limb of the force-length relation. a theoretical consideration," *J Biomech*, Vol. 29, pp. 627–633, May 1996.

134. Zahalak, G. I., "Can muscle fibers be stable on the descending limbs of their sarcomere length-tension relations?," *J Biomech*, Vol. 30, pp. 1179–1182, Dec. 1997.

135. Fernandez, J. W., A. Ho, S. Walt, I. A. Anderson, and P. J. Hunter, "A cerebral palsy assessment tool using anatomically based geometries and free-form deformation," *Biomech Model Mechanobiol*, Vol. 4, pp. 39–56, Aug. 2005.

136. Blemker, S. S., P. M. Pinsky, and S. L. Delp, "A 3d model of muscle reveals the causes of nonuniform strains in the biceps brachii," *J Biomech*, Vol. 38, pp. 657–665, Apr. 2005.

137. Trotter, J. A., F. J. Richmond, and P. P. Purslow, "Functional morphology and motor control of series-fibered muscles," *Exerc Sport Sci Rev*, Vol. 23, pp. 167–213, 1995.

138. Purslow, P. P., "The structure and functional significance of variations in the connective tissue within muscle," *Comp. Biochem. Physiol., Part A Mol. Integr. Physiol.*, Vol. 133, pp. 947–966, Dec. 2002.

139. Purslow, P. P., and J. A. Trotter, "The morphology and mechanical properties of endomysium in series-fibred muscles: variations with muscle length," *J. Muscle Res. Cell. Motil.*, Vol. 15, pp. 299–308, June 1994.

140. Jaspers, R. T., H. M. Feenstra, M. B. Lee-de Groot, P. A. Huijing, and W. J. van der Laarse, "Twitch and tetanic tension during culture of mature xenopus laevis single muscle fibres," *Arch. Physiol. Biochem.*, Vol. 109, pp. 410–417, Dec. 2001.

141. Yucesoy, C. A., and P. A. Huijing, "Specifically tailored use of the finite element method to study muscular mechanics within the context of fascial integrity: The linked fiber-matrix mesh model," *International Journal for Multiscale Computational Engineering*, Vol. 10, no. 2, pp. 155–170, 2012.

142. Yucesoy, C. A., A. N. Turkoğlu, S. Umur, and F. AteÅ, "Intact muscle compartment exposed to botulinum toxin type a shows compromised intermuscular mechanical interaction: Btx-a compromises mechanics," *Muscle & Nerve*, Vol. 51, pp. 106–116, Jan. 2015.

143. Maas, H., G. C. Baan, P. A. Huijing, C. A. Yucesoy, B. H. Koopman, and H. J. Grootenboer, "The relative position of edl muscle affects the length of sarcomeres within muscle fibers: experimental results and finite-element modeling," *J Biomech Eng*, Vol. 125, pp. 745–753, Oct. 2003.

144. Tian, M., R. D. Herbert, P. Hoang, S. C. Gandevia, and L. E. Bilston, "Myofascial force transmission between the human soleus and gastrocnemius muscles during passive knee motion," *J. Appl. Physiol.*, Vol. 113, pp. 517–523, Aug. 2012.

145. Maas, H., and T. G. Sandercock, "Are skeletal muscles independent actuators? force transmission from soleus muscle in the cat," *J. Appl. Physiol.*, Vol. 104, pp. 1557–1567, June 2008.

146. Shin, D. D., J. A. Hodgson, V. R. Edgerton, and S. Sinha, "In vivo intramuscular fascicle-aponeuroses dynamics of the human medial gastrocnemius during plantarflexion and dorsiflexion of the foot," *J. Appl. Physiol.*, Vol. 107, pp. 1276–1284, Oct. 2009.

147. Muraoka, T., T. Muramatsu, H. Kanehisa, and T. Fukunaga, "Transverse strain of aponeurosis in human tibialis anterior muscle at rest and during contraction at different joint angles," *Journal of Applied Biomechanics*, Vol. 19, pp. 39–48, Feb. 2003.

148. Wu, D., J. Xu, M. T. McMahon, P. C. M. van Zijl, S. Mori, F. J. Northington, and J. Zhang, "In vivo high-resolution diffusion tensor imaging of the mouse brain," *Neuroimage*, Vol. 83, pp. 18–26, Dec. 2013.

149. Morgan, D. L., N. P. Whitehead, A. K. Wise, J. E. Gregory, and U. Proske, "Tension changes in the cat soleus muscle following slow stretch or shortening of the contracting muscle," *J. Physiol. (Lond.)*, Vol. 522 Pt 3, pp. 503–513, Feb. 2000.

150. Wohlfart, B., A. F. Grimm, and K. A. P. Edman, "Relationship between sarcomere length and active force in rabbit papillary muscle," *Acta Physiologica Scandinavica*, Vol. 101, pp. 155–164, Oct. 1977.

151. Willems, M. E., and P. A. Huijing, "Heterogeneity of mean sarcomere length in different fibres: effects on length range of active force production in rat muscle," *Eur J Appl Physiol Occup Physiol*, Vol. 68, no. 6, pp. 489–496, 1994.

152. Matthiasdottir, S., M. Hahn, M. Yaraskavitch, and W. Herzog, "Muscle and fascicle excursion in children with cerebral palsy," *Clin Biomech (Bristol, Avon)*, Vol. 29, pp. 458–462, Apr. 2014.

153. Pamuk, U., A. Karakuzu, C. Ozturk, B. Acar, and C. A. Yucesoy, "Combined magnetic resonance and diffusion tensor imaging analyses provide a powerful tool for in vivo assessment of deformation along human muscle fibers," *J Mech Behav Biomed Mater*, Vol. 63, pp. 207–219, 2016.

154. Maas, H., "Significance of epimuscular myofascial force transmission under passive muscle conditions," *J. Appl. Physiol.*, Jan. 2019.

155. Herbert, R. D., B. Bolsterlee, and S. C. Gandevia, "Passive changes in muscle length," *J. Appl. Physiol.*, Dec. 2018.

156. Wakahara, T., H. Kanehisa, Y. Kawakami, and T. Fukunaga, "Fascicle behavior of medial gastrocnemius muscle in extended and flexed knee positions," *Journal of Biomechanics*, Vol. 40, pp. 2291–2298, Jan. 2007.

157. Arampatzis, A., K. Karamanidis, S. Stafilidis, G. Morey-Klapsing, G. DeMonte, and G.-P. Brüggemann, "Effect of different ankle- and knee-joint positions on gastrocnemius medialis fascicle length and emg activity during isometric plantar flexion," *Journal of Biomechanics*, Vol. 39, pp. 1891–1902, Jan. 2006.

158. Trombitás, K., J. P. Jin, and H. Granzier, "The mechanically active domain of titin in cardiac muscle," *Circ. Res.*, Vol. 77, pp. 856–861, Oct. 1995.

159. Huyghe, J. M., D. H. van Campen, T. Arts, and R. M. Heethaar, "A two-phase finite element model of the diastolic left ventricle," *J Biomech*, Vol. 24, no. 7, pp. 527–538, 1991.

160. Karakuzu, A., U. Pamuk, C. Ozturk, B. Acar, and C. A. Yucesoy, "Magnetic resonance and diffusion tensor imaging analyses indicate heterogeneous strains along human medial gastrocnemius fascicles caused by submaximal plantar-flexion activity," *Journal of Biomechanics*, Vol. 57, pp. 69–78, May 2017.

161. Andrade, R. J., A. Nordez, F. Hug, F. Ates, M. W. Coppieters, P. Pezarat-Correia, and S. R. Freitas, "Non-invasive assessment of sciatic nerve stiffness during human ankle motion using ultrasound shear wave elastography," *J Biomech*, Vol. 49, pp. 326–331, Feb. 2016.

162. Gordon, A. M., A. F. Huxley, and F. J. Julian, "The variation in isometric tension with sarcomere length in vertebrate muscle fibres," *J. Physiol. (Lond.)*, Vol. 184, pp. 170–192, May 1966.

163. Linke, W. A., "Stretching molecular springs: elasticity of titin filaments in vertebrate striated muscle," *Histol. Histopathol.*, Vol. 15, no. 3, pp. 799–811, 2000.

164. Wang, K., and R. Ramirez-Mitchell, "A network of transverse and longitudinal intermediate filaments is associated with sarcomeres of adult vertebrate skeletal muscle," *J. Cell Biol.*, Vol. 96, pp. 562–570, Feb. 1983.

165. Nishikawa, K. C., J. A. Monroy, and U. Tahir, "Muscle function from organisms to molecules," *Integr. Comp. Biol.*, Vol. 58, no. 2, pp. 194–206, 2018.

166. Leonard, T. R., and W. Herzog, "Regulation of muscle force in the absence of actin-myosin-based cross-bridge interaction," *Am. J. Physiol., Cell Physiol.*, Vol. 299, pp. C14–20, July 2010.

167. Eckels, E. C., R. Tapia-Rojo, J. A. Rivas-Pardo, and J. M. Fernández, "The work of titin protein folding as a major driver in muscle contraction," *Annual Review of Physiology*, Vol. 80, pp. 327–351, Feb. 2018.

168. Abbott, B. C., and X. M. Aubert, "Changes of energy in a muscle during very slow stretches," *Proc. R. Soc. Lond., B, Biol. Sci.*, Vol. 139, pp. 104–117, Dec. 1951.

169. Bigland, B., and O. C. Lippold, "The relation between force, velocity and integrated electrical activity in human muscles," *J. Physiol. (Lond.)*, Vol. 123, pp. 214–224, Jan. 1954.

170. Edman, K. A., G. Elzinga, and M. I. Noble, "Enhancement of mechanical performance by stretch during tetanic contractions of vertebrate skeletal muscle fibres," *J. Physiol. (Lond.)*, Vol. 281, pp. 139–155, Aug. 1978.

171. Herzog, W., E. J. Lee, and D. E. Rassier, "Residual force enhancement in skeletal muscle," *J. Physiol. (Lond.)*, Vol. 574, pp. 635–642, Aug. 2006.

172. Herzog, W., "The role of titin in eccentric muscle contraction," *Journal of Experimental Biology*, Vol. 217, pp. 2825–2833, Aug. 2014.

173. Lee, E.-J., and W. Herzog, "Residual force enhancement exceeds the isometric force at optimal sarcomere length for optimized stretch conditions," *J. Appl. Physiol.*, Vol. 105, pp. 457–462, Aug. 2008.

174. Zuurbier, C. J., A. J. Everard, P. van der Wees, and P. A. Huijing, "Length-force characteristics of the aponeurosis in the passive and active muscle condition and in the isolated condition," *J Biomech*, Vol. 27, pp. 445–453, Apr. 1994.

175. Ger, R. B., J. Yang, Y. Ding, M. C. Jacobsen, C. E. Cardenas, C. D. Fuller, R. M. Howell, H. Li, R. J. Stafford, S. Zhou, and L. E. Court, "Synthetic head and neck and phantom images for determining deformable image registration accuracy in magnetic resonance imaging," *Medical Physics*, Vol. 45, pp. 4315–4321, Sept. 2018.

176. Clark, K., B. Vendt, K. Smith, J. Freymann, J. Kirby, P. Koppel, S. Moore, S. Phillips, D. Maffitt, M. Pringle, L. Tarbox, and F. Prior, "The cancer imaging archive (tcia): Maintaining and operating a public information repository," *Journal of Digital Imaging*, Vol. 26, pp. 1045–1057, Dec. 2013.

177. Ger, R., J. Yang, Y. Ding, M. Jacobsen, C. Cardenas, C. Fuller, R. Howell, H. Li, R. J. Stafford, S. Zhou, and L. Court, "Data from synthetic and phantom mr images for determining deformable image registration accuracy (mri-dir)," 2018.

178. Yoshitake, Y., D. Uchida, K. Hirata, D. L. Mayfield, and H. Kanehisa, "Mechanical interaction between neighboring muscles in human upper limb: Evidence for epimuscular myofascial force transmission in humans," *J Biomech*, Vol. 74, pp. 150–155, June 2018.